Phase Space Analysis of Quantum Effects in Strong Field Ionisation

Héloise Chomet

University College London

Physics and Astronomy

Submitted to University College London (UCL) in partial fulfilment of the requirements for the award of the degree of Doctor of Philosophy.

Primary supervisor: Prof. Carla Figueira de Morisson Faria

Secondary supervisor: Prof. Marzena Szymanska

Thesis submission date: January 18, 2023

Declaration

I, Héloise Chomet, confirm that the work presented in this thesis is my own. Where information has been derived from other sources, I confirm that this has been indicated in the thesis. The following parts of this thesis have been published in journals:

1. **Chapters 1**, **2**, **3**, **5**:

   H Chomet, D Sarkar and C Figueira de Morisson Faria "Quantum bridges in phase space: interference and nonclassicality in strong-field enhanced ionisation" New J. Phys. 21 123004 (2019)

2. **Chapters 2**, **5**:

   D Kufel, H Chomet and C Figueira de Morisson Faria "Alternative quantisation condition for wavepacket dynamics in a hyperbolic double well" J. Phys. A: Math. Theor. 54 035304 (2021)

3. **Chapters 1**, **2**, **5**:

   H Chomet and C Figueira de Morisson Faria "Attoscience in phase space" Eur. Phys. J. D 75, 201 (2021)

4. **Chapters 2**, **6**:

   H Chomet, S Plesnik, C D Nicolae, J Dunham, L Gover, T Weaving, C Figueira de Morisson Faria "Controlling quantum effects in enhanced strong-field ionisation with machine-learning techniques" J. Phys. B: At. Mol. Opt. Phys. 55 245501 (2022)

Abstract

This thesis explores quantum effects during strong field ionisation, with emphasis on both classical and quantum phase-space interpretational tools. Specifically, this involves investigating the presence of momentum gates during the enhanced ionisation of H_2^+. These structures cycle through the momentum space without following the time-profile of the external field. By computing autocorrelation functions and Wigner quasiprobability distributions, we establish that momentum gates may occur for static driving fields, and even for no external field at all. Their primary cause is an interference-induced bridging mechanism that occurs if both wells in the molecule are populated. Their cyclic motion in momentum space has a non-classical evolution, as seen from the quantum Liouville equation. Additionally, we employ the quantum trajectory method to seek another criteria for non-classicality.

Using an analytical method, we then compute the different eigenfrequencies governing the system in a field-free setting. This provides an in-depth understanding that is applied to the time-dependent case. There, the frequency of the quantum bridge, intrinsic to the molecule, is higher than that of the external field. This leads the quasiprobability distribution to sometimes counter-intuitively flow in the direction opposed to the electric-field gradient.

These ionisation mechanisms form an optimisation problem that can be controlled using the appropriate molecular targets, driving fields and coherent superposition of states. We investigate the impact of multiple parameters at once by employing machine learning dimensionality reduction techniques. This allows us to disentangle the different effects at play and establish a hierarchy of parameters for controlling ionisation. The features encountered are explained with phase-space arguments and optimal conditions are found for both static and time-dependent fields. The conclusions presented throughout this thesis can in the future be expanded towards multielectron systems, incorporating decoherence and multiple degrees of freedom.

Impact Statement

The work presented in this thesis focuses on the understanding and control of electrons in strong-fields in the timescale of attosecond (10^{-18} sec), which is one of the shortest timescales accessible in nature.

Our methods will affect the strong field community by bringing into focus powerful tools that are underused in the field. Phase space tools and quasiprobability distributions are instrumental to the physical interpretation of our results and are used to investigate non-classicality in strong field ionisation by, for instance, determining how bifurcations and different phase-space regions impact electron dynamics. They also enjoy great success in many fields such as quantum information, quantum optics and cold gases. This thesis brings this toolkit to the forefront of strong field and attosecond science.

In addition, this thesis can inspire applications of machine learning in the study of complex dynamical systems wherever they may arise. Machine learning methods, which help develop insight into the behaviour of complex systems, have been successfully utilised in a variety of research areas in physics, such as particle physics, astrophysics, condensed matter physics or quantum optics. More generally machine learning and artificial intelligence benefits in an immense variety of fields, such as image recognition, finance, agriculture, robotics or medical diagnosis. Despite their success, they are rarely present in strong-field and attosecond science, where they could provide great value. For instance, this thesis specifically analyses enhanced ionisation. This system depends critically on a wide range of parameters and their joint influence is very difficult to study systematically. The vast majority of work in this field focuses on a qualitative assessment of one parameter at a time. Yet, it is an ideal problem for machine learning dimensionality-reduction techniques as they are tailor-made to extract information from complex data sets.

Many of the conclusions found throughout this thesis can have powerful future applications in other scientific domains and for greater commercial use. Molecular electron localisation, which was highlighted as critical by the techniques used, is a key aspect of experimental and theoretical chemical reaction control. Thus, this thesis contributes to studies on precise timing and manipulation of chemical reactions and systems. Controlling electron release and coherent superpositions of states are important aspects in many scientific areas such as quantum technologies

and chemical reaction control. Finally, we focus on the steering of electron dynamics in the attosecond domain, which would allow unprecedented access to molecular ultrafast imaging. This potency could benefit a wide variety of industries outside of theoretical physics, for example medical imaging. In addition, new devices, for instance ultrafast electronics, could be pioneered by the control over the attosecond timescale enabled through those strong field processes.

Acknowledgements

First, I would like to express my deepest gratitude to my supervisor Prof Figueira de Morisson Faria for her guidance, without which this thesis would have not been possible.
I would also like to thank my fellow co-workers at UCL Dr Andrew Maxwell, Dr Abbie Bray, Dr Cornelia Hofmann, Gyeonghun Kim, Dr Lidice Cruz-Rodriguez and Tom Rook for their insights and friendship. I would also like to thank my co-authors Dhruva Sarkar, Dominik Kufel, Dragos Constantin Nicolae, Jack Dunham, Lesley Gover, Tim Weaving and Samuel Plesnik for their useful contributions.
Finally, I would like to offer my biggest thanks to my family for their love, support and encouragement throughout this entire journey.

Contents

Table of Acronyms

Notation	Description
TWA	Truncated Wigner Approximation.
ATI	Above-Threshold Ionisation.
FEL	Free-Electron Lasers.
XUV	eXtreme UltraViolet.
IVR	Initial Value Representation.
CCS	Coupled Coherent State.
CQSFA	Coulomb Quantum orbit Strong-Field Approximation.
SCTS	SemiClassical Two-Step.
HHG	High Harmonic Generation.
NSDI	Non-Sequential Double Ionisation.
RESI	Recollision Excitation with Subsequent Ionisation.
TDSE	Time-Dependent Schrödinger Equation.
TISE	Time-Independent Schrödinger Equation.
QTM	Quantum Trajectory Method.
PCA	Principal Component Analysis.
t-SNE	t-distributed Stochastic Neighbour Embedding.

List of Figures

List of Tables

Chapter 1

Introduction

1.1 Phase space historical overview

The idea of phase space, in which one may depict all possible states of a dynamical system evolving from *any* initial conditions by trajectories, is extremely powerful. Each phase space trajectory represents the evolution of a system starting from specific initial conditions, with each point corresponding to the state of the system at a specific time. The set of all phase space trajectories thus provides a mapping of all possible ways in which a system may evolve. In particular, the phase space is used for dealing with multidimensional systems, whose description would be much less intuitive otherwise. Examples of such systems are encountered in a wide range of areas, including physics, biology, chemistry and financial models (see [1] for a recent review). In physics alone, phase space tools are typically used in, for instance, statistical physics, quantum optics, collision theory, particle physics and nonlinear dynamics, and widely employed phase space variables are, for instance, positions and momenta, or angles and angular momenta. Its mathematical origin, dating from 1838, can be attributed to Liouville [2], and its first application to mechanics was made by Jacobi in 1842 [3]. However, the concept of describing the dynamics of a system as a single trajectory moving through multidimensional space was developed many decades later by Poincaré [4] (for a historic review on the subject see [5]).

The quantum phase space was introduced much later, by Wigner, together with the quasiprobability distribution named after him [6]. Since then, quantum phase space distribution functions, constructed using non-commuting operators, have become widespread. A key advantage is that they allow one to employ complex-number functions instead of dealing with operators. Furthermore, they provide valuable insight in quantum-classical correspondence [7], within the constraints posed by the uncertainty principle and its generalisations. However, there are different phase space distribution functions, whose applicability may suit specific problems better than others. This ambiguity stems from the fact that there are different rules

for associating non-commuting operators to scalar variables [8, 9]; for pioneering work exploring operator ordering in connection with quasiprobability distributions see also [10, 11]. For instance, due to their smooth behavior, Husimi distribution functions are popular in the context of nonlinear systems and classical chaos [12], while Wigner quasiprobability distributions, due to the information they provide on non-classical effects and quantum corrections, are widely used in quantum optics [13, 14]. Other applications of the Wigner function include optical propagation in waveguides [15], and the computation of angular momentum states [16], which can also be used to model two-level atoms [17, 18, 19]. The Glauber-Shudarshan $\mathcal{P}$ functions [20, 21] are also hugely popular in quantum optics, as they are very convenient for normal-ordered products of creation and annihilation operators.

Quantum phase space distribution functions play a major role in quantum optics [13, 14] and quantum information [22, 23]. This popularity has been triggered by the description of the electromagnetic field modes as quantum harmonic oscillators, for which distribution functions have been especially tailored (see, e.g., the discussion in [8, 9, 20, 21]), and the central interest in the definition of non-classical states of light [24]. Furthermore, due to being formulated in terms of density matrices, quasiprobability densities are well suited for investigating decoherence and the influence of the environment [25, 26, 19]. Quasiprobability distributions have also been explored in connection with logical gates [27, 28] and their classical simulation [29], and coherent-state superposition [30, 31].

Other traditional areas in which the quantum phase space is widely used are those dealing with large systems [32], such as chemical physics [33, 34], photochemistry [35], and cold gases [36]. In this case, the huge number of degrees of freedom makes a full quantum-mechanical treatment prohibitive. Therefore, crucial questions are what degrees of freedom need full treatment and which ones can be approximated, what kind of fluctuations and deviations from the classical picture are expected, and whether there are semiclassical limits one can take into consideration without losing essential information about the system's dynamics.

In the study of complex molecular systems, for instance, it is common to apply mixed classical-quantum methods, which describe less relevant degrees of freedom classically, more relevant degrees of freedom quantum mechanically, and couple them via effective potentials [37, 38]. One may also consider systems coupled to baths, whose dynamics are simplified [39]. Alternatively, one may develop semiclassical methods, in which swarms of classical trajectories are employed to construct quantum propagators (see, e.g., [40, 41, 42, 43, 44] and the reviews [33, 45]). Further approximations may then be applied, such as the smoothing of highly oscillatory terms [7], and linearised semiclassical approximations, in which the main contributions stem from trajectories whose phase space coordinates are close enough [41]. Truncated Wigner approximations are also widely used to describe chemical reac-

tions (for an early example see [41]).

Furthermore, there are many perturbative approximations which incorporate quantum fluctuations around classical limits, such as the semiclassical or truncated Wigner approximation (TWA). For an early discussion of phase space methods in which stochastic evolution equations, including the TWA, are applied to Bose-Einstein Condensates see [46]. The key idea is to embed quantum fluctuations in the initial quasiprobability distributions, which are then evolved classically. This means that quantum corrections appear only through initial conditions. Classical evolution is desirable for large systems as, typically, classical equations of motion scale linearly with its degrees of freedom, while quantum methods scale exponentially. The TWA has been explored in the context of Bose condensed gases perturbed from thermal equilibrium [47] in a wide range of scenarios such as the evolution of macroscopic entangled states [48], quantum fluctuations in condensate oscillations [49], non-classical effects arising from the splitting of condensates [50, 51] and vortices in reflecting Bose-Einstein condensates [52]. It works for weakly perturbed systems.

In contrast, in strong-field laser-matter interaction and attosecond science, the phase space picture and its tools have not become mainstream. This is actually surprising for the following reasons:

- *Classical and semi-classical trajectory-based methods have been used as interpretational tools for quantum effects since over two decades, and helped establish the key paradigms in the field.* Therein, laser-induced rescattering and recombination of an electron with its parent ion play a vital role by providing an intuitive interpretation of many strong-field phenomena (see, e.g., [53, 54, 55] and the special issue [56]). If recombination with a bound state occurs, the kinetic energy acquired by the electron in the continuum is released in form of high-order harmonic radiation, while rescattering will lead to high-energy photoelectrons. If the returning electron rescatters elastically, high-order above-threshold ionisation (ATI) will occur [57, 58]. Alternatively, if, upon recollision, it passes on part of its kinetic energy to the core, it may release other electrons, leading to nonsequential double and multiple ionisation [59, 60]. This orbit-based picture has been hugely successful in describing the physics of the problem, with far reaching consequences. For instance, the shapes of the high-harmonic and high-order ATI spectra, with a long plateau followed by sharp cutoffs whose energy positions are a multiple of the ponderomotive energy U_p [54, 58], proportional to the driving-field intensity, can be explained using the laser-induced rescattering picture. Furthermore, because ionisation and recombination occur at very specific times within a field cycle, they can be used for steering subfemtosecond electron dynamics, for generating attosecond pulses or bursts of electrons (see, e.g. [61, 62], and the special issue [63]), and for subfemtosecond imaging of matter [64, 65, 66]. For

a given energy, there is usually more than one quantum mechanical pathway along which the electron may interact with the core, so the corresponding transition amplitudes interfere. Quantum interference has many attosecond imaging applications, using high-order harmonic generation or photoelectrons (for reviews see, e.g., [67] or [68]).

- *The interaction between the continuum and bound states is of vital importance*, as strong-field ionisation and laser-induced rescattering or recombination play a key role in explaining strong-field phenomena [54, 55, 57, 59, 58, 68, 69]. Yet, tools that could provide rigorous and/or accurate information about non-classicality or boundaries of bound-continuum dynamics are underused.

Still, some groups have explored phase space dynamics in a strong-field context. This includes stabilisation [70, 71, 72, 73], strong-field ionisation [74, 75, 76, 77, 78], high-order harmonic generation [79, 80, 81, 82, 83], laser-induced core dynamics [84, 85], rescattering [86, 87, 79, 88, 80, 89], nonsequential double ionisation [90, 99, 100, 101, 102, 103, 104, 105, 106, 91, 92, 93, 94, 95, 96, 97, 98], or in connection with initial-value representations in strong fields [107, 108, 109, 110, 77]. Furthermore, the growing interest in free-electron lasers (FELs) means that the tools employed in quantum optics are being explored in the X-ray and extreme ultraviolet (XUV) regime [111, 112]. Examples range from seminal work unifying quantum and classical descriptions of electron dynamics in FELs [113, 114] to providing a road map for quantum signatures therein [115]. They include the development of quantum models whose radiation holds the promise of having better quality than that of classical FELs [116, 117, 118, 119, 115].

Overall, the use of phase space has been twofold: either the *classical* phase space was employed to delimit bound-continuum boundaries, highlight regular or chaotic behavior, and analyse different rescattering regimes, or *quantum* phase space distributions have been employed to assess classical or non-classical behavior and provide initial conditions for other methods. Often the intuitive picture obtained by classical methods is compared with the outcome of *ab-initio* computations or other approaches.

1.2 Phase space use in attoscience

Historically, the phase space has been applied to a variety of phenomena in attoscience, along the following research lines: Free-electron lasers and stabilisation, tunneling, rescattering in one-electron systems and correlated multielectron dynamics. These research lines often overlap, and a key common aspect is to try to understand and control attosecond electron dynamics in greater depth. They are briefly discussed below.

1.2.1 Free-electron lasers and stabilisation

Phase space tools have been first used in attosecond science and related fields in the 1980s, in the context of free-electron lasers (FELs) [113, 114]. These seminal papers aimed at bridging a gap that existed between fully quantum electrodynamic descriptions of electrons in a FEL and widespread classical descriptions of these dynamics. This was an important milestone as the classical description of electrons in a FEL are expected to become inaccurate in the XUV/X ray regime, for which quantum fluctuations are important [113, 114]. For that purpose, Wigner quasiprobability distributions were used and it was shown that, in the classical limit, the former descriptions were recovered. Following that, there have been phase space studies to determine the boundary between classical and quantum behaviour [116, 117, 118, 119, 115]. These studies have been motivated by the prospects of developing a Quantum FEL, which should exhibit a narrower linewidth and better temporal coherence than its classical counterpart [120]. In particular, one- [117] and three-dimensional [118] quantum models based on Wigner functions were presented. In [119], the phase space was used to establish a quantum regime, in which the system may be approximated by a two-level atom by averaging over fast oscillations. Recently, quantum effects in the FEL electrons and its gain were studied using Wigner quasiprobability distributions and the quantum Liouville equation [115].

Further work in the high-frequency regime, in the 1990s, addressed the question of non-classical behavior in atomic stabilisation. Atomic stabilisation stems from the breakdown of Fermi's golden rule for computing ionisation probabilities in strong laser fields. Roughly speaking, stabilisation is the suppression of ionisation with increasing field strength. In the 1990s, it has generated a great deal of controversy, from its definition, to the physical mechanisms behind it and its existence altogether (for reviews see [121, 122, 123, 124]). In this context, the Kramers-Henneberger frame, in which the field time dependence is embedded in the binding potential, is widely used. For high driving-laser frequencies, one may define a double-well effective potential, known as the Kramers-Henneberger potential. Wigner quasiprobability distributions were employed to assess under what conditions stabilisation was classical or quantum [70]. They were compared to classical-trajectory computations and exhibited regions that were attributed to coherent superpositions of a few bound states of the effective Kramers-Henneberger potential, thus highlighting the role of quantum interference [71]. Further work explored how quantum effects in stabilisation depend on the pulse shape and on the effective Kramers-Henneberger potential by using Wigner and Husimi distributions [72]. Much later work relates stabilisation to trapped trajectories and elliptic islands in a chaotic region via a classical phase space analysis, and highlights a hidden short-time nature of stabilisation [73].

1.2.2 Tunneling

In the low-frequency regime, phase space quantum distribution functions have been employed to assess tunneling ionisation dynamics since the early 2000s. Tunneling is crucial for strong-field and attosecond physics, and the question of with what velocity, and at what point in space an electron reaches the continuum, as well as whether one may define finite tunneling times, has attracted a great deal of attention (see, e.g., [125, 127, 128, 129, 130, 131, 132, 133, 134, 126] for a wide range of approaches and points of view). Since the phase space allows for an intuitive view of the classical-quantum correspondence, it is ideally suited to such questions.

Early studies of tunneling ionisation in phase space observed a tail for the Wigner quasiprobability distribution of a system in a static or quasi-static, low-frequency field. This tail has been associated with tunnel ionisation as it crosses from a bound phase space region to the continuum through classically forbidden regions [135]. Its slope has been employed to define a tunnel trajectory, which was first computed by [74] using an analytical model of a zero-range potential in a static field. Further work, a decade later, [79] investigated how the slope of the Wigner function behaved with regard to the potential being short or long range. Both publications focused on the agreement between the tail of phase space quantum distributions and a classical-trajectory picture, which were shown to match far away from the core. Nonetheless, quantum interference fringes associated with tunneling events at different times were observed in both publications. Close to the core, the tail of the Wigner function follows the separatrix and crosses into the continuum either via over the barrier or tunnel ionisation [77]. Recently, Wigner quasiprobability distributions have been employed to reconstruct the tunnel exit, which is an important parameter in determining the tunneling time [136]. Further work by the same group addresses the influence of quantum interference and over-the-barrier ionisation on classical-quantum correspondence when an electron is freed into the continuum [137]. For systems with more than one centre, such as in diatomic molecules, Wigner quasiprobability distributions have been employed in the context of enhanced ionisation [75, 76]. More details on the subject is presented is section 1.3.

Tunneling dynamics in strong fields has also been looked at in the context of initial-value representations (IVRs) [138, 77]. In initial-value representations, the boundary problems that arise in semiclassical theory are replaced by averages over initial phase space coordinates, which are used to construct wave packets. These wave packets are then evolved in time, guided by ensembles of classical trajectories. IVRs are employed in many areas of science, for instance quantum chemistry, chaos and nonlinear dynamical systems, and are very powerful approaches due to their scalability and absence of cusps and singularities. For key references see, e.g., [40, 41, 42, 43, 44] and the reviews [33, 45]. However, there has been considerable debate whether these approaches can be used to model tunnel ionisation, as they employ

ensembles of real classical trajectories to construct wave packets [139, 140, 141, 142]. Tunneling may manifest itself in position space, as transmission, or in momentum space, as above-the-barrier reflection, and it not being accounted correctly will cause semiclassical IVRs to degrade for longer times [142]. Nonetheless, because the top of a potential barrier can be approximated by an inverted harmonic oscillator, tunneling has been found to work well near this threshold [135]. To deal with this, one may either focus on rescattering only and place the initial electronic wave packet away from the core [107, 108], or employ short times and IVRs with effective potentials that account for quantum corrections, such as the Coupled Coherent State (CCS) method [77]. Phase space has also been employed to develop path integral approaches [143] that incorporate the residual potentials and the driving field on equal footing, such as the Coulomb Quantum Orbit Strong-Field Approximation (CQSFA) [144, 145, 146, 147] and the semiclassical two-step (SCTS) model [148, 149, 150], with emphasis on quantum interference and photoelectron holography. For a review see [68].

1.2.3 Rescattering in one-electron systems

Because most strong-field phenomena can be explained as laser-induced rescattering, one must understand how it manifests itself in phase space. Although structures associated with rescattering have already been identified in [74], closer scrutiny happened only in the 2010s. In [151], distinct interference patterns in Wigner quasiprobability distributions have been associated with different types of intra-cycle electron scattering and above-threshold ionisation. This has been extended in [87] in order to assess lower impact velocities, and to compute the bound-state population using phase space criteria. Therein, phase space signatures of channel closings have also been identified. Further work has investigated the connection between rescattering and entanglement [88].

Rescattering in phase space has also been studied in relation to other phenomena. For instance, in [79], a phase space analysis of rescattering in conjunction with high-order harmonic generation (HHG) was performed employing Wigner and Husimi distribution functions. It was shown that the rescattering wave packet exhibits a chirp, which can be extracted from the Wigner quasiprobability distribution at the position of rescattering. The HHG temporal profile given by the Wigner function strongly resembles that obtained by other means such as windowed Fourier transforms. Recent work has focused on a systematic analysis of the orbit-based rescattering picture for tunneling, rescattering and HHG using Wigner functions with spatial windows in reduced-dimensionality models, and effective Wigner functions for multidimensional systems in order to facilitate the interpretation of more intricate dynamics [89].

Different types of orbits and their role in HHG [107] and ATI [108] have also been

investigated using initial-value representations. It was found that irregular orbits play an important role in forming the HHG plateau. Furthermore, phase space tools have been employed to identify regions of dominant, integrable Hamiltonians, which led to HHG spectra with excellent agreement with ab-initio methods [109, 110]. A key challenge in modeling HHG is that it is a coherent process that relies on the periodicity of the field. This implies that any dephasing associated with the degradation of the time evolution determined by the IVR will affect the harmonic spectra. This will play a key role if the wave packet is initially bound as tunnel ionisation will be important in this case (for discussions see [77, 152]).

Subsequently, a purely classical perspective into how the presence of the Coulomb potential affects recollisions in strong fields, as related to the high-harmonic spectra, is provided in a series of publications [80, 81, 83]. Therein, classical phase space arguments have been used to show that Coulomb focusing enhances delayed recollisions and increase their energy. These recollisions occur along periodic orbits whose energy are higher than the standard cutoff energy value of $3.17U_p$ [81], where U_p is the ponderomotive energy. Nonetheless, in [80], a fully classical method that considers the Coulomb potential in the continuum is employed to explain why the standard cutoff law works. A set of periodic orbits stemming from a resonance with the field are linked to laser-induced recollision, whose maximal energy approaches the standard HHG cutoff in the high-intensity limit. Good agreement with the *ab-initio* solution of the time-dependent Schrödinger equation is observed. Further work explores the extension of the cutoff upon macroscopic propagation [83]. The phase space has also been employed by us in [82] to extract different instantaneous configurations and time scales for HHG in inhomogeneous fields.

1.2.4 Correlated multielectron processes

In addition to one-electron problems, since the early 2000s, the phase space has been used to explore non-trivial features in correlated multielectron processes. This extends from laser-induced nonsequential double ionisation (NSDI) [59], which is the archetypical example of electron-electron correlation in intense laser fields [90], to the temporal profile of autoionisation dynamics in Helium [85]. For instance, in [90] Wigner quasi-probability distributions associated with the centre-of mass coordinates of a two-particle system have been compared to the outcome of a mean-field theory in order to identify signatures of rescattering and electron-electron interaction. NSDI has also been modeled for the Helium atom using IVRs beyond reduced-dimensionality models [153, 154]. In particular an alternative version of the Coupled Coherent States (CCS) method that incorporates the exchange symmetry of fermionic particles, the fermionic CCS, has been successfully applied in this context [154].

A whole line of research has been devoted to investigating NSDI in a fully clas-

sical framework. In NSDI, an outer electron reaches the continuum, is brought back by the field and transfers part of its kinetic energy to an inner electron. These recollision dynamics are quite rich and can be interpreted using tools from phase space, the theory of non-linear dynamical systems, and effective Hamiltonians for each of the electrons involved. These reduced, integrable Hamiltonians were first defined in [105, 106] for NDSI. Subsequently, the role of multiple recollisions on the efficient energy transfer in NSDI has been investigated using symplectic maps and similar approaches to those used in kicked Rydberg atoms, and a road map has been provided for identifying different NSDI mechanisms in [91, 92]. Further work by the same group has focused on an in-depth analysis of recollision excitation with subsequent ionisation (RESI) in terms of resonances and their proximity to periodic orbits [95, 96]. In particular, a sticky region in phase space arises due to the interplay of the external field and the binding potential. This region traps trajectories before ionisation, leading to time delays for the second electron. A detailed analysis of the types of periodic orbits, resonance conditions and distinct sources of chaos is provided in [96]. Interestingly, if reduced-dimensionality models are used, oscillations in the RESI yield as functions of the laser intensity are reported and attributed to resonances. However, these oscillations are washed out if more degrees of freedom are incorporated, due to chaotic transverse dynamics and additional resonances. These oscillations are distinct from those attributed to quantum interference in RESI [155, 156, 157, 158]. Further work is related to NSDI in bichromatic, linearly polarised fields [94], and the dynamics of recollisions in fields with circular polarisation [93, 97, 98]. In [93] it is shown that, in contrast to previous assumptions, recollisions may occur in circularly polarised fields, by analysing the system's dynamics in a rotating frame. The physical mechanism is similar to that leading to ionisation in Rydberg atoms in microwave fields. A decade later, this topic is revisited and several associated time scales are analysed in detail [97, 98]. In particular, a recollision mechanism taking place over many field cycles is reported.

One may also employ classical models and dynamical systems tools to determine modified threshold laws for correlated multielectron ionisation that account for the presence of an external field [99]. This approach starts by identifying similarities with its field-free counterpart [159], considering the two or more electrons in an excited compound and identifying the relevant subspaces for which correlated double and multiple ionisation may occur. This information can then be used to construct effective reduced Hamiltonians for the subspace of interest, identify existing symmetries and possible electron escape configurations, and determine which of the latter will prevail. This has been done for nonsequential double [100, 103], triple [101] and multiple [102] ionisation. One can also use this method as guidance for defining effective reduced-dimensionality quantum models, so that the actual dynamics are preserved as faithfully as possible, without introducing artificial constraints or

correlations [104].

Another manifestation of electron-electron correlation is autoionisation. Thereby, the quantum interference between a direct and a quasi-resonant pathway is of extreme importance. Wigner quasi-probability distributions in the time-energy domain are used to study this interference and disentangle these pathways in a transient process [85]. They provide an advantage over other methods used in time-frequency analysis, for exposing non-classical behavior in a much more explicit way. A further issue is that, in classical-trajectory models, autoionisation manifests itself as an artifact that renders the system unstable. These problems have been overcome in [86, 160], which employ quasiprobability densities and phase space arguments to develop classical-trajectory models that do not exhibit these shortcomings and are consistent with their quantum-mechanical counterparts. Wigner quasi-probability distributions in the time-energy domain are also used to analyse interfering resonances [161] during the photoionisation of Xenon.

1.3 Enhanced ionisation

A peculiar and well-known effect that occurs for stretched molecules in strong, low-frequency fields is enhanced ionisation. It consists of a sharp increase in the ionisation rate around specific inter-nuclear separations, typically a few times larger than the equilibrium distance. Since its first prediction [162], enhanced ionisation has been calculated and measured in myriad systems. These include diatomic [163, 164] molecular species such as H_2 [165, 166, 167, 168, 76, 75], I_2 [169, 170, 171, 172], and Cl_2 [173], tri- [168, 174, 175] and polyatomic molecules [176, 177]. It has also been used as a means to highlight electron nuclear coupling of degrees of freedom in photoelectron holography [178]. Physically, enhanced ionisation has been partially attributed to a narrower effective-potential barrier for the uphill well due to the presence of a neighbouring, downhill centre.

To better visualise this mechanism, the effective potentials of one-dimensional models of H_2^+ in static fields are shown in Figure 1.1. The addition of an external electric field increases the energy of the upfield potential barrier and decreases that of the downfield potential barrier. Comparing Fig. 1.1 (a) and (b) displays how this energy difference increases with the internuclear distance. It also brings forward the possible physical configurations of the stretched molecule. Indeed, in Fig. 1.1 (a) the central saddle is lower than the Stark saddle (an explanation of saddles is found in Chapter 2.1). In short, even if the wavepacket tunnels through the central barrier, it will remain trapped in the downfield well and the ionisation rate is suppressed. On the other hand, in Fig. 1.1 (b), once the wavepacket has tunnelled through the central barrier it can easily escape to the continuum. Because increasing the internuclear distance also increases the width of the central barrier, at very high

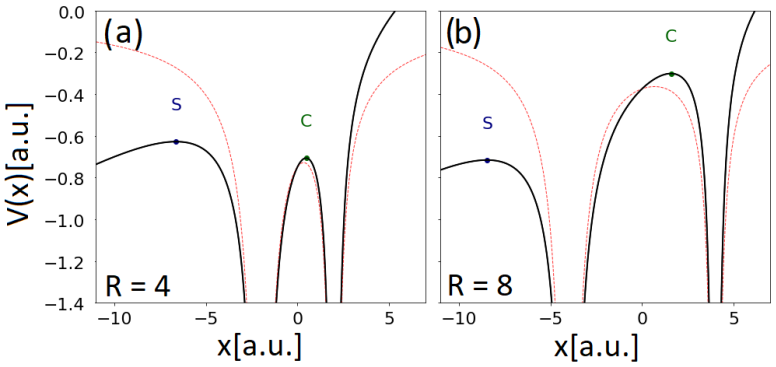

Figure 1.1: The effective potentials of a one-dimensional molecular model of H_2^+ in a static external field of strength $E_0 = 0.0534$ a.u. are shown using inter-nuclear separations of $R = 4$ a.u. and $R = 8$ a.u.. The Stark and the central saddles are indicated by the labels S and C in the figure, and the field-free potentials are given by the dashed red lines.

internuclear distances the ionisation rate is again suppressed. That is why, for specific internuclear distances, when compared with a companion atom of similar ionisation potential, the barrier between the two centers becomes narrower and there is an increase of at least one order of magnitude in the ionisation rate. This narrowing implies that tunnel ionisation will be enhanced for the uphill well. This explanation is strongly based on the quasi-static picture, in which one assumes that the joint influence of the binding potential and the instantaneous driving field form an effective potential barrier. Discussions on the validity of this picture, together with the assumption that the electron tunnels from the uphill well, can be found in [179, 180, 181], and its experimental confirmation has been reported in [182].

Another cause for enhanced ionisation are coupled charge resonant states. Charge resonance occurs when two states produce very similar charge distributions. Nearly degenerate coupled charge-resonant states that occur for large inter-nuclear separations facilitate a strong population transfer to the continuum [162, 166, 183]. On the other hand, for extended systems, multielectron and non-adiabatic effects play an increasingly important role [177, 184, 185](for a recent review see [186, 187]). Loosely speaking, non-adiabaticity implies that the electron probability density as a function of time does not “follow" the field gradients, and instead may be related to population trapping, resonances, multielectron effects and coupling of different degrees of freedom. This type of behaviour has also raised a great deal of debate in the context of the attoclock [188, 129, 189, 190].

One should note, however, that even simple, one-electron systems with only two wells may exhibit non-adiabatic behaviour. For instance, in [191, 75], multiple ionisation bursts that have been identified theoretically do not follow the time profile of the field. This behaviour was attributed to strongly coupled charge resonant states and the system responding non-adiabatically to time dependent fields [76]. In [191, 76], a phase-space analysis has been performed using Wigner quasiprobability

distributions. Thereby, intriguing structures that cycle through momentum space in a quarter of the field cycle have been identified: the momentum gates. As they allow a rapid transfer of population, such gates have been associated to quarter-cycle ionisation bursts, and thus to non-adiabatic following of the time-dependent field [76].

1.4 Structure of the thesis

This thesis is organised as follows. After the overview of phase-space usage in attosecond science and the introduction to enhanced ionisation presented in Chapter 1, we will establish the theoretical frameworks and methods used throughout this work. While chapters will sometimes use different specific tools or frameworks, they are all brought together in Chapter 2, separated by specific sections.

We then in Chapter 3 study enhanced ionisation in stretched molecules. After establishing the system dynamics and the connection between phase-space regions and ionisation rates, we use the Wigner quasi-probability distribution and various initial wavepackets and internuclear distances to investigate momentum gates (structures cycling through the momentum space that do not follow the time-profile of the external field, see sec. 1.3) and their cause. Employing static fields to properly isolate this quantum bridging phenomenon, we focus on its non-classical nature by applying classical phase space arguments (and their limits) and the quantum Liouville equation.

We then aim to expand on the visualisation and interpretation of these quantum effects in Chapter 4 by propagating quantum trajectories with the Quantum Trajectory Method (QTM). In order to perform field derivatives on an unstructured grid, we discretise the density. At the start of the chapter we will introduce improvements to the density approximation and boundary conditions. We will then apply this improved method to atomic tunnel ionisation and enhanced ionisation, emphasising both its interpretational strengths and its computational shortcomings.

From this, we move on to Chapter 5 where we identify the time scales of the quantum bridge and its interplay with the external time-dependent field. This chapter is split into two parts. First, we isolate the effect in a field-free setting allowing the use of analytical methods to obtain the eigenfrequencies at play and their link to the autocorrelation function oscillation frequencies. Following that, we can understand the interplay taking place with the external time-dependent field, whose frequency is lower than that of the quantum bridge.

In Chapter 6, we aim at steering the pathways behind enhanced ionisation. As seen in previous chapters, the interplay between the external field and the quantum bridge is essential for controlling enhanced ionisation and depends on a multitude of parameters. For that reason we will be using machine learning dimensionality

reduction techniques, t-distributed Stochastic Neighbor Embedding (t-SNE) and Principal Component Analysis (PCA), to investigate the entire parameter space simultaneously. This chapter is again separated in two parts. First we perform an initial qualitative analysis of our system in a static field to serve as a proof of concept of the presented dimensional reduction technique. Following that, we apply the t-SNE to the complete time-dependent field case and use the results to guide our qualitative phase-space analysis.

Finally, in Chapter 7 we conclude the thesis with a summary of its main results.

Chapter 2

Theoretical framework and methods

Throughout this chapter we will present an overview of the various tools and methods used throughout this thesis. We focus on simplified, reduced-dimensionality models in which a single spatial dimension is taken into consideration. They provide a transparent, yet accurate picture of the system's dynamics for linearly polarised fields. We also use atomic units (see Appendix A). We employ both classical and quantum-mechanical phase-space tools. We describe both a numerical and analytical method of wavepacket propagation. We will finish of this chapter by giving an introduction to the Quantum Trajectory Method (QTM) and an overview of two machine learning dimensionality reduction techniques.

2.1 Classical phase space dynamics

The following classical phase-space approach is used to determine bound and continuum phase space regions and identify fixed points under different conditions. This is crucial when looking at signatures of strong field tunneling and over-the-barrier ionisation and is done by employing key concepts of the theory of dynamical systems, some of which are briefly stated here. For a more detailed and rigorous discussion please see e.g., [192]. Classically, the phase space dynamics are described by Hamilton's equations

$$\dot{x} = p = \frac{\partial H_{\mathrm{cl}}(p,x)}{\partial p} \tag{2.1.1}$$

$$\dot{p} = -\frac{\partial V_{\mathrm{eff}}}{\partial x} = -\frac{\partial H_{\mathrm{cl}}(p,x)}{\partial x}, \tag{2.1.2}$$

where x and p are the position and canonically conjugate momentum, respectively. The classical Hamiltonian H is defined by

$$H_{\mathrm{cl}}(p,x) = \frac{p^2}{2} + V_{\mathrm{eff}}(x) \tag{2.1.3}$$

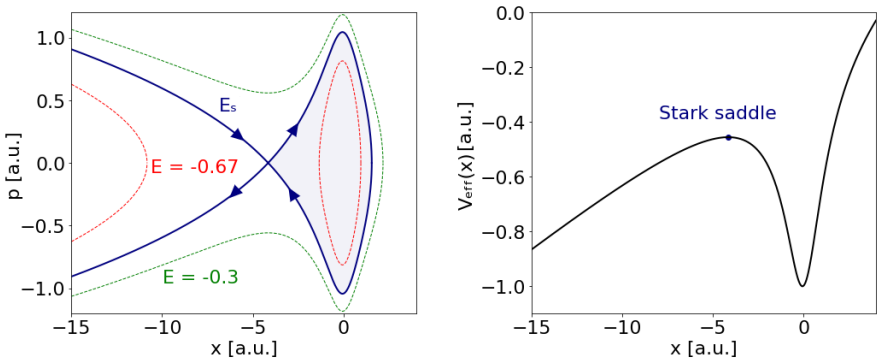

Figure 2.1: Phase portrait for the one-dimensional system defined as an atom with a soft-core potential (2.1.5) in a static field of strength $E_0 = 0.0534$. a.u.[left panels], together with the corresponding effective potential [right panels]. The Stark saddle has corresponding energy $\mathrm{E_S} = -0.46$, which is also the energy of the separatrix. The latter is depicted by the solid line in phase space, while the dashed red and green lines illustrate solutions for energies $E = -0.67$ a.u. and $E = -0.3$ a.u., respectively. The bound region is depicted by the shaded area.

where

$$V_{\text{eff}} = V(x) + V_l. \tag{2.1.4}$$

V_{eff} is the effective potential determined by the external electric field acting on the electronic wave packet. The physical picture of a time-dependent effective potential corresponds to the length gauge and the dipole approximation, which are used throughout this thesis. Thereby, V_l is the potential energy determined by the laser field, which for a field without spatial dependence, reads $V_l = x\mathcal{E}(t)$.

Solutions of Eqs. (2.1.1) and (2.1.2) which stay the same for all times, that is, for which $\dot{x} = \dot{p} = 0$, are fixed points. For conservative Hamiltonian systems of the form (2.1.3) one may show that fixed points are centres or saddles. In phase space, these fixed points are located at $(x_f, p_f) = (x_s, 0)$, where x_s is the value of the coordinate x for which the effective potential V_{eff} is stationary. Centres and saddles are given by the minima and maxima of the effective potential, respectively. Centres are attractive and surrounded by closed orbits, while saddles are semi-stable and help delimit qualitatively different dynamical regions in phase space. For that reason, phase space trajectories crossing saddles are called *separatrices*.

This is exemplified in Figure. 2.1 for a model atom in a static field, i.e. $\mathcal{E}(t) = E_0$. Similar pictures have been provided in [193, 74]. The binding potential $V(x)$ is chosen to be soft-core

$$V_{\text{sc}}(x) = -\frac{1}{\sqrt{x^2 + \lambda}}, \tag{2.1.5}$$

where λ is known as the softening parameter and $\lambda = 1$ is chosen throughout. This removes the singularity at $x = 0$ of the true Coulomb potential, yet remains long-range [194, 195, 196]. This parameter is typically chosen such that the ionisation energy coincides with the ground state of the potential [197]. This soft-core potential

and variations of it will be often used throughout this thesis.

The figure shows two fixed points according to the definition provided above: a centre at the origin, and the Stark saddle to the left, whose positions are determined by the minimum and the maximum of the effective potential $V_{\text{eff}}(x)$, respectively. The figure also shows a separatrix, which corresponds to the stable and unstable manifolds of the Stark saddle. It is associated with the minimum energy to undergo over-the-barrier ionisation. The closed region to the right of the saddle is bound: trajectories within it will propagate along closed orbits. If the particle starts on the left of the Stark saddle, or if it has an energy higher than that of the separatrix, it will be free. This clearly shows that the particle's energy is paramount to defining the continuum regions; the particle being close to the core is not sufficient for describing its dynamics. For a time-dependent field in the parameter range considered throughout this thesis, namely low frequencies and high driving-field intensities, one may assume that the system behaves quasi-statically. This means that one may use the approximation that the phase space configurations discussed for static fields and shown in Fig. 2.1 hold for each instant of time. They will change instantaneously, such that an electron reaching the continuum at different times and propagating in the field will be exposed to a wide range of transient bound and continuum regions. This implies that the time should be included as an additional variable in an extended phase space.

2.2 Wavepacket propagation

In order to facilitate the phase-space analysis and interpretation, in this work we will use a simplified, one-dimensional model as well as the full solution of the time-dependent Schrödinger equation (TDSE),

$$\mathrm{i}\partial_t|\Psi(t)\rangle = \hat{H}|\Psi(t)\rangle, \tag{2.2.1}$$

where the length-gauge Hamiltonian reads

$$\hat{H} = \frac{\hat{p}^2}{2} + \hat{V}_{\text{eff}(\hat{x})}, \tag{2.2.2}$$

with $V_{\text{eff}}(x,t)$ being defined as above and the hats denoting operators. Depending on the problem at hand, we choose different initial potentials $V_{\text{eff}}(x)$. The evolution of the wavepacket is given by solving the TDSE in the position space, which reads

$$i\partial_t\Psi(x,t) = \left(-\frac{1}{2}\frac{\partial^2}{\partial x^2} + V_{\text{eff}}(x,t)\right)\Psi(x,t), \tag{2.2.3}$$

where $\Psi(x,t)$ is the time-dependent wave function. We solve the TDSE numerically using the split-operator method [198]. Therein, propagation steps are split

up between the potential and kinetic operator and treated in coordinate and momentum space respectively. Unless stated otherwise, the time step, length grid and momentum grid precision used are respectively dt = 0.1 a.u., dx = 0.2 a.u. and dk = 0.05 a.u..

Throughout this work, we will approximate the initial wave function by Gaussian wave packets

$$\Psi(x,0) = \langle x|\Psi(0)\rangle = \left(\frac{\gamma}{\pi}\right)^{\frac{1}{4}} \exp\left\{-\frac{\gamma}{2}(x-q_0)^2 + ip_0(x-q_0)\right\} \tag{2.2.4}$$

of width γ centred at vanishing initial momentum $p_0 = 0$ and initial coordinate q_0, or coherent superpositions thereof. Gaussian wave packets are widely used in several areas of knowledge, and have the advantage of facilitating computations and often allowing analytic treatments. This is very helpful from the interpretational viewpoint. The width of $\Psi(x,0)$ ($\gamma = 0.5$ a.u.) has been calculated such that the ground-state energy of a field free single-centre soft-core potential with $\lambda = 1.0$ is minimised. This ground state energy is $E_{\text{sc}} = -0.67$ a.u..

The time-dependent wave function will be used to calculate the time dependent autocorrelation function

$$a(t) = \int \Psi^*(x,t)\Psi(x,0)dx, \tag{2.2.5}$$

which is given by the overlap integral between the initial and time propagated wave function. The autocorrelation function is a relevant quantity that provides insight into the resulting wave function time dynamics and will be employed to assess the behaviour of the system in time-dependent electric fields.

2.3 Quantum distribution functions

Wigner quasiprobability distributions, within the constraints posed by the uncertainty principle, permit the study of position-momentum correlations (for reviews see, e.g., [199, 1]). Wigner functions have been widely employed in quantum optics and quantum information, and more sparsely in strong-field and attosecond physics. See for instance studies of ionisation [74, 191, 76, 77], rescattering [79, 87] and entanglement [88] in this context. One should also note that quantum distribution functions may be defined using any two variables corresponding to incompatible observables, such as time and frequency. For instance, Wigner-type time-energy distributions were employed to study HHG [200], different regimes in ATI [201] and autoionisation [85].

The time-dependent wave function is used as input in the Wigner quasiproba-

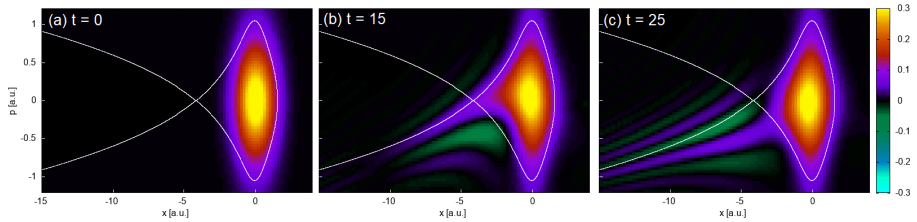

Figure 2.2: Wigner quasiprobability distribution for the one-dimensional system defined as an atom with a soft-core potential (2.1.5) in a static field of strength $E_0 = 0.0534$. a.u. The initial wavefunction used is a Gaussian wavepacket of width $\gamma = 0.5$. The snaphots shown are taken at times (a) t = 0, (b) t = 15 and (c) t = 25. The separatrix is depicted by the solid white line in phase space.

bility distribution

$$W(x,p,t) = \frac{1}{\pi}\int_{-\infty}^{\infty} d\xi \Psi^*(x+\xi,t)\Psi(x-\xi,t)e^{2ip\xi}, \tag{2.3.1}$$

where ξ is a dummy variable. This function is real, normalised, and provides momentum and position resolution within the constraints posed by the uncertainty principle. Additionally, its marginals correspond to physical probability distributions for each conjugate variable, respectively. However, it exhibits both positive and negative values, hence the name "quasiprobability". This, among other features, makes its interpretation as a probability distribution difficult [199]. On the other hand, its deviations from probability densities can be used to indicate non-classicality [19]. For instance, a widespread definition used in quantum optics is to seek regions for which $W(x,p,t)$ is negative and classify them as non-classical [202].

To illustrate the phase space signatures of ionisation, we propagate a Gaussian wavepacket of width $\gamma = 0.5$ using the TDSE following the method described in section 2.2. In Fig. 2.2 we show the resulting Wigner quasiprobabilty distribution as well as the associated classical separatrix. Quantum mechanically there will always be an uncertainty for the initial wavepacket, which manifests itself as a phase space spread in Figure. 2.2 (a). The initial quasiprobability distribution is positive throughout phase space. For a static field and ionisation from a single centre, the Wigner function always follows or is partly contained by classical separatrices [77]. This happens to its bound part as well as the signature semiclassical tail seen in Figure 2.2 (b) associated either with over-the-barrier or tunnel ionisation discussed in [74] (see also [193] for a seminal discussion of such features in the context of quantum localisation). It follows the separatrix and crosses from the bound to the continuum region around the Stark saddle (the saddle formed by the interplay of the field and the potential). For longer times, shown in Figure. 2.2 (c), the tail moves to lower momenta and the quasiprobability distribution exhibits interference fringes associated with the quantum interference between different ionisation events. Under many circumstances this even means that the electron reaches the continuum

with non-vanishing momenta, although it follows an equienergy curve and thus the field gradient. This oscillating behaviour around the separatrix has been identified in other areas of research as the semiclassical limit of the Wigner function's time evolution [135].

To investigate the time evolution of the Wigner function as well as a more restrictive definition of its non-classicality, we will use the quantum Liouville equation [13].

$$\left(\frac{\partial}{\partial t}+\frac{p}{M}\frac{\partial}{\partial x}-\frac{dV_{\text{eff}}(x)}{dx}\frac{\partial}{\partial p}\right)W(x,p,t)=Q(x,p,t), \tag{2.3.2}$$

where

$$Q(x,p,t)=\sum_{l=1}^{\infty}\frac{(-1)^l(\hbar/2)^{2l}}{(2l+1)!}\frac{d^{2l+1}V_{\text{eff}}(x)}{dx^{2l+1}}\frac{\partial^{2l+1}}{\partial p^{2l+1}}W(x,p,t) \tag{2.3.3}$$

are the quantum corrections to the classical Liouville equation. The quantum Liouville equation (also known as Moyal equation) may also be written more compactly as

$$\frac{\partial W(x,p,t)}{\partial t}=-\{\{W(x,p,t),H(x,p,t)\}\}, \tag{2.3.4}$$

where $H(x,p,t)$ is the system's Hamiltonian and $\{\{\cdot\}\}$ give a Moyal bracket [203, 204][1]. In the classical limit (setting $\hbar=0$), Eqs. (2.3.2) and (2.3.4) become the classical Liouville equation, such that $Q(x,p,t)=0$ and the right-hand side of Eq. (2.3.4) will be given by a Poisson bracket. In this case, the Wigner quasiprobability distribution will evolve like a classical entity. This is a useful tool for distinguishing between regimes in which quantum interference is present, but evolves classically by, for instance, following classical separatrices, and those truly quantum regimes with no classical counterpart. A widespread approach in quantum optics and cold gases, known as the truncated Wigner approximation (TWA), is to consider the classical Liouville equation with stochastic quantum corrections. This correction is required many times in order to deal with large systems. The TWA was first used in the context of Bose-Einstein condensates in [46]; for reviews see [36, 32], and is closely related to the linearised semiclassical IVR [41, 33]. Nonetheless, in some instances it may be nontrivial to compute a classical limit for the quantum Liouville (Moyal) equation (see [7] for an early discussion).

A direct inspection of Eq. (2.3.3) shows that the quantum corrections vanish for binding potentials up to the second order in x. This includes linear potentials such as the interaction Hamiltonian in $V_{\text{eff}}(x)$ and harmonic potentials.

By computing the value of $Q(x,p,t)$ from Eq.2.3.2, we aim to determine zones of non-classical time evolution of the Wigner function. In order to test this, shown in Fig. 2.3 are the quantum corrections of a harmonic oscillator as well as anharmonic oscillators

[1]Moyal brackets map non-commuting operators to functions in phase space and have been used in a wide range of problems; for instance, non-Hermitian Hamiltonian systems [205].

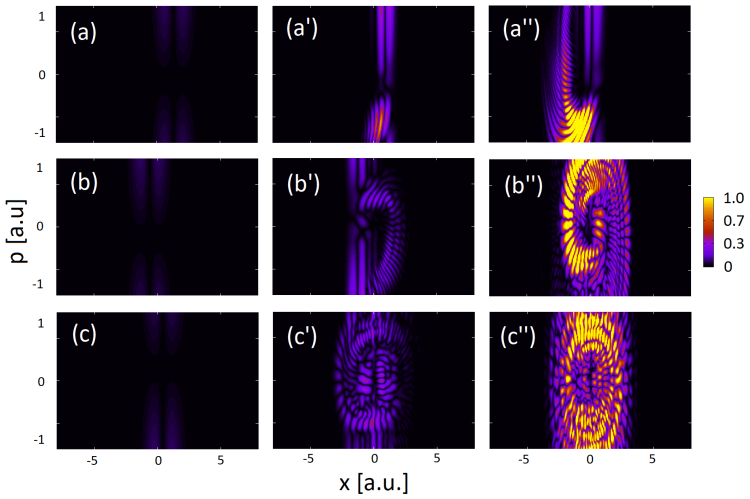

Figure 2.3: Quantum corrections for the harmonic oscillator (left panel), anharmonic oscillator following Eq. (2.3.5) with $\lambda = 0.2$ (middle panel) and $\lambda = 0.8$ (right panel), at times from top to bottom $t = 0.5$ (a), $t = 2$ (b) and $t = 5$ (c)

$$V_h(x) = 0.5x^2 + \lambda x^4 \tag{2.3.5}$$

with increasing levels of anharmonicity. As expected from Eq. (2.3.3) the quantum corrections are mostly absent when using the displaced harmonic oscillator. Not only do the quantum corrections appear when using an anharmonic oscillator, but they also increase with λ, the amount of anharmonicity.

There are however very faint quantum corrections for the harmonic oscillator at high momentum regions. When looking at the Wigner function for the harmonic oscillator (not shown) we note that the quasiprobability distribution is absent in these regions with faint quantum corrections. Since these are derived computationally with derivatives, this suggests a computational limitation when the quasiprobability distributions is near zero. Indeed, in Fig. 2.4, when the quantum corrections are multiplied by the absolute value of the Wigner function, the corrections are as expected completely absent for the harmonic oscillator. In conclusion, one must make sure the region with quantum corrections is one where the Wigner function is present in order to avoid computational errors.

2.4 The quantum trajectory method

Throughout Chapter 4 we will be using the quantum trajectory method (QTM) with the aim to analyse and understand non-classicality in strong field enhanced ionisation. In contrast to the more standard classical or semiclassical trajectory based methods used in strong field physics (see for example [53, 54, 55, 33, 45, 138, 77, 144, 145]), here the *exact* equations of quantum mechanics are solved in a similar fashion to Bohmian mechanics. These trajectories are highly non-classical,

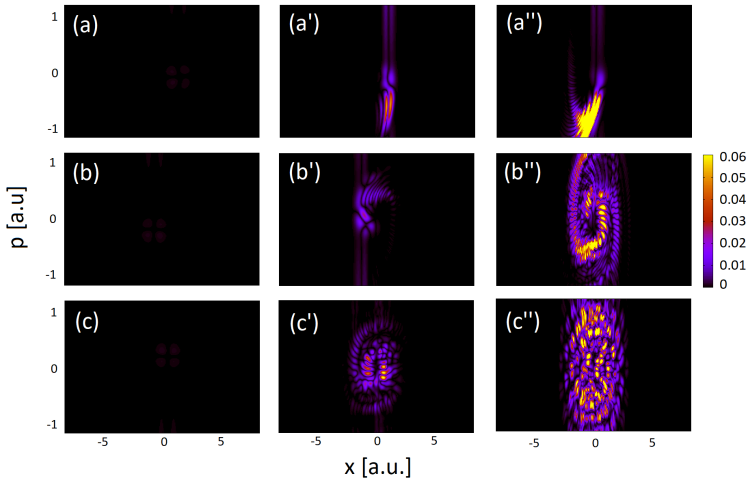

Figure 2.4: Quantum corrections scaled with the absolute value of the Wigner function for the harmonic oscillator (left panel), anharmonic oscillator following Eq. (2.3.5) with $\lambda = 0.2$ (middle panel) and $\lambda = 0.8$ (right panel), at times from top to bottom $t = 0.5$ (a), $t = 2$ (b) and $t = 5$ (c)

as a single Bohmian trajectory can be related to an ensemble of classical trajectories [206, 207]. The trajectories in QTM are equivalent to Bohmian trajectories, although they are computed differently as explained later in this chapter. For a detailed overview of quantum trajectories in this context, see [208]. In the following section we will go through an introduction of the key equations of the QTM as well as its implementation using a discrete representation of the density, starting from Madelung's derivation of the hydrodynamic equations [209]:

In the one-dimensional time dependent Schrödinger equation (TDSE),

$$i\partial_t \Psi(x,t) = \left(-\frac{1}{2}\frac{d^2}{dx^2} + V(x)\right)\Psi(x,t), \tag{2.4.1}$$

the complex valued time dependent wave function $\Psi(x,t)$ is written in polar form

$$\Psi(x,t) = R(x,t)e^{\frac{iS(x,t)}{\hbar}}, \tag{2.4.2}$$

where $S(x,t)$ is the phase and $R(x,t)$ the amplitude, both real. The probability density is defined by $\rho(x,t) = [R(x,t)]^2$. By inserting the polar form into the TDSE one obtains the hydrodynamic equations of motion, which are two coupled partial differential equations: the quantum Hamilton-Jacobi equation

$$\frac{-\partial S(x,t)}{\partial t} = \frac{1}{2m}\left[\frac{\partial S(x,t)}{\partial x}\right]^2 + V(x) + Q(x,t), \tag{2.4.3}$$

where

$$Q(x,t) = -\frac{\hbar^2}{4m}\left[\frac{\rho''(x,t)}{\rho(x,t)} - \frac{1}{2}\left[\frac{\rho'(x,t)}{\rho(x,t)}\right]^2\right] \tag{2.4.4}$$

is the quantum potential, and the continuity equation

$$\frac{\partial \rho(x,t)}{\partial t} = -\frac{\partial}{\partial x}[\rho(x,t)v(x,t)], \tag{2.4.5}$$

where the flow velocity of the probability fluid

$$v(x,t) = \frac{1}{m}\frac{\partial S(x,t)}{\partial x}, \tag{2.4.6}$$

constrains the velocity of the quantum trajectories, forcing them to follow specific lines determined by the gradient of the phase. The fact that this physical system is composed of both a wavefunction and a quantum particle guided by that wavefunction is a postulate [210].

From a computational perspective, the essence of QTM [208] is to propagate the trajectories directly instead of first solving the TDSE. This is different from Bohmian mechanics, where the TDSE is computed first conventionally and Bohmian trajectories are then propagated using the wavefunction. The former avoids the difficulties of increased dimensionality that arises when computing the wavefunction on a fixed grid. Taking the gradient on both sides of the quantum Hamilton-Jacobi equations and writing the total derivative as $\frac{d}{dt} = \frac{\partial}{\partial t} + v\frac{\partial}{\partial x}$, one obtains a Newton-like equation of motion

$$m\frac{d^2x}{dt^2} = -\nabla[V(x) + Q(x,t)], \tag{2.4.7}$$

where the force is split into a classical and quantum contribution. All non-local effects come into play via the quantum potential, named as such from having no classical analog. We then obtain a Lagrangian version of the quantum Hamilton-Jacobi equation and the continuity equation:

$$\frac{dS(x,t)}{dt} = \frac{1}{2m}\left[\frac{\partial S(x,t)}{\partial x}\right]^2 - V(x) - Q(x,t) \tag{2.4.8}$$

$$\frac{d\rho(x,t)}{dt} = -\rho(x,t)\frac{\partial v(x,t)}{\partial x} \tag{2.4.9}$$

The quantum trajectories can therefore be propagated without directly evaluating the wavefunction at each time step, and instead using Eq. (2.4.7). This however requires calculating field derivatives on unstructured grids, which is an especially relevant issue when looking at larger systems, such as molecules, and so a number of techniques have been implemented to attempt to overcome these issues [208].

2.4.1 Discrete approximation

Here, an approach that parameterised the density developed by [211] and expanded by [212, 213] is summarised. An expression for the quantum force and quantum

potential is derived from the discrete approximation of the density

$$\rho(x_n) = \rho_-(x_n) \approx \rho_+(x_n), \tag{2.4.10}$$

written for simplicity as $\rho_-(x_n) = \frac{1}{N(x_n - x_{n-1})}$ and $\rho_+(x_n) = \frac{1}{N(x_{n+1} - x_n)}$, where N is the number of trajectories and x_n the position of the nth trajectory such that $x_1 < x_2 < ... < x_N$.

The derivative of a function in 1D is approximated using the finite difference method [214] at $x = x_n$ by either

$$\varphi'(x_n) \approx \frac{\varphi(x_{n+1}) - \varphi(x_n)}{x_{n+1} - x_n} \approx \frac{\varphi(x_n) - \varphi(x_{n-1})}{x_n - x_{n-1}}, \tag{2.4.11}$$

called respectively the forward and backward scheme. To conserve information from the neighbouring trajectories in both directions, $\rho^{'}(x,t)$ is calculated using either the forward scheme on $\rho_-(x_n)$ or the backward scheme on $\rho_+(x_n)$. Both yield

$$\frac{\rho^{'}(x,t)}{\rho(x,t)} = \frac{1}{(x_{n+1} - x_n)} - \frac{1}{(x_n - x_{n-1})}, \tag{2.4.12}$$

which is then used in the quantum potential [211]. This gives

$$Q_0(x_n,t) = \frac{\hbar^2}{8m}\left[\frac{1}{(x_{n+1} - x_n)} - \frac{1}{(x_n - x_{n-1})})\right]^2, \tag{2.4.13}$$

which is then later used to derive the quantum force. Here the $\frac{\rho^{''}(x,t)}{\rho(x,t)}$ term has been neglected as it does not influence the quantum force, only the potential. However the quantum potential is crucial when calculating the energy and all phase related phenomena. This is shown by the work of [212, 213]. Again a forward or backward scheme can be used to calculate the second derivative. Using first a forward scheme, followed by a backward scheme for the first derivative, one obtains

$$\varphi^{''}(x_n) = \frac{\varphi^{'}(x_{n+1}) - \varphi^{'}(x_n)}{x_{n+1} - x_n}, \tag{2.4.14}$$

$$\varphi^{''}(x_n) = \frac{\frac{\varphi(x_{n+1}) - \varphi(x_n)}{x_{n+1} - x_n} - \frac{\varphi(x_n) - \varphi(x_{n-1})}{x_n - x_{n-1}}}{x_{n+1} - x_n}, \text{and} \tag{2.4.15}$$

$$\frac{\rho^{''}(x,t)}{\rho(x,t)} = \frac{\rho_+(x_{n+1})}{\rho_+(x_n)}\frac{1}{(x_{n+1} - x_n)^2} - \frac{1}{(x_{n+1} - x_n)^2} - \frac{1}{(x_{n+1} - x_n)(x_n - x_{n-1})} + \frac{\rho_+(x_{n+1})}{\rho_+(x_n)}\frac{1}{(x_{n+1} - x_n)(x_n - x_{n-1})}. \tag{2.4.16}$$

This ratio is used to obtain the quantum potential,

$$Q_{CR}(x_n,t) = -\frac{\hbar^2}{4m}\left[\frac{1}{(x_{n+2}-x_{n+1})(x_{n+1}-x_n)} - \frac{1}{(x_{n+1}-x_n)(x_n-x_{n-1})}\right.$$
$$\left. -\frac{1}{(x_{n+1}-x_n)^2} + \frac{1}{(x_n-x_{n-1})^2} - \frac{1}{2}\left(\frac{1}{(x_{n+1}-x_n)} - \frac{1}{(x_n-x_{n-1})}\right)^2\right] \tag{2.4.17}$$

To propagate the trajectories the quantum force F_q is used

$$F_q(x_n,t) = -\frac{\partial Q(x,t)}{\partial x_n} = -\frac{\partial}{\partial x_n}\sum_{i=1}^{N} Q(x_i,t) = -\frac{\partial}{\partial x_n}\sum_{i=n-2}^{n+1} Q(x_i,t) \tag{2.4.18}$$

Starting from the $\frac{\rho'(x,t)}{\rho(x,t)}$ part and keeping only terms with deriving x_n (all others will go to zero after the partial differentiation), we obtain

$$\begin{aligned}\sum_{i=n-1}^{n+1}\left(\frac{\rho'(x_i,t)}{\rho(x_i,t)}\right)^2 &= \sum_{i=n-1}^{n+1}\frac{1}{(x_{i+1}-x_i)^2} + \frac{1}{(x_i-x_{i-1})^2} - \frac{2}{(x_{i+1}-x_i)(x_i-x_{i-1})}\\ &= \frac{1}{(x_n-x_{n-1})^2} - \frac{2}{(x_n-x_{n-1})(x_{n-1}-x_{n-2})} + \frac{1}{(x_{n+1}-x_n)^2}\\ &\quad + \frac{1}{(x_n-x_{n-1})^2} - \frac{2}{(x_{n+1}-x_n)(x_n-x_{n-1})} + \frac{1}{(x_{n+1}-x_n)^2}\\ &\quad - \frac{2}{(x_{n+2}-x_{n+1})(x_{n+1}-x_n)}\end{aligned}$$

This leads to the force

$$\begin{aligned}F_q(x_n,t) &= -\frac{\hbar^2}{8m}\frac{\partial}{\partial x_n}\sum_{i=n-2}^{n+1}\left(\frac{\rho'(x_i,t)}{\rho(x_i,t)}\right)^2\\ &= \frac{\hbar^2}{4m}\left[\frac{2}{(x_n-x_{n-1})^3} - \frac{x_{n-1}-x_{n-2}}{(x_n-x_{n-1})^2(x_{n-1}-x_{n-2})^2} - \frac{2}{(x_{n+1}-x_n)^3}\right.\\ &\quad \left. -\frac{x_{n+1}-2x_n+x_{n-1}}{(x_{n+1}-x_n)^2(x_n-x_{n-1})^2} + \frac{x_{n+2}-x_{n+1}}{(x_{n+2}-x_{n+1})^2(x_{n+1}-x_n)^2}\right]\\ &= \frac{\hbar^2}{4m}\left[-\frac{2}{(x_{n+1}-x_n)^3} + \frac{1}{(x_{n+2}-x_{n+1})(x_{n+1}-x_n)^2}\right.\\ &\quad -\frac{1}{(x_{n+1}-x_n)(x_n-x_{n-1})^2} + \frac{1}{(x_{n+1}-x_n)^2(x_n-x_{n-1})}\\ &\quad \left. +\frac{2}{(x_n-x_{n-1})^3} - \frac{1}{(x_n-x_{n-1})^2(x_{n-1}-x_{n-2})}\right]\end{aligned}$$

.

$$F_q(x_n,t) = \frac{\hbar^2}{4m}\left[\frac{1}{(x_{n+1}-x_n)^2}\left(\frac{1}{(x_{n+2}-x_{n+1})} - \frac{2}{(x_{n+1}-x_n)} + \frac{1}{(x_n-x_{n-1})}\right) - \frac{1}{(x_n-x_{n-1})^2}\left(\frac{1}{(x_{n+1}-x_n)} - \frac{2}{(x_n-x_{n-1})} + \frac{1}{(x_{n-1}-x_{n-2})}\right)\right] \tag{2.4.19}$$

We will be able to effectively propagate quantum trajectories by either using these expressions or by improving them for greater accuracy in Chapter 4.

2.5 Analytical propagation

When looking at a field-free system in Chapter. 5, we will supplement our numerical results with the insight of interpretational power of the analytical model in [215]. It provides an alternative quantisation condition for wavepacket dynamics in hyperbolic double well potentials of arbitrary height or width. A short summary of the method along with the relevant equations for Chapter 5 are described below.

We will consider the evolution of a time-dependent wave packet $\Psi(x,t)$ using the basis of eigenstates $\psi_n(x)$ that solve the time-independent Schrödinger equation (TISE)

$$H\psi_n(x) = E_n\psi_n(x), \tag{2.5.1}$$

with the Hamiltonian defined by

$$H = \frac{p^2}{2m} + V(x). \tag{2.5.2}$$

The binding potential

$$V(x) = -V_0\frac{\sinh^4(x/d)}{\cosh^6(x/d)} \tag{2.5.3}$$

is a double well (bistable) potential where V_0 specifies the depth of the potential and d its peak location. In the eigenbasis of the TISE,

$$\Psi(x,t) = \sum_n \Lambda_n \exp(-iE_nt/\hbar)\psi_n(x), \tag{2.5.4}$$

where

$$\Lambda_n = \int \Psi(x,0)\psi_n^*(x)dx \tag{2.5.5}$$

are overlap integrals between the initial wavepacket $\Psi(x,0)$ and eigenfunctions $\psi_n(x)$ of the hyperbolic double well. The 1D time-independent Schrödinger equation (TISE) for the potential given in Eq. (2.5.3) reads as

$$\frac{d^2\psi(z)}{dz^2} + \left(\epsilon d^2 + U_0d^2\frac{\sinh^4(z)}{\cosh^6(z)}\right)\psi(z) = 0, \tag{2.5.6}$$

with dimensionless parameters $z = x/d$, $U_0 = 2mV_0/\hbar^2$, $\epsilon = 2mE/\hbar^2$. Note that the potential $V(x)$ has even parity, which implies the existence of even/odd parity wavefunctions.

The Schrodinger equation is then reduced to Heun's equation. Indeed it was shown [216] that for even parity wavefunctions the above equation may be reduced to the Heun confluent differential equation by introducing the new variable $\xi = 1/\cosh^2 z$ (with $0 < \xi \leq 1$ as $-\infty < z < +\infty$), that is,

$$\frac{d^2}{d\xi^2}H(\xi) + \left(\alpha + \frac{\beta+1}{\xi} + \frac{\gamma+1}{\xi-1}\right)\frac{d}{d\xi}H(\xi) + \left(\frac{\mu}{\xi} + \frac{v}{\xi-1}\right)H(\xi) = 0, \tag{2.5.7}$$

where the even-parity solutions to TISE are of the following form:

$$\psi_{even}(\xi) = \xi^{\beta/2}e^{\alpha\xi/2}H(\alpha,\beta,\gamma,\delta,\eta,\xi), \tag{2.5.8}$$

with $\alpha = -d\sqrt{U_0} < 0$, $\beta = -id\sqrt{\epsilon} > 0$ and others given by $\gamma = -\frac{1}{2}$, $v = \frac{1}{4}(\alpha+\beta(\beta+1))$, $\delta = \mu + v - \frac{\alpha}{2}(\beta+\gamma+2)$, $\mu = \frac{1}{4}(\alpha(\alpha+2)+2\alpha\beta-\beta(\beta+1))$, $\eta = \frac{\alpha}{2}(\beta+1) - \mu - \frac{1}{2}(\beta+\gamma+\beta\gamma)$.

Furthermore, following the similar procedure as above but using the exchange of variables $\zeta = \tanh(x/d)$ (with $-1 < \zeta < 1$ as $-\infty < z < +\infty$) it may be found [216] that

$$\psi_{odd}(\zeta) = \zeta\left(1-\zeta^2\right)^{\beta/2}e^{-\frac{\alpha}{2}\zeta^2}H(-\alpha,-\gamma,\beta,-\delta,\eta+\frac{\alpha^2}{4},\zeta^2) \tag{2.5.9}$$

where $H(-\alpha,-\gamma,\beta,-\delta,\eta+\frac{\alpha^2}{4},\zeta^2)$ is again a Heun's function, only mapping $\alpha \to -\alpha$, $\beta \to -\gamma$, $\gamma \to \beta$, $\delta \to -\delta$, $\eta \to \eta + \frac{\alpha^2}{4}$. Note, that in contrast to $x \to \xi$, the $x \to \zeta$ transformation intrinsically constrains the wavefunctions to be odd in x-space.

Using the quantisation condition provided in [215], we obtain the eigenvalues E_n (and hence eigenfrequencies ω_n) and find the eigenfunctions given by Eqs. (2.5.8) for these allowed energies.

We then formulate the initial wavepackets to be placed in a hyperbolic double well. We would like to benefit from the relatively simple forms of the eigenfunctions in ξ-spaces and to devise the simple purely even initial wavepackets in ξ-spaces. In this way the intricate[2] overlap integrals from x-spaces can be evaluated in ξ-spaces by introducing the appropriate weight function $q(\xi)$ to the integrals. In ξ-space, noting that $d\xi/dz = -2\sinh(z)/\cosh^3(z)$ we obtain

$$dx = \frac{d}{-2\xi\sqrt{1-\xi}}d\xi = -q(\xi,d)d\xi. \tag{2.5.10}$$

[2]For example, the even-parity eigenfunctions from Eq. (2.5.8) when evaluated in x-space become $\psi(x) = (1/cosh^2(x/d))^{\beta/2}e^{\alpha(1/2cosh^2(x/d))}H(\alpha,\beta,\gamma,\delta,\eta,1/cosh^2(x/d))$

We will utilise an even-parity, delocalised initial wavepacket $\Psi(\xi,0)=\psi_{\mathrm{DLE}}(\xi,c,\Omega)$ which explicitly reads

$$\psi_{\mathrm{DLE}}(\xi,c,\Omega)=\frac{\xi^{c\Omega}e^{-c\xi}}{\sqrt[4]{\pi}\sqrt{{}_1\tilde{F}_1\left(2c\Omega;2c\Omega+\frac{1}{2};-2c\right)}\sqrt{\Gamma(2c\Omega)}}, \tag{2.5.11}$$

with $0<\Omega<1$ specifiying the location of the peak; $c>0$ specifying the width of the wavepacket; ${}_1\tilde{F}_1(a,b,c)$ denoting regularised confluent hypergeometric function and $\Gamma(u)$ complete gamma function. The x-space peaks location of the even delocalised wavepacket can be retrieved from Ω by inverting the $x\rightarrow\xi$ mapping to produce $x=\pm d\cosh^{-1}\left(1/\sqrt{\Omega}\right)$.

The overlap integrals Eq.(2.5.5) Λ_n are therefore evaluated analytically for n=0,2,4,.. from

$$\Lambda_n=\int_0^1\psi^*_{\mathrm{DLE}}(\xi,c,\Omega)\psi_n(\xi)q(\xi,d)d\xi. \tag{2.5.12}$$

2.6 Dimensionality reduction

When dealing with a system of multiple parameters, it can be very useful to look at the entire parameter space at once. The main challenge to overcome when studying the effect of a large number of parameters simultaneously is how to visualise the results. To do so throughout Chapter 6 we will be using the following machine learning dimensional reduction techniques. Indeed, each data point will exist in a high-dimensional space (the number of dimensions equal to the number of parameter used), and ideally we would like to project our results down to a two-dimensional space.

2.6.1 Principal Component Analysis

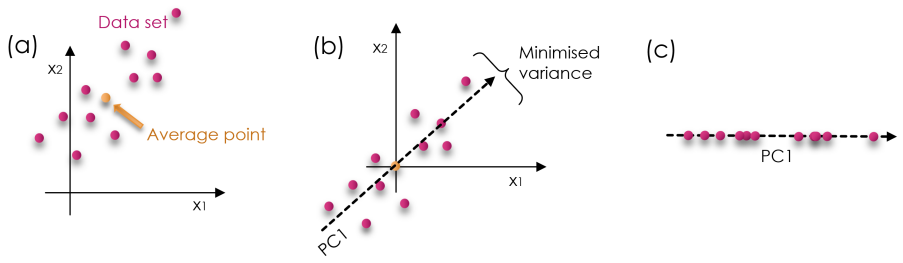

Figure 2.5: Schematic representation of a 2-dimensional data set reduction to 1-dimension using PCA. (a) Original data set in red along with the variable average represented in orange. (b) Mean-centered data set along with the first principal component minimising the average squared distances. (c) Data set recast onto the first principal component.

Principal Component Analysis (PCA) is a common way to reduce the dimensions of our data while keeping the overall trends and patterns. A schematic representation

of PCA is shown in Figure 2.5.

The essence of PCA is to compute the principal components of a collection of points. The principal components are a sequence of unit vectors. The $i-th$ principal component is chosen such that its direction minimises the average squared distance from the data points to the principal component line, while being orthogonal to the previous $i-1$ vectors. In other words, the first principal component can be defined as the direction that maximises the variance of the projected data. We can then use the first two principal components to perform a change of basis on the data.

From the definition above, the principal components are the eigenvectors of the data's covariance matrix. They are obtained from the following steps:

1. We consider our data to be in the form of a matrix X with n rows and k columns. The k columns represent the different parameters of our data, while the rows n represent the different data points computed.

2. We standardize (subtract the mean and divide by standard deviation) the initial variables such that they contribute equally to the analysis. This is critical because PCA is sensitive to the variance of the initial variables.

3. Compute the covariance matrix of the standardized data.

4. Compute the eigenvectors and eigenvalues of the covariance matrix.

5. Recast the data along the first two principal component axes.

2.6.2 T-Distributed Stochastic Neighbor Embedding

Another dimensional reduction technique is the t-Distributed Stochastic Neighbour Embedding (t-SNE). It is an unsupervised machine learning technique, meaning it will find overall trends and patterns without any prior knowledge on the origin of the data. A detailed explanation of the workings of the t-SNE method can be found in [217]. It is summarised here and divided into three steps:

1. Defining a probability distribution p_{ij} of picking a pair of points (x_i, x_j) in our original high dimensional space such that neighbouring points lead to a higher probability. This is done by defining the conditional probability $p_{i|j}$ of a point x_j being picked after choosing x_i by

$$p_{i|j} = \frac{\exp(-||x_i - x_j||^2)/2\sigma_i^2}{\sum_{k \neq i} \exp(-||x_i - x_k||^2/2\sigma_i^2)}. \tag{2.6.1}$$

   The conditional probability is represented by a Gaussian distribution of the Euclidean distance between points x in high dimensional space. The Gaussian is centred at x_i, has standard deviation σ_i, and is normalised in order to handle clusters of different densities. The conditional probability $p_{i|i} = 0$.

From these conditional probabilities we create the joint distribution p_{ij}

$$p_{ij} = \frac{p_{i|j} + p_{j|i}}{2n} \tag{2.6.2}$$

where n is the number of data points. The symmetric property of the pairwise similarities ($p_{ij} = p_{ji}$) helps simplify the calculation at the third stage of the algorithm. The joint distribution is one of the major improvements between the SNE and the t-SNE.

2. Creating a random dataset of points y in the target dimension and calculating, similarly to step 1, the joint probability distribution q_{ij} of picking a pair of points (y_i, y_j)

$$q_{ij} = \frac{(1 + ||y_i - y_j||^2)^{-1}}{\sum_{k \neq l}(1 + ||y_k - y_t||^2)^{-1}}. \tag{2.6.3}$$

However, instead of a Gaussian distribution, q_{ij} is represented by the Student's t-distribution with one degree of freedom (equivalent to a Cauchy distribution), which is much more heavy-tailed. The Cauchy distribution is chosen instead of a Gaussian in order to prioritise preserving local structure. Indeed, for data that is intrinsically high-dimensional, pair-wise distances can never all be preserved. By using a heavy-tail distribution, we compromise by allowing dissimilar points in high dimension to be modelled too far apart in the low dimensional map. Additionally, because intermediate distances in high dimensional space become extreme in the target dimension, this helps prevent crowding in the final distribution. Incidentally this is another improvement from the SNE.

3. Modifying the dataset y in the target dimension such that q_{ij} is as similar as possible to p_{ij}. This is done by defining a cost function C

$$C = KL(P||Q) = \sum_i \sum_j p_{ij} log \frac{p_{ij}}{q_{ij}} \tag{2.6.4}$$

chosen to be the Kullback–Leibler divergence (KL divergence) [218] between the two distributions. The KL divergence is a measure of how different two distributions are to one another. We then minimise the cost function C using the gradient descent method. This involves taking a stochastic sampling of the cost function and obtaining the gradient

$$\frac{\delta C}{\delta y_i} = 4 \sum_j (p_{ij} - q_{ij})(y_i - y_j)(1 + ||y_i - y_j||^2)^{-1} \tag{2.6.5}$$

for a small batch of samples. The gradient is then scaled by the learning rate (often referred to as step size) and used to modify the target dataset

y. This procedure is then repeated over many steps, which approximates the true gradient and successfully minimises the cost function. For a more detailed explanation of the stochastic gradient descent method see [219].

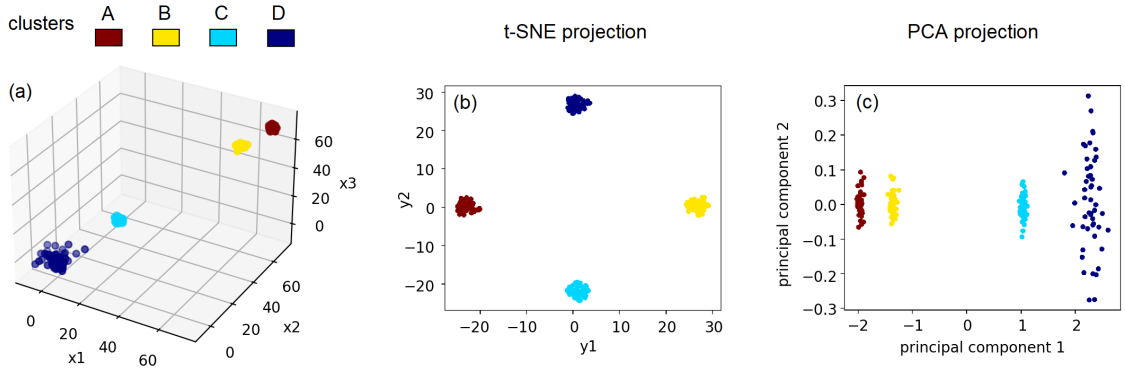

Figure 2.6: 3-dimensional plot of four Gaussian clouds in (a) along with its 2-dimensional t-SNE projection in (b) and PCA projection in (c). The four clusters A B C D are shown by different colors, red, yellow, light blue and dark blue respectively. Cluster D is four times more dispersed than clusters A B and C. The distance between clusters A and B is two times shorter than that between C and D and four times shorter between B and C.

Throughout Chapter 6 we will be mainly using t-SNE dimensional reduction while also comparing those results with a PCA projection. The reason behind using both distributions is that they have very different strengths and limitations and therefore provide complementary information on the initial multi-dimensional dataset. For instance, PCA is deterministic while the t-SNE is stochastic and uses

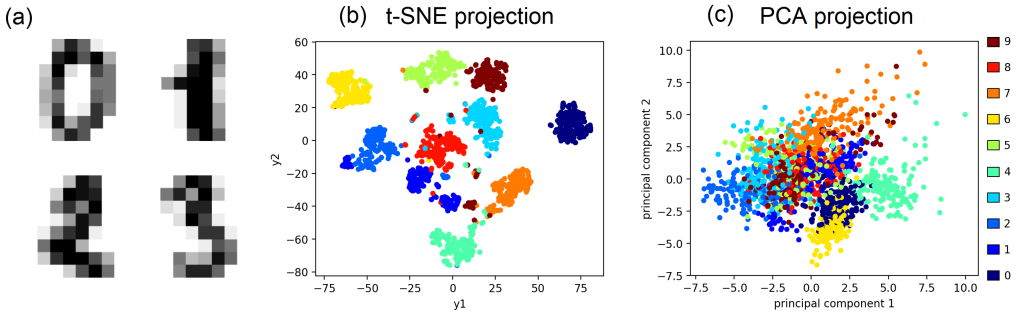

Figure 2.7: Projection of a handwritten digits dataset from 64-dimensions down to 2-dimensions. The four sub-figures in (a) show examples of different possible data points. Each data point is an 8x8 pixel image of a handwritten digit. The total dataset is composed of 1797 datapoints. The t-SNE projection is presented in (b) while the PCA projection is shown in (c). The colour of each point represents their label value. The handwritten digits dataset is taken from the UCI Machine learning repository, sklearn.datasets.load_digits.

hyperparameters. This means every t-SNE run can yield different results. Indeed the gradient descent uses stochastic sampling and brings the learning rate and step

number as hyperparameters. Another hyperparameter is the early exaggeration. In order to provide more space between clusters in the target dimension, the probabilities p_{ij} of Eq. (2.6.2) are multiplied by the exaggeration value during the first 99 gradient descent steps. Finally, a highly relevant hyperparameter is the perplexity, which comes from choosing different standard deviations σ_i of $p_{i|j}$. The perplexity measures the effective number of neighbours of a point x_i. The value σ_i is thus chosen such that the Gaussian probability distribution has the predetermined perplexity. Using different perplexities changes the target number of neighbours for each point and can lead to very different results. As such it must be chosen with care. For an effective visualisation and discussion of the effect of the perplexity see [220].

Another major difference between PCA and t-SNE is that t-SNE focuses on preserving the local structure of the data. On the contrary PCA preserves global properties while potentially losing low-variance deviations between neighbours. As shown in Figure 2.6, as opposed to PCA you cannot visualise the size and distance between clusters in a t-SNE projection. Indeed the clusters in Figure 2.6 (b) have equal size and distance between them while the PCA projection in (c) correctly maps the distance between the clusters and the increased spread of cluster D. The t-SNE algorithm expands dense clusters, and contracts sparse ones, evening out cluster sizes. Consequently, global properties such as the distance between clusters cannot be gleaned from the t-SNE projection. On the other hand, PCA is a purely linear

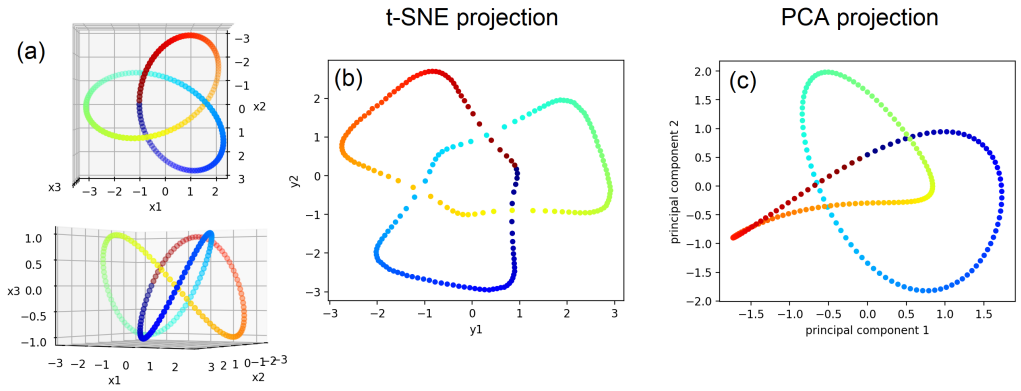

Figure 2.8: 3-dimensional plot of a trefoil knot from two different perspectives in (a) along with its 2-dimensional t-SNE projection in (b) and PCA projection in (c). The data points are marked by different colours to serve as a guide.

technique, while t-SNE is a highly non-linear algorithm. Consequently it can better handle linearly non-separable data. An example of this is shown in Figure 2.7, where both t-SNE and PCA are used on a complex dataset of handwritten digits. Each data point in the example is a 8x8 pixel image of a handwritten digit, as shown in Figure 2.7 (a). Consequently the t-SNE and PCA algorithms are applied to reduce the 64-dimensional dataset to a 2-dimensional dataset in Figures 2.7 (b) and (c). While the t-SNE projection contains various clusters successfully corresponding to

the different digits, the PCA algorithm struggles to create distinct clusters. In Figure 2.8 the t-SNE successfully represents the trefoil knot as three interlinked shapes of equal size, while PCA loses the intrinsic topology.

In conclusion, by comparing both projections we can guarantee the accuracy of the t-SNE results and gain the most information about the original dataset.

Chapter 3

Quantum Bridges in Enhanced Ionisation

In this chapter, we will perform a phase-space analysis of strong-field enhanced ionisation in molecules, with emphasis on quantum-interference effects. Indeed, in H_2^+ multiple ionisation bursts have been identified [191, 75] that do not follow the time profile of the external field. In [191, 76], a phase space analysis performed with Wigner quasiprobability distributions revealed intriguing structures that cycle through the momentum space in a quarter of a field cycle: the momentum gates (see section 1.3). However, the physical reason for the behaviour of momentum gates remains unknown. It is not clear whether momentum gates could occur under a different set of circumstances, such as with static fields, or what role quantum interference and other types of nonclassical behaviour play in this context. In order to address these questions we will apply methods that make use of phase space, such as the Wigner quasiprobability distribution. A major advantage is that they provide information not only about the electron's initial coordinate, but also about its initial momentum distribution and their subsequent evolution.

We will start this Chapter with section 3.1 by giving an overview of the system dynamics, looking at both the different phase space configurations as well as their effect on the ionisation rate. Following that, in section 3.2, we will perform a study of momentum gates for both initially delocalised and localised states, providing more information on their effect and their quantum bridging mechanism. Finally, in section 3.3, using both the autocorrelation function and the quantum Liouville equation, we investigate the temporal evolution of the system and its non-classical nature. We will close this chapter with a brief conclusion and discussion.

3.1 System dynamics

3.1.1 Phase space configuration

Our system is a one-dimensional single-electron molecule whose wave function $\Psi(x,t)$ is obtained by solving the TDSE numerically in a fixed grid using the split-operator method. Therein, propagation steps are split up between the potential and kinetic operator and treated in coordinate and momentum space respectively. Unless stated otherwise, the time step, length grid and momentum grid precision used are respectively dt = 0.1 a.u., dx = 0.2 a.u. and dk = 0.05 a.u.. More details are given in section 2.2.

The external laser field $\mathcal{E}(t)$ is taken to be static, i.e., $\mathcal{E}(t) = E_0$. This reflects to some extent the instantaneous configurations that will occur for a low-frequency field and will be essential in interpreting the results in Chapters 5 and 6.

The molecular binding potential $V(x)$ is given by

$$V(x) = V_0(x - R/2) + V_0(x + R/2), \tag{3.1.1}$$

Where each potential well $V_0 = V_{\text{sc}}$ is chosen be the soft-core potential defined in Eq. (2.1.5), and R is the internuclear distance. This is a good approximation for large internuclear distances, which is the parameter range at which enhanced ionisation occurs. Indeed previous computations [186] and experiments [191, 182] have shown that enhanced ionisation requires R to be at least a few times larger than the equilibrium value, which for H_2^+ is around 2 a.u..

The corresponding effective potential V_{eff} is shown in Figure 3.1 (a) and (b) for varying values of internuclear distance R, along with the binding potential $V(x)$ (dashed lines). In the field-free case we now have two centres located in the molecular wells as well as a central saddle in between them, labelled C. A non-vanishing field breaks this symmetry and causes the appearance of a second saddle, the Stark saddle (see Figure 2.1), labelled S.

We now identify and analyse the bound and continuum regions in phase space, shown in Figure. 3.1 (c) and (d). In the field-free case (see dashed lines), the separatrices are symmetric with regard to the central saddle. They form a closed curve around the two molecular centres, consisting of homoclinic trajectories. With the presence of a static field, the additional saddle means that, by extension, our system admits two separatrices in phase space, which are asymmetric with regard to the a reflection about $x = 0$. They have energies E_C and E_S, the energy of the central and Stark saddle respectively and their interplay will influence the ionisation dynamics. We define the energy difference between these two saddles as

$$\Delta E = E_C - E_S. \tag{3.1.2}$$

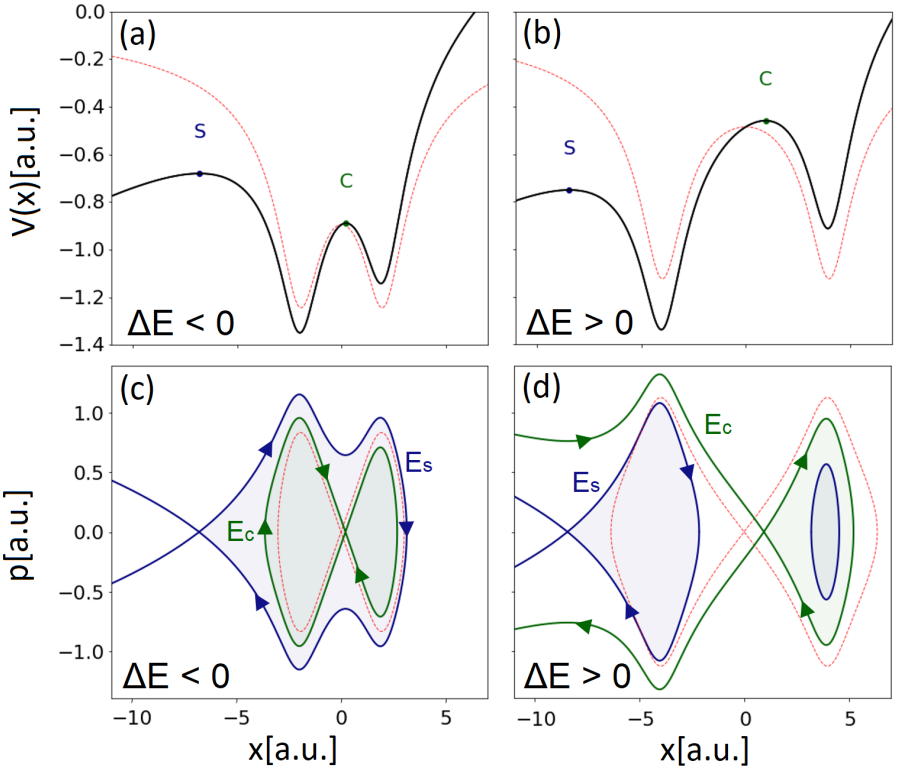

Figure 3.1: Effective potentials for the one-dimensional homonuclear molecular models described by the potential (3.1.1), using inter-nuclear separations of $R = 4$ a.u. [left] and $R = 8$ a.u. [right] and a static field $E = 0.0534$ a.u. [upper panels], together with the corresponding phase portraits [lower panels]. The Stark and the central saddles are indicated by the labels S and C in the figure, their respective energies by E_S and E_C and the field-free separatrices and potentials are given by the dashed red lines. The arrows indicate the direction followed by a trajectory. The energy between the two saddles ΔE is defined in Eq. (3.1.2). The shaded areas indicate the phase space regions for which the wave packet is bound. The colours of these regions match those of the respective separatrices.

ΔE is either negative [Fig. 3.1 left panels] or positive [Fig. 3.1 right panels] and characterises two different phase space configurations. If the downfield potential maximum is higher in energy than the upfield maximum ($\Delta E < 0$), then the separatrix associated with the Stark saddle (in blue) encapsulates entirely the homoclinic separatrix related to the central saddle (in green). Thus, even if an electronic wave packet tunnels through the central barrier, it would be trapped in the downhill centre. This means that it would still need to tunnel through a wider Stark saddle in order to reach the continuum. In contrast, if the energy of the central saddle is higher than that of the Stark saddle ($\Delta E > 0$), the electron would only need to tunnel through the central saddle to reach the continuum. The optimal scenario occurs if the energy of the central saddle is high enough to allow direct ionisation into the continuum, but still leads to an effective potential barrier narrower than that of a single atom with similar ionisation potential.

In addition, in order to ensure the robustness of those conclusions, the phase space configurations were investigated using a wide range of inter-nuclear distances

and field strengths. Most notably, using a 1D Coulomb potential model

$$V_{0C}(x) = -\frac{1}{|x|}. \tag{3.1.3}$$

The results are shown in Fig. 3.2 and in both cases we find the same bifurcation, i.e., the separatrices go from nested to open around a critical internuclear distance.

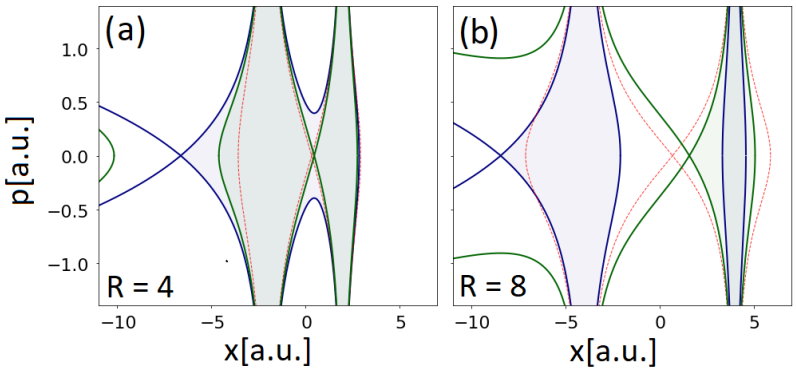

Figure 3.2: Phase portrait of the one-dimensional homonuclear molecular models described by the Coulomb potential (3.1.3), using inter-nuclear separations of $R = 4$ a.u. and $R = 8$ a.u. and a static field $E = 0.0534$ a.u. The field-free separatrices and potentials are given by the dashed red lines. The shaded areas indicate the phase space regions for which the wave packet is bound. The corresponding effective potentials can be found in Fig. 1.1.

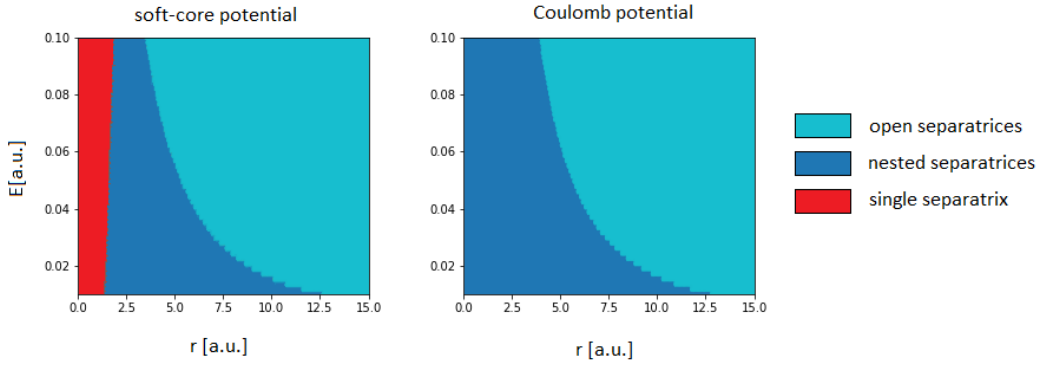

Figure 3.3: Schematic representation of the phase space configurations for a 1D model molecule computed with the soft-core potential given by Eq. (2.1.5) (left panel) and singular potential given by Eq. (3.1.3) (right panel). Different colors indicate the varying phase space configurations dependent on the parameter regions.

To study the previous point more systematically, in Fig. 3.3 we show how the different configurations vary with regard to the field strength and internuclear separation (vertical and horizontal axis, respectively). In the parameter range of interest (large internuclear distances and field strengths up to 0.07 a.u.), the qualitative behavior is the same for both potentials. The tests performed above confirm that the potential shapes will not alter the following conclusions.

3.1.2 Initial wavepacket

In this Chapter, enhanced ionisation will be studied using three different initial states: Localised around the downfield well $\Psi_{\text{down}}(x,0)$, localised around the upfield well $\Psi_{\text{up}}(x,0)$, or delocalised symmetrically between both wells $\Psi_{\text{cat}}(x,0)$. The localised wavefunctions are approximated by Gaussian wavepackets defined in Eq (2.2.4) considering $q_0 = -R/2$ for $\Psi_{\text{down}}(x,0)$ and $q_0 = R/2$ for $\Psi_{\text{up}}(x,0)$. Within the approximations used those describe coherent states.

The delocalised wave function is taken to be the symmetric coherent superposition

$$\Psi_{\text{cat}}(x,0) = \frac{\Psi_{\text{down}}(x,0) + \Psi_{\text{up}}(x,0)}{\sqrt{2\,(1+\mathcal{I}_o)}}, \tag{3.1.4}$$

where $\mathcal{I}_o$ is the overlap integral

$$\mathcal{I}_o = \int \Psi^*_{\text{down}}(x,0)\Psi_{\text{up}}(x,0)dx. \tag{3.1.5}$$

This wavepacket is known as a stationary cat state [13].

For the symmetric, delocalised state given by Eq. (3.1.4), the Wigner function (see Eq. 2.3.1)), reads

$$W_{\text{cat}}(x,p,0) = \frac{W_{\text{down}}(x,p,0) + W_{\text{up}}(x,p,0) + W_{\text{int}}(x,p,0)}{2\,(1+\mathcal{I}_o)}, \tag{3.1.6}$$

where

$$W_j(x,p,0) = \frac{1}{\pi}\exp\left[\gamma(x \pm R/2)^2 - \frac{p^2}{\gamma}\right]. \tag{3.1.7}$$

The index $j =$ down indicates a Wigner function centred at $(q_0,p_0) = (-R/2,0)$, i.e., the downfield well, while $j =$ up refers to a centre at $(q_0,p_0) = (R/2,0)$, i.e., the upfield well. The term

$$W_{\text{int}}(x,p,0) = \frac{2}{\pi}\exp\left[-\gamma x^2 - \frac{p^2}{\gamma}\right]\cos[pR] \tag{3.1.8}$$

is peaked at the origin and gives a series of interference fringes parallel to the x axis, whose extrema occur for $p = n\pi/R$. Even and odd values of the integer number n give maxima and minima, respectively. If the wave packet is initially localised in the downfield or upfield well, the initial Wigner function will be given by $W_{\text{down}}(x,p,0)$ or $W_{\text{up}}(x,p,0)$, respectively, and the interference term is absent.

3.1.3 Ionisation rates

The ionisation rate Γ from an initial time $t = 0$ to a final time $t = T$, is calculated using

$$\Gamma = -\ln\left(\frac{|\mathcal{P}(T)|^2}{|\mathcal{P}(0)|^2}\right)\frac{1}{T}, \tag{3.1.9}$$

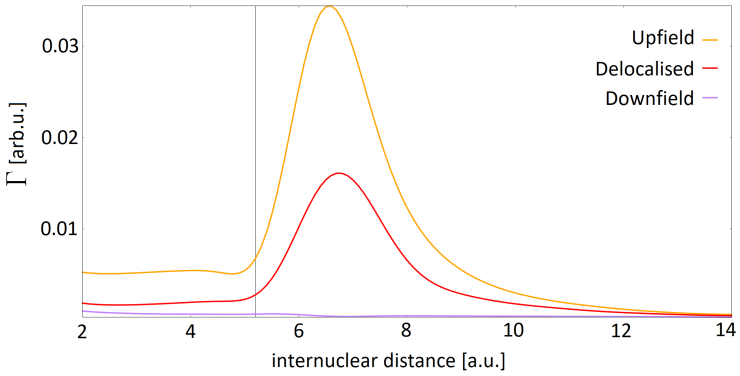

Figure 3.4: Ionisation rate as a function of the inter-nuclear distance R, calculated in a 'box' from $x_{\min} = -100$ a.u. to $x_{\max} = 100$ a.u., final time $T_{end} = 150$ a.u. and field strength $E = 0.0534$ (intensity $I = 10^{14}$ W/cm^2) using different starting wave packets: delocalised (red), localised upfield (orange) and localised downfield (purple). The vertical line indicates the inter-nuclear separation for which the phase-space configuration changes.

where

$$\mathcal{P}(t) = \int_{-\infty}^{+\infty} \Psi^*(x,t)\Psi(x,t)dx. \tag{3.1.10}$$

This definition of ionisation rate was used in the seminal paper [162] in the context of enhanced ionisation of molecules. Note that, numerically, the limits of the above integral will be finite (typically $x = -100$ to $x = 100$ a.u.). Instead of an absorber, the grid size is taken to be twice as large as the 'box size' set by the above stated limits. The integration is performed over the box size and due to irreversible ionisation, Eq. (3.1.10) will be less than unity and decrease with time. Thus, it will be a good measure of the probability density that has reached the integration boundaries. Since the box size over which the integration is performed is only a fraction of the total grid size, the norm will decrease and reflections will be minimised.

The ionisation rate as a function of the inter-nuclear distance, plotted in Fig. 3.4, shows the effect of the different phase-space configurations. If the initial wave packet is delocalised, or centred around the upfield potential minimum, a very strong peak is present. The ionisation rate starts to increase dramatically when the inter-nuclear distance reaches the value at which the phase-space configuration changes. For this critical value of R, which, for the chosen external field, is $R_c = 5.2$ a.u. (see thin vertical black line), the outer separatrix "opens" and no longer traps the wave packet. The ionisation rate then reaches a peak at $R = 6.8$ a.u., and drops for larger inter-nuclear separations. This happens because the two centres become further apart, thus hindering tunnel ionisation via the central saddle. If a downfield initial wave packet $\Psi_{\text{down}}(x, 0)$ is taken, the ionisation rate is suppressed by two orders of magnitude.

This, along with the fact that the ionisation rate with an upfield wave packet is about double that of a delocalised wave packet, suggests that around the opening

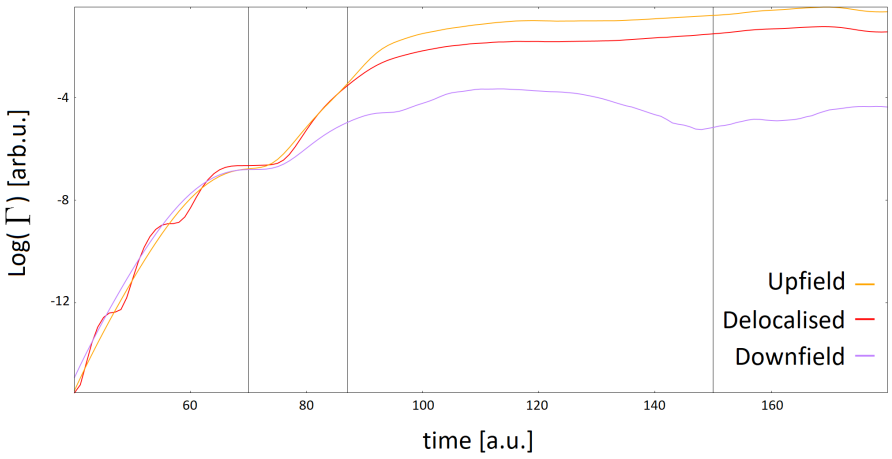

Figure 3.5: Ionisation rate Γ on a logarithmic scale over time of an H_2^+ molecule of inter-nuclear distance $R = 6.8$ a.u. in a static field of strength $E = 0.0534$ a.u.. The starting wavepacket is either delocalised (red), localised upfield (orange) or downfield (purple). The vertical lines are set at times $t = 70$ a.u., $t = 87$ a.u. and $t = 150$ a.u. and relate to Fig. 3.6

.

of the separatrix ionisation comes mainly from the upfield population. This corresponds exactly to the hypothesised point of maximum enhancement, where the energy of the saddle is high enough for the tunnelling electron not to be trapped by the downfield centre (e.g. after $R_c = 5.2$ a.u.) but low enough for the effective potential barrier to be narrower than that of a single atom (e.g. before $R = 9$ a.u.).

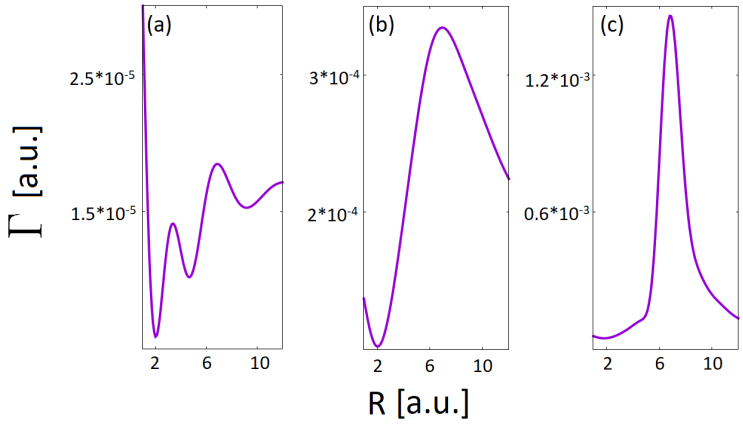

Figure 3.6: Ionisation rates with a static field of strength $E = 0.0534$ for a delocalised starting wavepackets and with grid size $x = -100$ to $x = 100$ over inter-nuclear distance for different final ionisation times, from left to right, $t = 70$ (a), $t = 87$ (b) and $t = 150$ (c)

The overall ionisation rate is however not a sufficient tool in order to understand the dynamics of ionisation close to the core. This is because there is a time delay between events at the core and at the boundary, where the information about the ionisation rate is taken. The ionisation rate over time, shown in Fig. 3.5 is compared with the ionisation rate as a function of the inter-nuclear distance plotted in Fig. 3.6 (a)-(c) for different final times T.

Using the saddle separatrix in Fig. 3.1 (b) we can approximate the time delay between the ionisation bursts and events happening near the core. By estimating that starting at $x = -15$ a.u. the wavepacket follows closely the saddle separatrix (see section. 3.2) and using its average velocity, we see that the region of interest of the momentum gates seen in [76] occurs around $t = 70$, or Fig. 3.6 (a). This suggests that important effects at the core happen before the main ionisation burst seen in Fig. 3.5 at $t = 90$. However, from Fig. 3.6 (b), we see the main features of the ionisation rate in Fig 3.4 build up over time, mainly after the region of interest.

The ionisation rate is a stationary feature that takes time to develop. In order to study the events happening near the core at a much shorter time scale, we will use throughout this thesis the Wigner quasiprobability (Eq. 2.3.1) distribution and the autocorrelation function (Eq. 2.2.5).

3.2 Quantum bridging via momentum gates

3.2.1 Momentum gates for initially delocalised states

Using the Wigner quasiprobability distributions, we provide a more detailed explanation for enhanced ionisation and its causes. In Fig. 3.7, we plot such distributions for different inter-nuclear separations computed using initial delocalised states $\Psi_{\text{cat}}(x, 0)$. The inter-nuclear distances used in the left, centre and right panels, respectively, have been chosen such that (i) the two separatrices are nested and closed ($R = 4.0$ a.u.), (ii) the outer separatrix has just opened ($R = 6.8$ a.u.), and (iii) the separatrix including the central saddle is completely open and the two centres are well separated ($R = 14.0$ a.u.).

The initial Wigner functions $W(x, p, 0)$ are given by Eq. (3.1.6), and behave as predicted, with Gaussian shaped quasiprobability densities centred at the origin $(x, p) = (0, 0)$ and at each potential well $(x, p) = (\pm R/2, 0)$. There are also interference fringes near the central saddle, with extrema at $(x, p) = (0, n\pi/R)$, which become finer for larger values of R. This pattern is less distinguishable for small inter-nuclear distances [Fig. 3.7(a)] due to the strong overlap of the Gaussians that form $W(x, p, 0)$, but becomes clearer as this overlap decreases [see, e.g., Fig. 3.7(a′)]. For $R = 14$ a.u., the central fringes and the Gaussians located in the uphill and downhill potentials are very well defined, with little overlap. With time propagation, the Wigner functions become asymmetric, flowing from the upfield to the downfield well in the molecule. Semiclassically, the expected behaviour (shown in Figure. 2.2) is that the Wigner quasiprobability density follows the classical separatrices and form a tail that can be associated with over-the-barrier or tunnel ionisation, as well as with an oscillatory behaviour around the separatrix, as shown in section 2.3. It can be seen clearly on the left of the downfield well, for $t \geq 20$ (third to last row in Fig. 3.7).

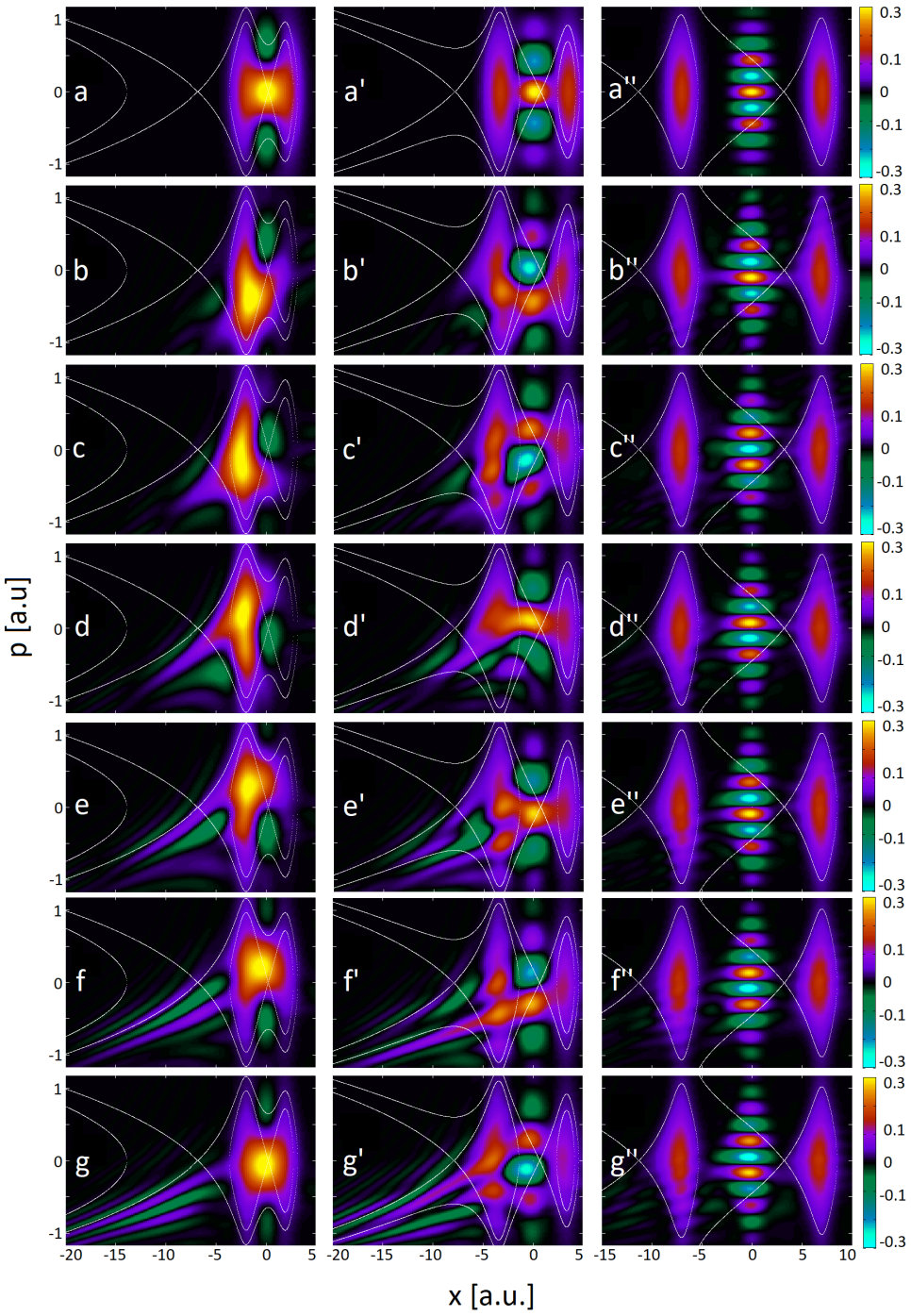

Figure 3.7: Wigner quasi probability distribution at different instants of time, calculated for a model H_2^+ molecule in a static laser field of strength $E = 0.0534$ a.u. (intensity $I = 10^{14}\mathrm{W/cm}^2$) using an initially delocalised (cat) state given by Eq. (3.1.4), with $\gamma = 0.5$. In the left, middle and right columns, the inter-nuclear separation is taken as $R = 4$ a.u., $R = 6.8$ a.u. and $R = 14$ a.u., respectively. The temporal snapshots are given from top to bottom. Panels (a), (a′) and (a″) [first row] have been calculated for $t = 0$ a.u., panels (b), (b′) and (b″) [second row] for $t = 8$ a.u., panels (c), (c′) and (c″) [third row] for $t = 12$ a.u., panels (d), (d′) and (d″) [fourth row] for $t = 16$ a.u., panels (e), (e′) and (e″) [fifth row] for $t = 20$ a.u., panels (f), (f′) and (f″) [sixth row] for $t = 24$ a.u., panels (g), (g′) and (g″) [seventh row] for $t = 30$ a.u. The thin white lines in the figure give the equienergy curves (including the separatrices).

However, there are very peculiar features that do not follow the separatrices, form at much earlier times and occur in the region around the central saddle [see, for instance, Fig. 3.7(b), (b′) and (b″)]. They consist of a strong quasiprobability flow from one centre to the other. This transfer occurs mostly along lines of approximately vanishing phase-space slope, i.e., of nearly constant momentum, and are the momentum gates reported in Refs. [75, 76]. They are visible for the whole range of inter-nuclear separations in Fig. 3.7, although they manifest themselves in different ways.

The interference fringes around the central saddle act as a quantum bridge and facilitate this transfer for positive quasiprobability densities. The flow is significant if the overlap of the left and right peaks with the central interference structure is large, as shown in the left and central columns of Fig. 3.7. Therein, the Wigner function exhibits a clockwise movement, whose period depends on the inter-nuclear separation. Figs. 3.7(b) and (b′) show the start of this motion, with a strong right-left flow for momenta below that of the central saddle. This momentum gate then moves upward in phase space until a subsequent bridge is established, and the bulk of the Wigner function is transferred back.

Furthermore, the presence or absence of enhanced ionisation is directly linked to the interplay of the semiclassical tail and the population transferred via the quantum bridge. If the separatrices are nested (left panels of Fig. 3.7), the bulk of the quasiprobability distribution remains trapped by the inner separatrix and tunnels back to the upfield centre. This trapping can be clearly seen on the left-hand side of Fig. 3.7(b), in which the inner separatrix hinders the Wigner function to reach the Stark saddle. Significant tunnelling via this saddle may only occur after population has built up in the downfield centre, at later times [see Fig. 3.7(d) and (e)]. There is also some "spilling" of the Wigner function for larger absolute values of p, when the two separatrices become close in phase space. This spilling can be seen at the bottom of Figs. 3.7(b) and (e), but it is not a highly probable pathway.

If, on the other hand, the two separatrices are no longer nested, population trapping will no longer occur. Thus, the tail near the Stark saddle will build up already for $t = 8$ a.u.[Fig. 3.7(b′)]. This will add up to the contributions from the tail that forms for higher absolute values of momenta, when the separatrices' energies are close [Fig. 3.7(c′)]. Figs. 3.7(d′) to (g′) show that, for later times, direct transfer via the quantum bridges will feed into both tails, which will cause enhanced ionisation. Particularly striking is Fig. 3.7(f′), which shows a direct quasiprobability leak from the uphill centre to the continuum via the quantum bridge, at a higher energy than that determined by the Stark saddle.

For larger values of R, there is far less quasiprobability transfer, but the bridges can be clearly seen due to the three phase-space regions of the Wigner functions being well separated (see right columns in Fig. 3.7). For instance, for $R = 14$

a.u., at $t = 8$ a.u. [Figs. 3.7(b″)], a horizontal bridge forms near zero momentum, and right-left population transfer occurs. Subsequently, the central fringes move downwards. If a negative (positive) quasiprobability density is located near the central saddle, the bridges are weakened (strengthened) [see e.g., Figs. 3.7(c″) and (f″) in contrast to Figs. 3.7(b″), (d″), and (g″)]. If the central bridge is weakened, other bridges may occur for higher, albeit constant momenta.

Field-free Wigner function

The above-mentioned cyclic evolution of the momentum gates is even present for the Wigner function of a field-free H_2^+ molecule, shown in Figure 3.8. For smaller inter-nuclear distances, e.g. $R = 6$ a.u., the quasiprobability density "wobble" from a positive to a negative gradient. There is a flow from one centre to another, facilitated by the quasiprobability maximum at $p = 0$. The frequency of this change in the gradient increases with the inter-nuclear distance. For larger inter-nuclear distances, where the overlap region is separated from the two centres, the flow from one centre to another is a lot weaker and is characterised by links between different interference fringes. First, a simultaneous flow occurs in the positive (negative) momentum region towards the upfield (downfield) centre, see Fig. 3.8(d). Following that, a bridge between the potential well populations and the saddle population emerges near $p = 0$, see Fig. 3.8(e).

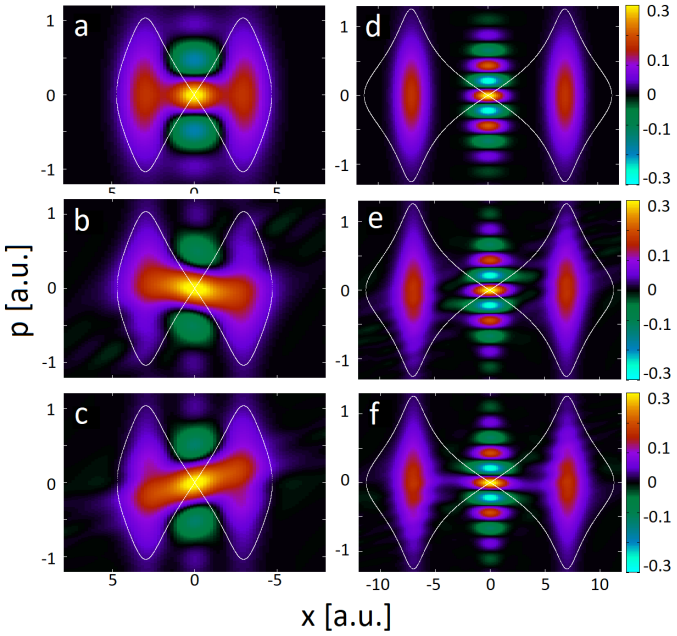

Figure 3.8: Wigner function computed using the same initial state as in Fig. 3.7, but considering a field-free H_2^+ model molecule. The left and the right columns have been calculated for inter-nuclear separations of $R = 6$ a.u. and $R = 14$ a.u., respectively. The labels (a) and (d) refer to $t = 0$, (b) to $t = 5$, (c) to $t = 12$, (e) to $t = 15$, and (f) to $t = 20$.

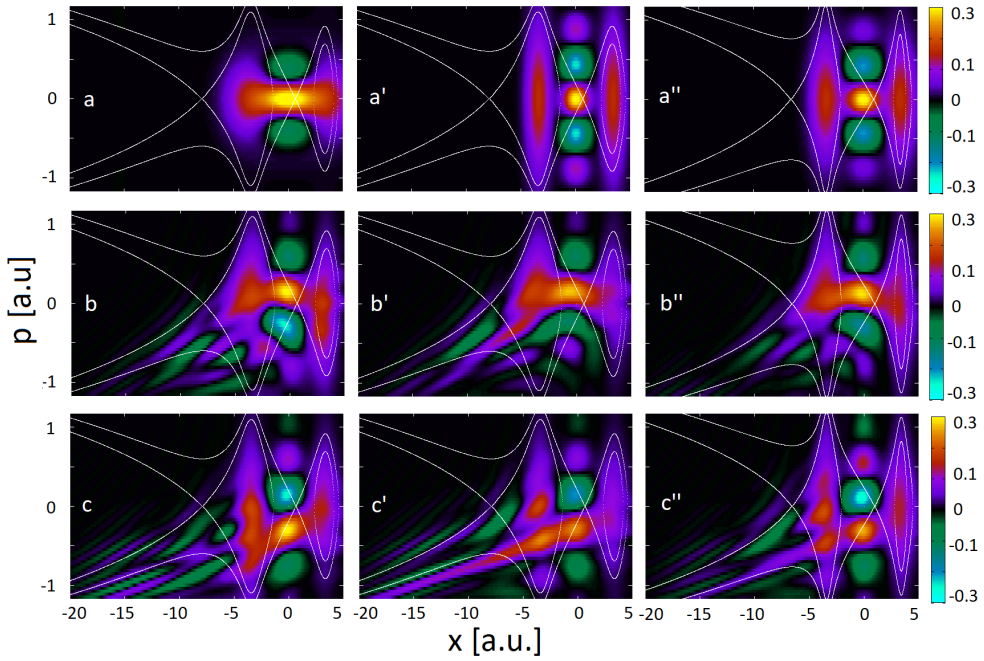

Figure 3.9: Wigner quasi probability distribution computed for a H_2^+ molecule of inter-nuclear separation $R = 6.8$ a.u. in a static laser field of strength $E = 0.0534$. In the columns from left to right a delocalised Gaussian initial wavepacket of width $\gamma = 0.2$ [a.u.], $\gamma = 0.8$ [a.u.] and $\gamma = 0.5$ [a.u.], respectively. The first two columns use the soft-core potential expression in Eq. (2.1.5), while the right-most column uses Eq. (3.2.1). The labels (a), (a′) and (a″) refer to $t = 0$, (b), (b′) and (b″) to $t = 15$, and (c), (c′) and (c″) to $t = 24$.

Different binding potential shape

The quantum bridges reported here are also quite robust with regard to the shape of the binding potential and of the initial wave packet. This is shown in Fig. 3.9, in which we present Wigner quasiprobability distributions computed using initial Gaussian states of different widths, $\gamma = 0.2$ [left column] and $\gamma = 0.8$ [middle column] for the same parameters employed in Fig. 3.7. [middle column]. Although there are differences in their shapes, the quantum bridges keep the same features and exhibit the same time dependence. In the right-most column we employ the regular width $\gamma = 0.5$, but use a different soft-core potential, which is the limit of the improved potential in [221] for large internuclear distances. Explicitly, this is given by using Eq. (3.1.1) with

$$\widetilde{V}_0(x) = -\frac{\frac{1}{2}Z}{\sqrt{x^2 + \frac{1}{4Z^2}}}, \tag{3.2.1}$$

where $Z = 1$ is the charge of the ion core. The results obtained using the improved potential are practically indistinguishable from those in Fig. 3.7 [middle column]. This shows that the quantum bridges are a universal feature in the regime of interest.

3.2.2 Momentum gates for initially localised Wigner functions

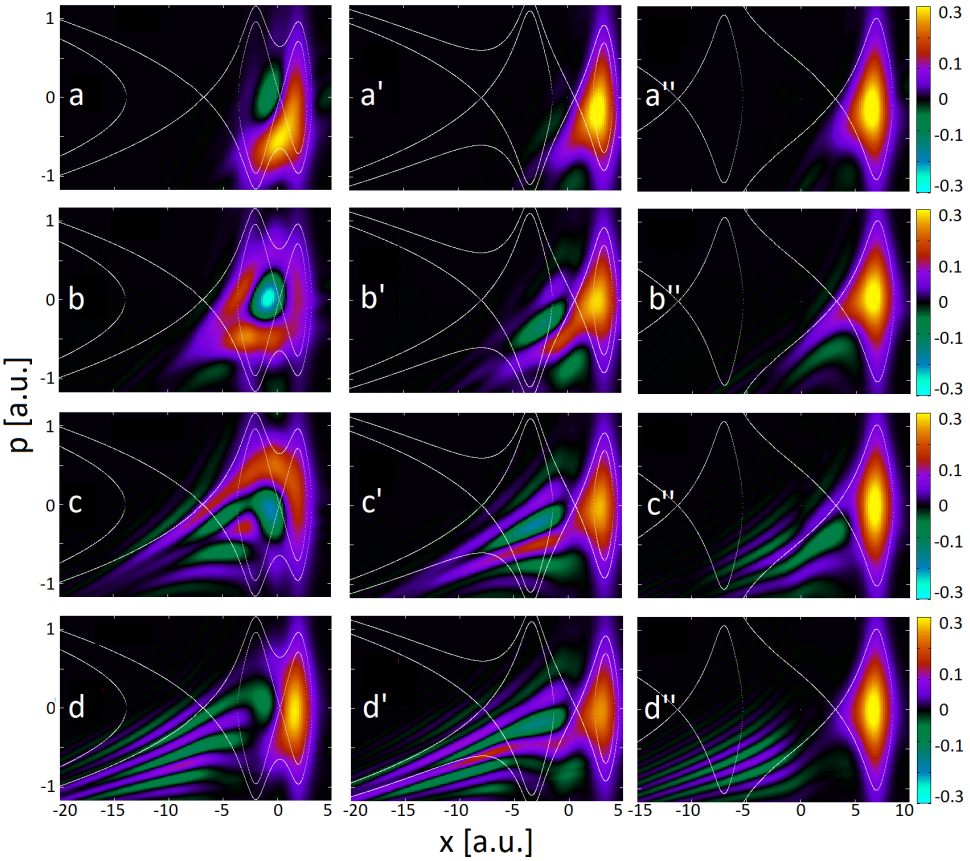

Figure 3.10: Wigner quasi probability distribution computed for a H_2^+ molecule in a static laser field of strength $E = 0.0534$ using a Gaussian initial wave packet $\Psi_{\text{up}}(x, 0)$ of width $\gamma = 0.5$ centred around the upfield potential well. The left, centre and right columns correspond to the inter-nuclear separations $R = 4$ a.u., $R = 6.8$ a.u. and $R = 14$ a.u., respectively. The first, second, third and fourth row have been calculated for $t = 6.0$ a.u. [panels (a), (a′) and (a″)], $t = 12.0$ a.u. [panels (b), (b′) and (b″)], $t = 20.0$ a.u. [panels (c), (c′) and (c″)] and $t = 30.0$ a.u. [panels (d), (d′) and (d″)].

To expand on the roles of the quantum bridges and their cyclical motion, in the two subsequent figures we employ a similar system, but with localised initial wave packets. In this case, the central interference fringes in the initial Wigner function given by Eq. (3.1.8) are absent. For a wave packet $\Psi_{\text{up}}(x, 0)$ placed at the upfield potential well, the dynamics and nature of the bridges are different from those observed in the delocalised case. If the potential wells are not close enough, the quantum bridge does not form and there is no enhanced ionisation. We see this for $R = 14$ a.u. (right panels of Fig. 3.10), where the tail marking the escape path follows the separatrix associated with the uphill centre [Fig. 3.10(b″)]. Subsequently, it deviates from this curve when the escaping electron is slowed down by the downfield centre [Fig. 3.10(d″)], but no shortcut to the continuum is provided. This is radically different from the $R = 4$ a.u. case, displayed in the left column of

Fig. 3.10, where both the momentum gates and the clockwise motion of the Wigner function are present. Because the separatrices are nested, the population flowing to the downfield centre via the momentum gate is trapped. It then travels back via a positive momentum gate to the upfield centre. Finally, for $R = 6.8$ a.u. (middle column of Fig. 3.10), we present the optimal configuration. Indeed the potential wells are close enough to allow the creation of the quantum bridge. However, because the separatrices are open, the population escapes directly through the semiclassical path, following the separatrices, and does not flow back to the upfield centre. The quantum bridges provide a "shortcut" to several pathways for the quasiprobabilities to reach the continuum. A clear example is provided in Fig. 3.10(d′), which shows a tail starting along the central saddle and being guided by the quantum bridge towards the Stark saddle. Escape happens via several equienergy curves, not only the inner separatrix.

In this context, it is noteworthy that the dynamics and the nature of the bridges are different from those observed in the delocalised case. Whilst we do see multiple tails enhanced by tunnelling from the upfield well, the clockwise motion observed in Fig. 3.7 is much less clear. This quasiprobability transfer from one centre to the other, displayed in the last row of the figure, is only obvious when the separatrices are nested, i.e., for $R < R_c$ [see left panels in Fig 3.10]. In this case, population trapping will hinder enhanced ionisation. However, for $R > R_c$, there will be no such trapping. Furthermore, the clockwise motion of the Wigner function will be strongly suppressed, with no feedback loop to the upfield centre. This makes the upfield localised configuration more efficient for enhanced ionisation than using a delocalised initial state.

In Fig. 3.11, we present the Wigner probability distributions for an initial downfield wavepacket. In this case, the previously observed quantum bridges are absent throughout and the escape pathway mainly follows that of a single atom [77], i.e., along the separatrix determined by the Stark saddle. Only if the two separatrices are nested and energetically close, i.e., for $R < R_c$, is there some upfield quasiprobability flow, as shown in the first column of the figure. This is however not sufficient to form a bridge between both centres. Nested separatrices mean that ionisation will be strongly suppressed, which can be inferred by the very faint tails of the Wigner function in the continuum region.

3.3 Temporal evolution and non-classicality

We can now focus on the cyclical evolution of the momentum gates. This evolution can be quantified directly using autocorrelation functions Eq (2.2.5). In Fig. 3.12, we plot their absolute values computed for an initial delocalised state $\Psi_{\text{cat}}(x, 0)$ and the same parameters used in Fig. 3.7. As the quasiprobablity distribution

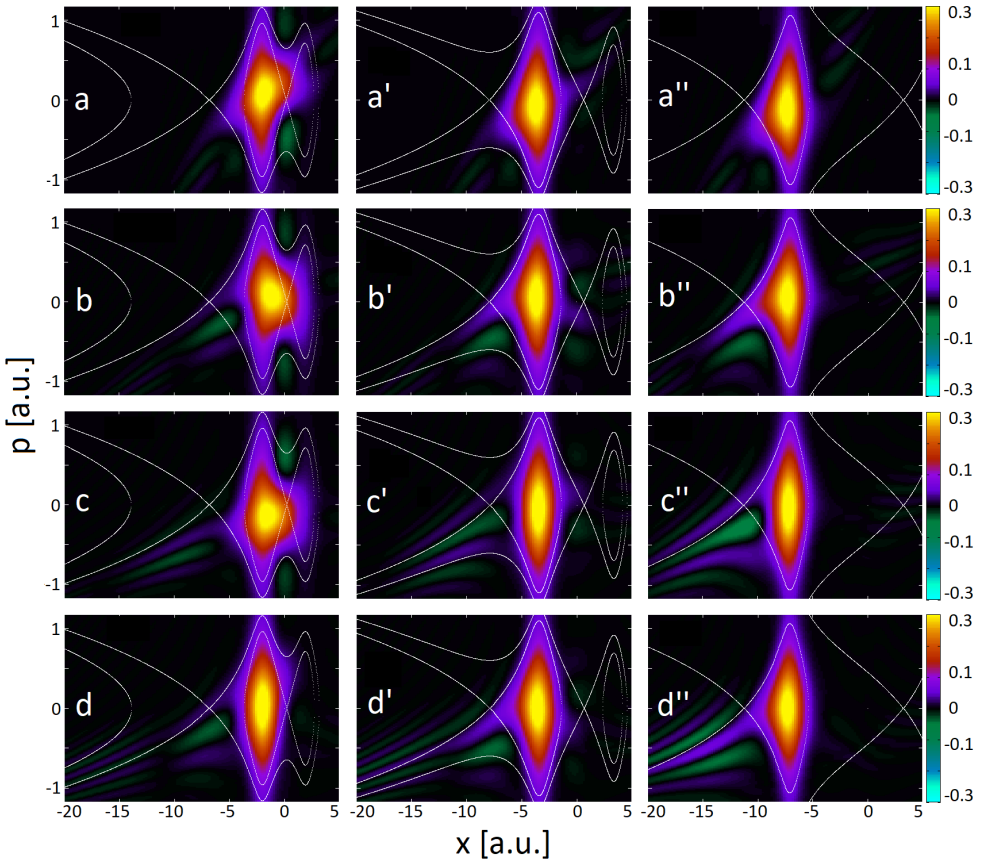

Figure 3.11: Wigner quasi probability distribution computed for a H_2^+ molecule in a static laser field of strength $E = 0.0534$ using a Gaussian initial wave packet $\Psi_{\text{down}}(x, 0)$ of width $\alpha = 0.5$ centred around the downfield potential well. The left, centre and right columns correspond to the inter-nuclear separations $R = 4$ a.u., $R = 6.8$ a.u. and $R = 14$ a.u., respectively. The first, second, third and fourth row have been calculated for $t = 6.0$ a.u. [panels (a), (a′) and (a″)], $t = 12.0$ a.u. [panels (b), (b′) and (b″)], $t = 20.0$ a.u. [panels (c), (c′) and (c″)] and $t = 30.0$ a.u. [panels (d), (d′) and (d″)].

shifts towards the downfield centre, the autocorrelation function decreases before increasing again as the population returns to the upfield centre. It then reaches its starting position, completing a period of $T = 29$ a.u. for $R = 4$ a.u., $T = 18.3$ a.u. for $R = 6.8$ a.u. and $T = 8.4$ a.u. for $R = 14$ a.u. This is confirmed by comparing the Wigner functions for $R = 4$ a.u. at $t = 0$ and $t = 30$ [Figs. 3.7(a) and (g), respectively]. The quasiprobability densities in the bound phase-space region are nearly identical. Significant differences between both Wigner functions occur only in the continuum region, for which there are tails along equienergy curves in the latter time. Interestingly, there is a single frequency associated with the cyclic motion of the Wigner function, which increases with the internuclear distance. This is not obvious as a Gaussian wavepacket is a coherent superposition of many eigenfunctions of the system, which are associated with more than one bound-state energy.

In contrast, Fig. 3.13 shows that, for initially localised wavepackets, this clockwise motion is not always present and the autocorrelation function may not be

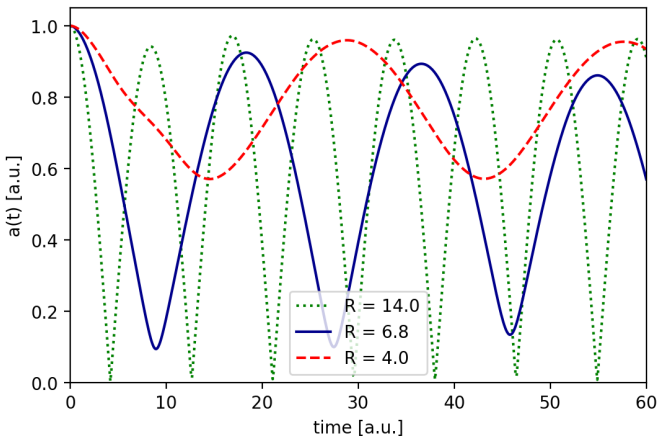

Figure 3.12: Absolute value of the auto-correlation function of a H_2^+ molecule in a static laser field of intensity $E = 0.0534$ a.u. using a delocalised starting wave packet with inter-nuclear distances of $R = 4$ a.u. (red dashed), $R = 6.8$ a.u. (blue) and $R = 14$ a.u. (green dotted).

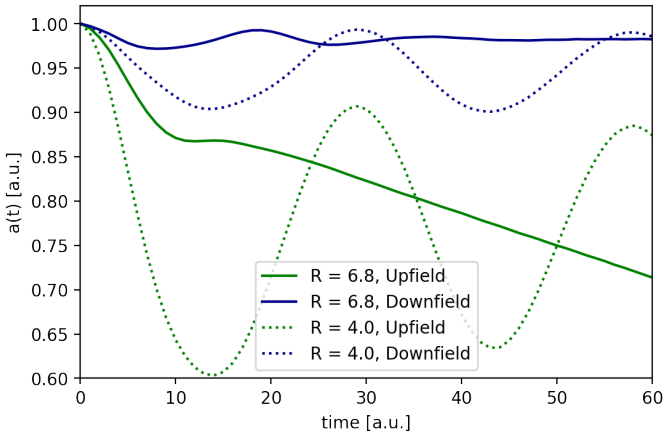

Figure 3.13: Absolute value of the auto-correlation function of a H_2^+ molecule in a static laser field of intensity $E = 0.0534$ a.u. using a localised starting wavepacket with inter-nuclear distances of $R = 4$ a.u. upfield (green dotted) and downfield (blue dotted) or $R = 6.8$ a.u. upfield (green) and downfield (blue).

periodic. In this case, periodic behaviour only occurs for $R < R_c$, i.e., when the separatrices are nested and the outer separatrix causes the population to be trapped. For instance, for $R = 4$ a.u., despite starting in a localised state, the autocorrelation function oscillates with a similar frequency both in the upfield and downfield case. The amplitude of that oscillation however is a lot greater if an initial upfield wavepacket $\Psi_{\text{up}}(x, 0)$ is taken, and resembles that obtained using a delocalised starting wavepacket. This cyclic behaviour however changes if the separatrices are no longer nested, i.e., $R > R_c$. For the optimal inter-nuclear distance $R = 6.8$ a.u., if the initial wavepacket is located downfield, the oscillation is very faint, practically absent. For an initial upfield wavepacket $\Psi_{\text{up}}(x, 0)$, the autocorrelation function decays practically monotonically. Thus, the electron escapes out of the upfield potential while its return is blocked, maximising ionisation enhancement

In order to understand the non-trivial, sometimes periodic behaviour discussed above, to first approximation one may resort to classical arguments. For that purpose, it is helpful to consider the periodic bound orbits of a classical electron moving in the effective potential (2.1.4) that arises in the presence of a static field. Such orbits have well-defined energies, and their dynamics are governed by Hamilton's equations. This explains the clockwise evolution of the momentum gates, which agree with the directional arrows in Fig 3.1.

Periodic motion implies closed orbits, whose classical period T_{cl} can be computed with the integral

$$T_{cl} = \oint_{sep} \frac{1}{p(x)} dx, \tag{3.3.1}$$

over a closed equienergy curve in phase space. As we are interested in the highest possible energy a bound electron may have, we consider the closed path to be along the separatrix. These estimates can be used as long as the inter-nuclear distance is small enough so that the phase space configuration contains homoclinic trajectories which circle both centres [see Fig. 3.1(a)]. This condition holds for inter-nuclear distances $R < R_c$, since in that case the separatrices are nested.

We obtain a maximum and minimum value for T_{cl} following the path along the outer and inner separatrices, respectively. Using the period T_q obtained from the

Initial state	$R = 4$		$R = 4.5$		$R = 5$	
	T_{cl}	T_q	T_{cl}	T_q	T_{cl}	T_q
Ψ_{up}	31.9 - 38.7	29.0	39.5 - 51.4	29.8	50.1 - 51.9	NA
Ψ_{cat}	31.9 - 38.7	28.8	39.5 - 51.4	28.3	50.1 - 51.9	26.1
Ψ_{down}	31.9 - 38.7	29.0	39.5 - 51.4	29.7	50.1 - 51.9	NA

Table 3.1: Comparison of the period T in a.u. obtained from the classical estimates (T_{cl}) given by Eq. (3.3.1) and from the absolute value of the auto-correlation function (T_q) of a H_2^+ molecule in a static laser field of strength $E = 0.0534$ a.u. (intensity $I = 10^{14}\text{W/cm}^2$) computed for with different inter-nuclear distances of $R = 4$ a.u., $R = 4.5$ a.u. and $R = 5$ a.u. using different initial states (delocalised (cat), localised upfield and downfield) with width $\gamma = 0.5$ a.u. Cells labelled NA refer to systems with non-periodicity.

autocorrelation function of the same system, we can compare the classical evolution estimates to the empirical results. These results are summarised in Table 3.1, with the classical estimates being far above the empirical values in all cases. Furthermore, the period T_{cl} increases with the inter-nuclear distance, while the opposite trend is observed for T_q (see also the discussion of Fig. 3.12, for a wider range of internuclear separations). Throughout, the values of T_q obtained for initial delocalised states are slightly lower. At $R = 5$ a.u., while the separatrices are still nested, the phase space configuration is very close to the bifurcation discussed in Sec. 3.1 that will lead to an open outer separatrix. If the initial wave function is in a localised initial state, the oscillation no longer takes place and the system resembles that of the open

configuration, seen in the middle column of Figs. 3.10 and 3.11, and in Fig. 3.13. Classically, an oscillation is still expected as the orbits remain closed. All this indicates that the evolution of the Wigner function is non-classical.

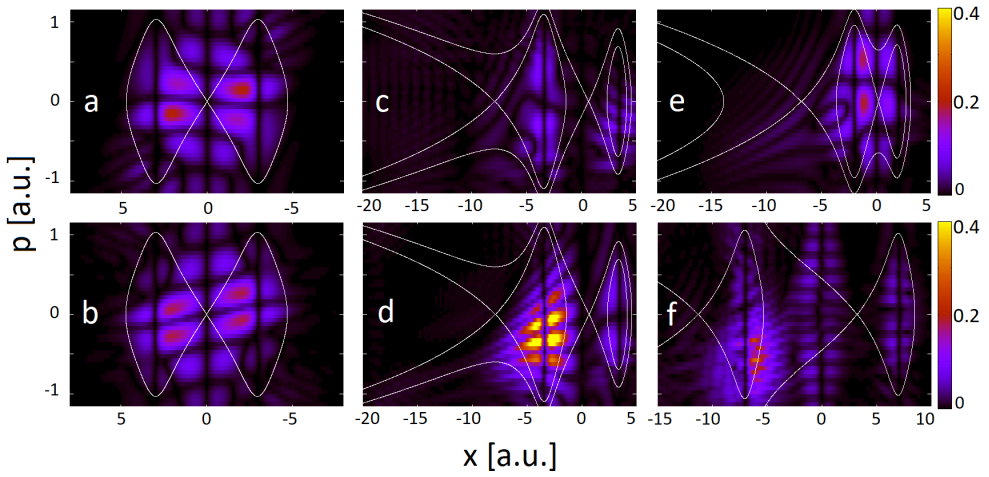

Figure 3.14: Phase space map of the quantum corrections $Q(x, p, t)$ [Eq.(2.3.2)] of a H_2^+ molecule. (a) and (b) are a field-free delocalised wave packet of inter-nuclear distance $R = 6$ a.u. at times $t = 5$ and $t = 13$ respectively. (c) and (d) both use an H_2^+ molecule in a static laser field of strength $E = 0.0534$ a.u. (intensity $I = 10^{14}\mathrm{W/cm}^2$), inter-nuclear distance $R = 6.8$ a.u. and time $t = 24$, and use an initial wave packet localised downfield and upfield respectively. (e) and (f) use a delocalised starting wave packet in the same static field. (e) has $R = 4$ a.u. and $t = 29.5$ while (f) has $R = 14$ a.u. and $t = 26$. The separatrix of the system is shown by the white line.

To further expand on this, we now present in Fig. 3.14 the quantum corrections $Q(x, p, t)$ to the classical Liouville equation [Eq. (2.3.2)]. If the Wigner function has a fully classical time evolution, $Q(x, p, t)$ vanishes everywhere. As seen in Figure 3.14, this is not the case. Spots in phase-space that are non-zero indicate where and when the evolution of the Wigner function is non-classical.

From Fig. 3.14(a) and (b), we see that this non-classical evolution is not due solely to the electric field, as it is present in the field-free case. By comparing those results to the Wigner quasi-probability density in Fig. 3.8 (c) and (d), the areas around which $Q(x, p, t) = 0.2$ a.u. follow the probability density. This is not true around the central saddle, where the evolution is practically classical. This is expected, as, in this region, the potential barrier may be approximated by an inverted harmonic oscillator. Since such a potential does not contain terms higher than up to the second order, $Q(x, p, t) = 0$ holds. One should bear in mind, however, that Wigner quasiprobability distributions do show non-local behaviour near separatrices [135].

From adding a static field, we can draw additional conclusions. The quantum corrections are located around the well, close to the region where the quantum bridges occur. If the wave packet is initially placed in the downfield well, the corrections are much weaker, but are still present, as shown in Fig 3.14(c). This supports

the observations in the second column of Fig. 3.11, which shows a faint residual tail towards the upfield centre.

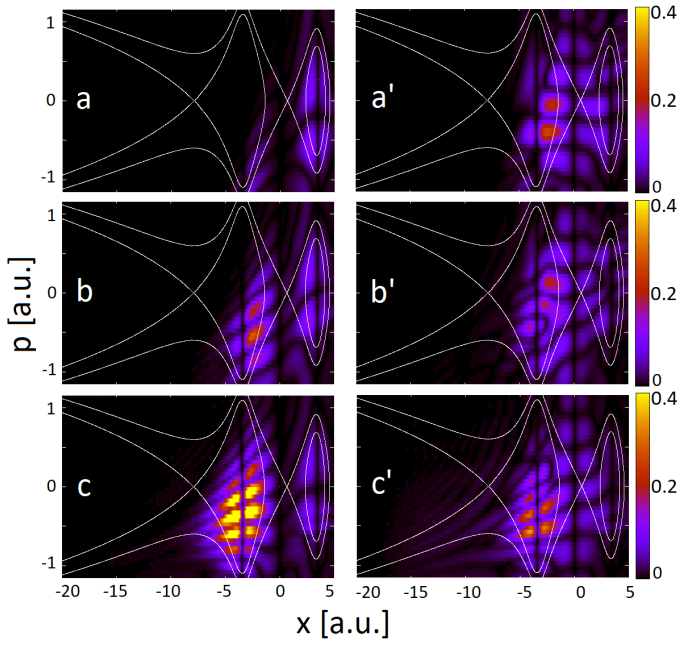

Figure 3.15: Phase space map of the quantum corrections $Q(x, p, t)$ [Eq. (2.3.2)] of a H_2^+ molecule of inter-nuclear distance $R = 6.8$ in a static laser field of strength $E = 0.0534$ a.u. (intensity $I = 10^{14}\mathrm{W/cm}^2$). The left column uses a localised upfield starting wave packet, while the right column ($'$) a delocalised one. Those are shown at times from top to bottom: $t = 5$ for (a) and (a$'$), $t = 10$ for (b) and (b$'$), and $t = 24$ for (c) and (c$'$). The separatrix of the system is shown by the white line.

The more intensely non-classical regions ($Q(x, p, t) > 0.2$ a.u.) are located at the quantum bridge, whether it is in the positive or negative momentum region [as seen in Figures 3.14 (d), (e) and (f)]. This also explains why those are absent from Fig 3.14 (c). By starting the initial wave packet downfield and because the inter-nuclear distance is too large, the quantum bridge is very faint. Most striking is the very bright ($Q(x, p, t) > 0.4$ a.u.) region in Fig 3.14 (d). A comparison with the second column of Fig 3.10(d$'$) shows that it occurs at the quantum bridge that passes through the downfield centre.

In Fig. 3.15, we compare the evolution of the quantum corrections for an initially delocalised wave packet $\Psi_{\mathrm{cat}}(x, 0)$ and a localised upfield wave packet $\Psi_{\mathrm{up}}(x, 0)$. There we see that the very high quantum corrections shown in the previous figure build up over time, and are only present when the downfield potential well starts to be populated. The early evolution of both systems, shown in Figure 3.15(a) and Figure 3.15(a$'$), are radically different. For an initially delocalised wave packet, the quantum bridge as well as the quantum corrections surrounding that bridge are present even at $t = 5$ a.u.. They fluctuate in time, as seen in Figs. 3.15(b$'$) and (c$'$). On the other hand, for an initial upfield wave packet, the quantum corrections form a steady uphill downhill flow. This supports the argument that there is a quantum

mechanism providing a shortcut for the electron to reach the semiclassical escape pathway. In both cases, the escape into the continuum appears to be governed by classical dynamics. Indeed the quasi probability flow follows an equienergy curve (as would classical trajectories) far from the core. This is expected as the interaction Hamiltonian is linear in the coordinate x and will be dominant in that region.

3.4 Conclusion

In this Chapter, we have performed a detailed analysis of strong-field enhanced ionisation using reduced-dimensionality models of diatomic molecules and phase-space methods, such as Wigner quasiprobability distributions and the quantum Liouville equation. Our studies show that enhanced ionisation stems from the interplay of at least two qualitatively different ionisation pathways, with an optimal phase-space configuration chosen to minimise population trapping and maximise direct downfield population transfer. One of these pathways follows the field gradient and leads to tails along separatrices that "spill" into the continuum, while the other does not obey field gradients or classical barriers in phase space. The former pathway may be associated with quasi-static tunnelling mechanisms [74, 77] as well as the semiclassical limit of Wigner quasi-probability distributions [135], with oscillatory tails around separatrices and equienergy curves. The latter pathway has been first identified in [191, 76] for oscillating driving fields. It consists of a cyclic motion performed by the Wigner function in phase space and the emergence of momentum gates, along which there is a direct quasiprobability flow from one well to the other. Therein, momentum gates were explained as resulting from strongly coupled states and the non-adiabatic response to the time-dependent field gradients.

We find, however, that this pathway occurs also for static fields, and even in the absence of driving fields altogether. By employing different types of initial bound states for the electronic wave packet, we show that the primary cause of the momentum gates in [191, 76] is quantum interference. If both wells are occupied, quantum interference will create a bridge that will support a direct intra-molecular quasiprobability flow. For initially delocalised (cat) states, quantum bridges are present from the start, while if the electron is initially located in the upfield molecular well they may build up with time. For that, it is necessary that enough quasiprobability density reaches the lower well. This can only happen if the molecular centres are close enough in order to guarantee a significant overlap between the quasi-probability density around the central molecular saddle and that located at the wells. For that very reason, the quantum bridges weaken for increasing inter-nuclear separation.

The quantum bridges perform a clockwise motion in phase space, and follow a single dominant frequency, which can be inferred directly using autocorrelation functions. For initial cat states, this motion extends over many cycles. This frequency is

strongly dependent on the internuclear separation and is barely affected by changes in the width of the initial wave packet. Since Gaussian wavepackets are coherent superpositions of eigenstates of this specific system, this hints at a resonant behaviour within the molecule. The frequency can also be estimated using classical arguments which however require closed separatrices allowing access to both centres. This condition is unfortunately met only for inter-nuclear separations $R < R_c$, i.e., smaller than that required for enhanced ionisation. Furthermore, the quantum corrections to the Liouville equation are quite large near the quantum bridges. This implies that the classical estimates presented in this work must be viewed with care. Still, they provide the correct direction of evolution for the Wigner functions, and yield reasonable agreement with the empirical quantum values. Away from the molecule, the quantum corrections vanish and the temporal evolution of the Wigner function is essentially classical.

Depending on the phase-space configuration around the two molecular wells, the quantum bridges may aid or hinder enhanced ionisation. For instance, for $R < R_c$, there are two nested separatrices and thus significant population trapping. Hence, the downfield population will be forced back to the upfield centre by the quantum bridge's clockwise motion and no enhanced ionisation will occur. In contrast, for larger inter-nuclear distances the outer separatrix will open. This implies that the quantum bridge may strongly connect the population of the upfield centre to the semiclassical escape pathway, thus providing a "shortcut" that will result in enhanced ionisation. This makes the initial upfield configuration so efficient: in that case, once the quantum bridge has been built, for optimal values of R it may not be able to resume its periodic motion in the uphill direction. This explains why an initial wave packet localised upfield and an inter-nuclear distance of $R = 6.8$ a.u. leads to the highest ionisation yield: The return is blocked by both the inter-nuclear distance and the lack of population initially in the downfield centre. An initial cat state is less efficient as the strong overlap stimulates the clockwise motion uphill. However, the quantum bridges will still feed the tails that built around various equienergy curves.

These conclusions lead us to two research lines explored in the following Chapters: Investigating the non-classical evolution around the quantum bridges, expanding on the results found from the quantum Liouville equation (Chapter 4) and the other focusing on the frequencies involved in the momentum gates phenomenon (Chapter 5).

Chapter 4

Ionisation dynamics using the Quantum Trajectory Method

From the investigation of the quantum Liouville equation, we brought forward in Chapter 3 the non-classical evolution of the momentum gates in enhanced ionisation. In this Chapter we aim to expand on this notion by investigating the quantum bridging mechanism with the quantum trajectory method (QTM), see section 2.4. The hydrodynamic formulation of quantum mechanics introduces quantum trajectories: They evolve following a velocity field, and the phase and amplitude of the wave function can be retrieved from them. This separates them from Bohmian trajectories, where the wavefunction is needed first to propagate them. The main limitation of QTM is the need to compute field derivatives on unstructured grids. As seen in Chapter 2.4, one such method parameterises the density. The trajectories can then be propagated using a Newton-like quantum equation of motion and the wave function does not need to be calculated at every time step to propagate every trajectory. This technique is also compelling because of its interpretative uses. Indeed, such a trajectory-based method will be best at visualising quantum phenomena such as quantum bridges in enhanced ionisation.

This Chapter is organised as follows. In section 4.1 we present our improvements to the discretisation of the density method found in [211, 212, 213]. First by using a central difference approach to the density approximation, and next by changing the expression of the quantum potential for the boundary trajectories. This leads to better accuracy and means fewer trajectories are needed to model the same phenomenon. We then use this new method in section 4.2 to study the tunnelling dynamics through different atomic binding potentials. This includes using the quantum potential as a criteria for non-classicality. Following these results in section 4.3 we apply this technique to the enhanced ionisation model investigated in Chapter 3 and unfortunately reach the limits of our model. We end the Chapter with a conclusion in section 4.4

4.1 Accuracy improvements

4.1.1 Density approximation

The value for the density used in [211] is $\rho_-(x_n) = \frac{1}{N(x_n - x_{n-1})}$. However it also admits in its derivation of the quantum potential

$$\rho_-(x_n) = \frac{1}{N(x_n - x_{n-1})} \approx \rho_+(x_n) = \frac{1}{N(x_{n+1} - x_n)} \tag{4.1.1}$$

In order to improve the accuracy of the approximation, using both ρ_- and ρ_+, we define a central difference approach:

$$\rho(x_n) = \frac{x_{n+1} - x_{n-1}}{2N(x_{n+1} - x_n)(x_n - x_{n-1})}. \tag{4.1.2}$$

The density ρ_- and ρ are compared in the study of the ground state of the harmonic oscillator

$$V_{HO} = \frac{1}{2} m\omega^2 (x - x_0)^2 \tag{4.1.3}$$

shown in Fig. 4.1 (a)-(b). To obtain the ground state, the trajectories are adjusted by setting the velocity to zero at every time step, a method also used in [212]. The central difference approach as expected better matches the density obtained from the TDSE, especially for the trajectories near the boundary. This is more evidently shown in Fig. 4.1 (c)-(d), where the density ρ defined using a central difference scheme is more accurate by 1.5×10^{-2} at the boundary trajectories. Moreso, the largest difference between the QTM density ρ and the analytical TDSE solution using only 31 trajectories is still smaller than the largest difference using the density ρ_- and 101 trajectories. This means fewer trajectories are needed to obtain results of matching accuracy.

The value of the density for the boundary trajectories is of upmost importance when studying rare events such as tunnelling. While the quantum potential does not influence the position of those trajectories, it does play a major role in obtaining their phase and their energy. For this reason the boundary conditions on the quantum potential are scrutinised in the following section as well.

4.1.2 Boundary conditions

With the Q_{CR} potential defined in Eq. (2.4.17), there is a glaring issue at the boundary points, where either x_{n+2}, x_{n+1} or x_{n-1} do not exist (for $n = 1$, $N-1$ and N). This is resolved in [212] by setting virtual points infinitely away to the left and to the right. This will for example set the ratio $1/(x_n - x_{n-1}) = 0$ for the $n = 1$ trajectory. While this is an acceptable method for the $n = 1$ and $n = N - 1$ trajectories, it fails for $n = N$. In the following derivation we aim to obtain an equally valid

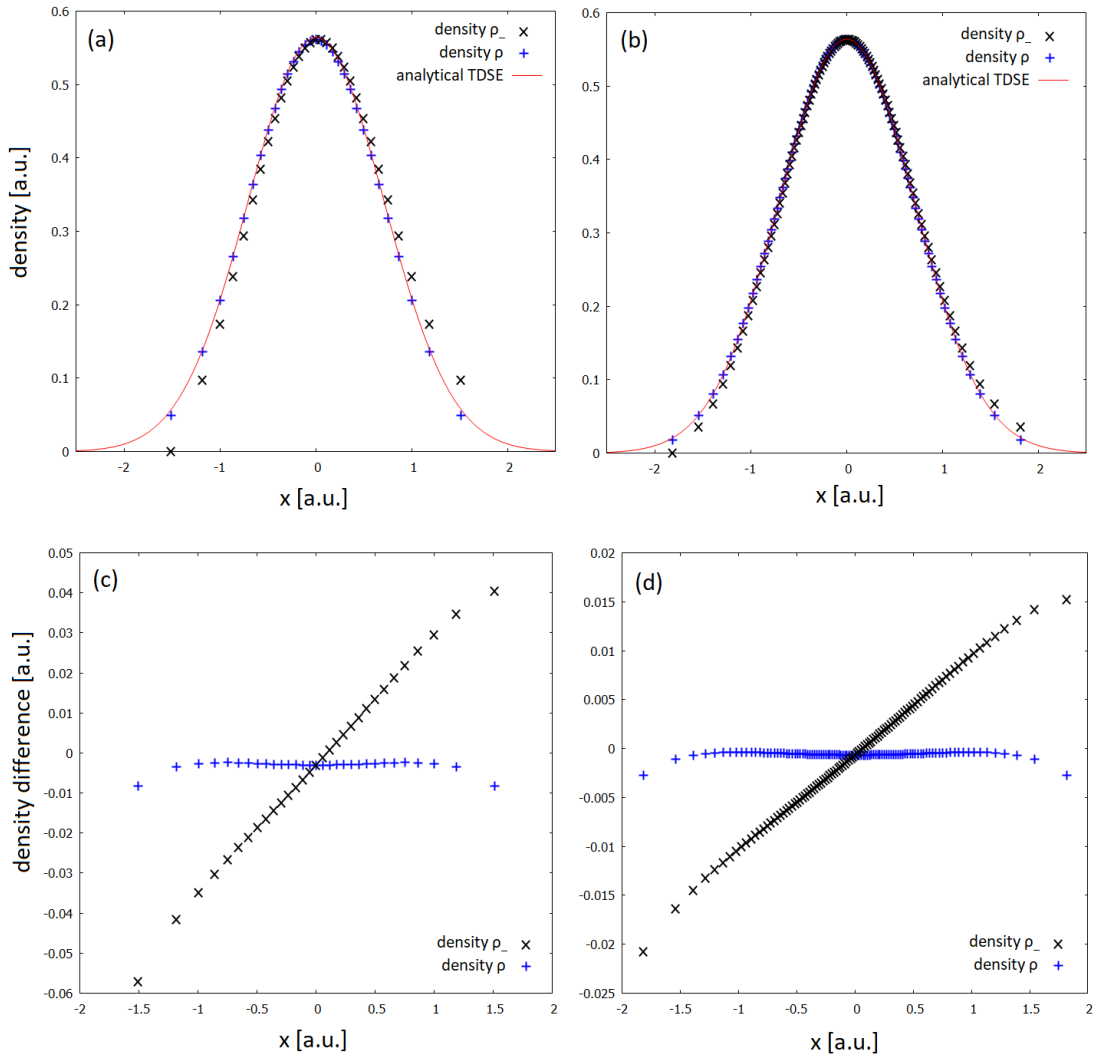

Figure 4.1: (a)-(b) Comparing the ρ with the ρ_- density of the harmonic oscillator potential from Eq. (4.1.3) with parameters $m = 1$ a.u., $x_0 = 0$ a.u. and $\omega = 1$ a.u. with the analytical solution from the TDSE using 31 trajectories in column one or 101 trajectories in column two propagating using a time step dt of 10^{-4} a.u.. (c)-(d) Plotting the difference with the TDSE analytical solution.

expression for the quantum potential that is well defined at the boundary trajectories. We start from the expression of the discrete second derivative $\varphi''(x_n)$ obtained in Eq. (2.4.15) using a forward scheme followed by a backwards scheme. Instead, we use the backward scheme first, followed by the forward scheme to calculate the second derivative. This gives

$$\varphi''(x_n) = \frac{\varphi'(x_n) - \varphi'(x_{n-1})}{x_n - x_{n-1}} \tag{4.1.4}$$

$$\varphi''(x_n) = \frac{\frac{\varphi(x_{n+1})-\varphi(x_n)}{x_{n+1}-x_n} - \frac{\varphi(x_n)-\varphi(x_{n-1})}{x_n-x_{n-1}}}{x_n - x_{n-1}}, \tag{4.1.5}$$

which, can then be used in the second derivative of the density

$$\frac{\rho^{''}(x,t)}{\rho(x,t)} = \frac{\rho_-(x_{n-1})}{\rho_-(x_n)}\frac{1}{(x_n - x_{n-1})^2} - \frac{1}{(x_n - x_{n-1})^2} - \frac{1}{(x_{n+1} - x_n)(x_n - x_{n-1})} + \frac{\rho_-(x_{n+1})}{\rho_-(x_n)}\frac{1}{(x_{n+1} - x_n)(x_n - x_{n-1})}. \tag{4.1.6}$$

This leads to an alternative expression for the quantum potential Q_{alt}:

$$Q_{alt}(x_n,t) = -\frac{\hbar^2}{4m}\left[\frac{1}{(x_n - x_{n-1})(x_{n-1} - x_{n-2})} - \frac{1}{(x_n - x_{n-1})^2} + \frac{1}{(x_{n+1} - x_n)^2} - \frac{1}{(x_{n+1} - x_n)(x_n - x_{n-1})} - \frac{1}{2}\left(\frac{1}{(x_{n+1} - x_n)} - \frac{1}{(x_n - x_{n-1})}\right)^2\right]. \tag{4.1.7}$$

Since both forms of the quantum potential in Eq. (2.4.17) and Eq. (4.1.7) are equivalent, we can combine them to obtain an expression for the quantum potential that uses information from both the forward and backward trajectories and is not undefined at the boundaries. The quantum potential for the centred trajectories (from 3 to $N-2$) takes the form of the average of both expressions. The trajectories 2 and $N-1$ use the Q_{CR} and Q_{alt} respectively. Trajectories 1 and N respectively use the Q_{CR} and Q_{alt} form setting x_{n-1} and x_{n+1} to $-\infty$ and $+\infty$. The complete expression is presented below.

$$
\begin{aligned}
Q(x_1,t) &= -\frac{\hbar^2}{4m}\left[\frac{1}{(x_{n+2}-x_{n+1})(x_{n+1}-x_n)} - \frac{1}{(x_{n+1}-x_n)^2} - \frac{1}{2}\left(\frac{1}{(x_{n+1}-x_n)}\right)^2\right] \\
Q(x_2,t) &= -\frac{\hbar^2}{4m}\left[\frac{1}{(x_{n+2}-x_{n+1})(x_{n+1}-x_n)} - \frac{1}{(x_{n+1}-x_n)(x_n-x_{n-1})}\right. \\
&\quad \left. + \frac{1}{(x_n-x_{n-1})^2} - \frac{1}{(x_{n+1}-x_n)^2} - \frac{1}{2}\left(\frac{1}{(x_{n+1}-x_n)} - \frac{1}{(x_n-x_{n-1})}\right)^2\right] \\
Q(x_n,t) &= -\frac{\hbar^2}{8m}\left[\frac{1}{(x_{n+2}-x_{n+1})(x_{n+1}-x_n)} - \frac{2}{(x_{n+1}-x_n)(x_n-x_{n-1})}\right. \\
&\quad \left. + \frac{1}{(x_n-x_{n-1})(x_{n-1}-x_{n-2})} - \left(\frac{1}{(x_{n+1}-x_n)} - \frac{1}{(x_n-x_{n-1})}\right)^2\right] \\
Q(x_{N-1},t) &= -\frac{\hbar^2}{4m}\left[\frac{1}{(x_n-x_{n-1})(x_{n-1}-x_{n-2})} - \frac{1}{(x_{n+1}-x_n)(x_n-x_{n-1})}\right. \\
&\quad \left. - \frac{1}{(x_n-x_{n-1})^2} + \frac{1}{(x_{n+1}-x_n)^2} - \frac{1}{2}\left(\frac{1}{(x_{n+1}-x_n)} - \frac{1}{(x_n-x_{n-1})}\right)^2\right] \\
Q(x_N,t) &= -\frac{\hbar^2}{4m}\left[\frac{1}{(x_n-x_{n-1})(x_{n-1}-x_{n-2})} - \frac{1}{(x_{n-1}-x_n)^2} - \frac{1}{2}\left(\frac{1}{(x_n-x_{n-1})}\right)^2\right]
\end{aligned}
\tag{4.1.8}
$$

The quantum potential Q then equally uses information from the forward and backward trajectories. This is shown by calculating the energy of individual trajectories in the ground state of the harmonic oscillator

$$E_n = \frac{p^2}{2m} + V(x_n) + Q(x_n), \tag{4.1.9}$$

as well as the average energy of the system

$$\langle E\rangle = \frac{1}{N}\sum_{n=1}^{N}\left[\frac{p^2}{2m} + V(x_n) + Q(x_n)\right]. \tag{4.1.10}$$

These results are shown in Table. 4.1 using the quantum potential Q_{CR} in Eq. (2.4.17) and the improved quantum potential Q in Eq. (4.1.8) defined above, using a varying number of initial trajectories. While the individual energy for all trajectories between $n = 1$ and $n = N - 1$ is of 0.5 a.u., the energy of the boundary trajectory $n = N$ is severely different from the ground state energy of the harmonic oscillator. This affects the average energy of the system, reaching only 0.48 a.u. instead of 0.50 a.u. for $N = 31$ trajectories,. This inaccuracy is suppressed when using more trajectories, as the average energy for $N = 101$ becomes 0.495 a.u..

The advantage of using Q instead of Q_{CR} is two-fold. First, the individual energy of the boundary trajectory is no longer inaccurate. This allows us to investigate the quantum potential of the boundary trajectory, which will be relevant when looking

Energy of trajectory	$N = 31$		$N = 101$	
	Q_{CR}	Q	Q_{CR}	Q
$n = 1$	0.50	0.50	0.500	0.500
$n = N - 1$	0.49	0.50	0.500	0.500
$n = N$	0.00	0.49	0.000	0.500
Average	0.48	0.50	0.495	0.500

Table 4.1: Table of the individual energy [Eq.(4.1.9)] of the $n = 1$, $n = N - 1$ and $n = N$ trajectory (where N is the total number of trajectory) as well as the total average energy [Eq.(4.1.10)] using either 31 or 101 trajectories, comparing results obtained using the quantum potential Q_{CR} and Q.

at rare events such as tunneling, and the dynamics of enhanced ionisation on an ultrashort timescale. Second, this means that fewer trajectories are needed to obtain a precise average energy. Indeed, the average energy using Q_{CR} and 101 trajectories is still less precise than the average energy found using Q and only 31 trajectories (0.495 versus 0.500). This, combined with the central difference approach density, means fewer trajectories will be needed to model the same phenomenon. Being able to model a system using the smallest number of trajectories greatly reduces computational time. Consequently both ρ from Eq.(4.1.2) and Q from Eq.(4.1.8) will be used throughout the rest of this Chapter.

4.2 Tunneling with QTM and non-classicality

Using the improved expression for the quantum potential described above, we aim to apply this method to atomic tunneling dynamics. We will be using the effective potential from Eq. (2.1.4) with a soft-core potential $V_{\mathrm{sc}}(x)$, see Eq.(2.1.5) and a static external field

$$E(t) = E_0. \tag{4.2.1}$$

To check whether the following observations hold for various model potentials and investigate the effect of the soft-core potential tail on the system dynamics, we will use as the binding potential $V(x)$ a truncated soft-core potential, defined below as

$$V_{\mathrm{Tr}}(x) = V_{\mathrm{sc}}(x)\mathrm{Tr}(x), \tag{4.2.2}$$

where the truncated function is the following

$$\mathrm{Tr}(x) = \begin{cases} 1, & \text{if } |x| < a_0, \\ \cos^7\left(\frac{\pi}{2}\frac{|x|-a_0}{L-a_0}\right), & \text{if } a_0 \leq |x| \leq L, \\ 0, & \text{if } |x| > L. \end{cases} \tag{4.2.3}$$

The parameters a_0 and L are chosen following [222, 206]. We will be using two

different truncated potentials: $\mathrm{Tr}_1(x)$ which eliminates the potential tail but keeps the core region unaltered, while potential $\mathrm{Tr}_2(x)$ is of extreme short range. Fig.4.2 shows the shape of the different potentials near the core.

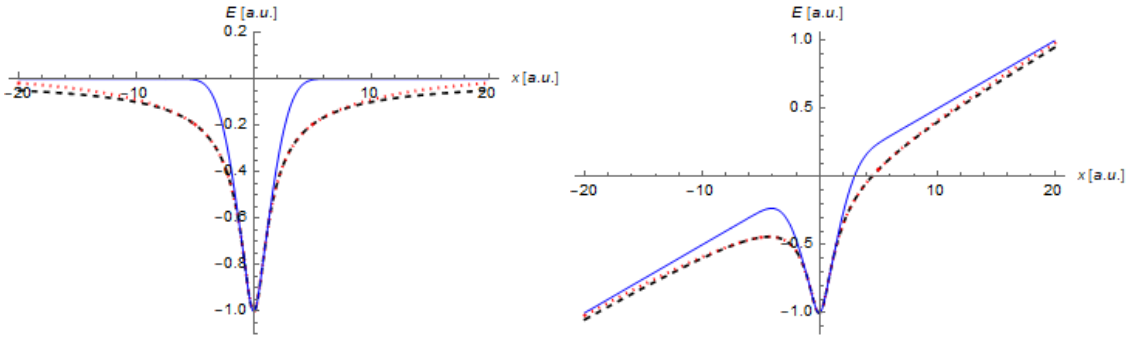

(a) (b)

Figure 4.2: (a) Comparison of the different potential energy in a field free system or (b) comparison of the effective potential energy $V_{\mathrm{eff}}(x)$ with a static field of strength $E = 0.05$ a.u. for the following potentials: soft-core potential (Eq. 2.1.5) [black-dashed line], truncated soft-core potential $\mathrm{Tr}_1(x)$ (Eq. 4.2.2) with parameters $a_0 = 5$, $L = 50$ [red-dotted line] and truncated soft-core potential $\mathrm{Tr}_2(x)$ (Eq. 4.2.2) with parameters $a_0 = 1$, $L = 5$ [blue-solid line].

The initial trajectories are prepared in the ground state of their respective binding potentials. The ground state of quantum trajectories is here defined as the state where the force, sum of the classical F_{C} and quantum F_{Q} force, acting on all trajectories is zero. These initial positions are obtained using the same relaxation method as in section 4.1. We then see how the time dependent energy E_n [Eq. (4.1.9)] of various individual trajectories compares to the effective potential energy $V_{\mathrm{eff}}(x)$.

These results are presented in Figure 4.3 for the soft-core potential and both truncated soft-core potentials. For all binding potentials, the initial positions of several ground state trajectories (and specifically shown here the first and fourth trajectories in [column 1] and [column 2]) are already out of the classical region and resting in the tunnelling region. While this makes the start of the tunnelling process non-trivial, in Fig. 4.3 (a), (a') and (a") we see a clear tunnel exit as the boundary trajectory crosses the effective potential. The time evolution of the quantum trajectories using the soft-core potential [first row] and the $\mathrm{Tr}_1(x)$ potential [second row] are near identical. This suggests that the long range effects of the soft-core tail are minimal within this scope. Removing long-range effects all-together with potential $\mathrm{Tr}_2(x)$ [third row] has more drastic effects. The boundary trajectory energy becomes superior to the effective potential at $t = 10$ for $\mathrm{Tr}_1(x)$ as opposed to $t = 15$ for $\mathrm{Tr}_2(x)$. The dynamics of the fourth trajectory involve more intense oscillations, especially with the soft-core potential [first and second row]. Its energy even briefly crosses that of the effective potential at $t = 23$. These variations can be attributed to fast changes in the quantum potential. Meanwhile, the trajectories around the core have a near constant energy well above that of the effective potential, despite their

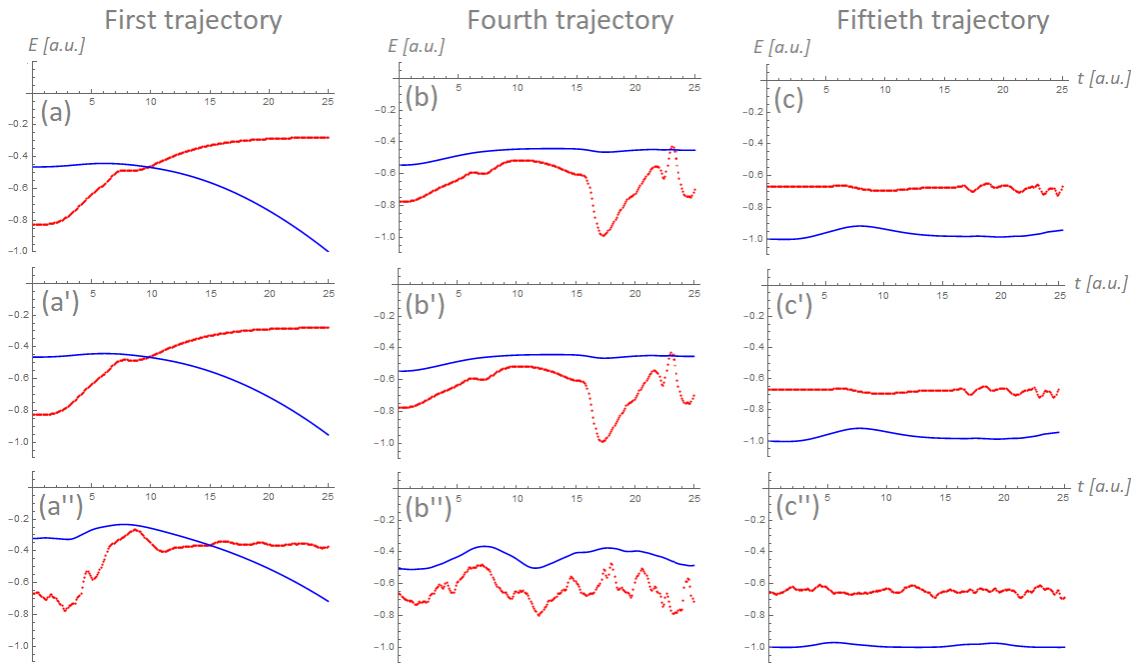

Figure 4.3: Evolution of time dependent energy of an individual trajectory Eq.(4.1.9) [Red dots] and the corresponding classical potential [Blue line], in a soft core potential (Eq. 2.1.5) [Top row], truncated soft-core potential 1 (Eq. 4.2.2) with parameters $a_0 = 5$, $L = 50$ [Second row] and a truncated soft-core potential 2 (Eq. 4.2.2) with parameters $a_0 = 1$, $L = 5$ [Third row] (using 101 trajectories) under the influence of a static laser field of strength $E_0 = 0.05$ a.u.. The individual trajectories chosen are the first, downfield one [panels (a), (a') and (a")], the fourth trajectory in the tunneling region [panels (b), (b') and (b")] and the fiftieth trajectory at the centre of the core region [panels (c), (c') and (c")].

momentum being negligible. This "extra" energy is also traced back to the quantum potential. The influence of the quantum potential is non-local, and strongest when trajectories are clustered together, which is especially true for the core trajectories.

We now analyse the phase space dynamics, see section 2.1, of the first two tunneling trajectories, as well as the evolution of their quantum potential. In Fig. 4.4(a) we see how the ionised trajectories initially do not follow any specific energy curve in phase space. As we saw in Chapter 3, this is associated with a non-classical evolution. However as they ionise and separate from the core, starting at position $x = -10$ a.u., their behaviour becomes analogous to that of a classical trajectory. In Fig. 4.4 (b), where the trajectory's individual quantum potential is shown depending on its position, we can see that from $x = -10$ a.u. their quantum potential tends to zero. On the other hand, the absolute value of the quantum potential around their starting position near the core grows very large.

As the quantum potential carries the non-classical contributions, and it reaches zero when the trajectories follow equi-energy curves in phase-space, we now aim to examine the evolution of the quantum potential around the momentum gates investigated in Chapter 3. Conceivably this will be another criteria for non-classicality, and will emphasise the quantum bridging phenomenon.

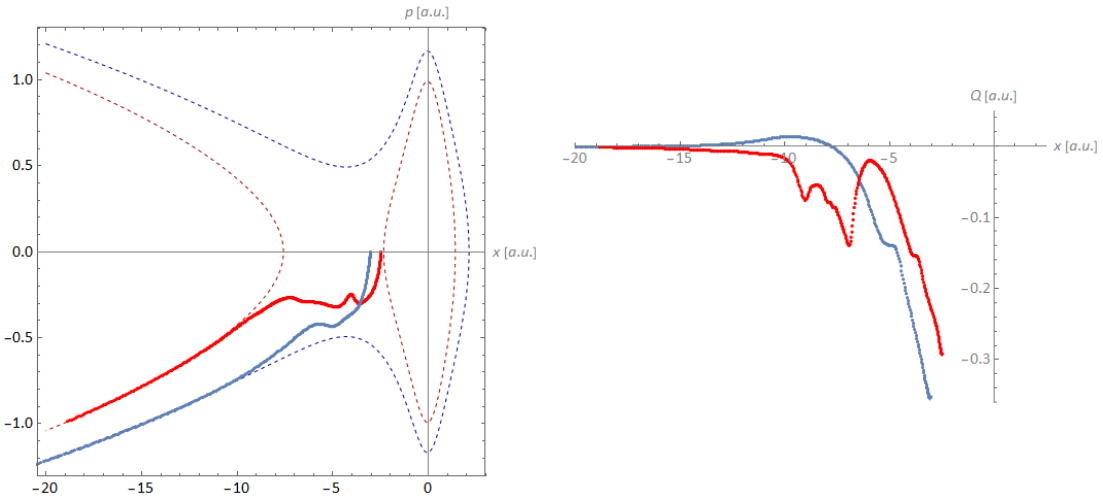

(a) (b)

Figure 4.4: (a) Phase Space representation of the evolution of the first (in blue) and second (in red) QTM trajectory in a soft core potential (using 101 trajectories) under the influence of a static laser field of strength $E_0 = 0.05$ a.u.. The dotted lines are the two corresponding equal energy curves of $e = -0.51$ a.u. (blue) and $e = -0.32$ a.u. (red). (b) Value of the quantum potential of the first (in blue) and second (in red) trajectory in the same conditions as (a) as they evolve with time.

4.3 Quantum potential in enhanced ionisation

Having set the background for atomic tunneling dynamics using quantum trajectories, we can now apply this method to enhanced ionisation, focusing on the dynamics of the trajectories at the quantum bridge. To this end we will use the molecular binding potential

$$V(x) = V_{\text{sc}}(x - R/2) + V_{\text{sc}}(x + R/2), \tag{4.3.1}$$

Where V_{sc} is the soft-core potential defined in Eq. (2.1.5), and R is the internuclear distance. An initially localised upfield set of trajectories is displayed in phase space in Figure 4.5. Early in the ionisation process, before the formation of the quantum bridge in Fig. 4.5(a), trajectories cross the bound phase space region and follow a path parallel to the separatrix. The corresponding quantum potential in Fig. 4.5(c) is as expected high for the core trajectories, and low (but non-negligible) for the escaping population. We now finally look at the behaviour of the quantum trajectories around the presence of the quantum bridge. Their dynamics are erratic, individual trajectories rapidly switching from negative to positive momenta. This is reflected by the snapshot in Fig. 4.5(b). The same uncontrolled behaviour is present in the quantum potential, the escaping trajectories having a highly oscillating quantum potential. Unfortunately, this is quite likely due to limitations with this computational method. Indeed, from the expression of the calculated numerically quantum potential, when trajectories are squeezed together too closely

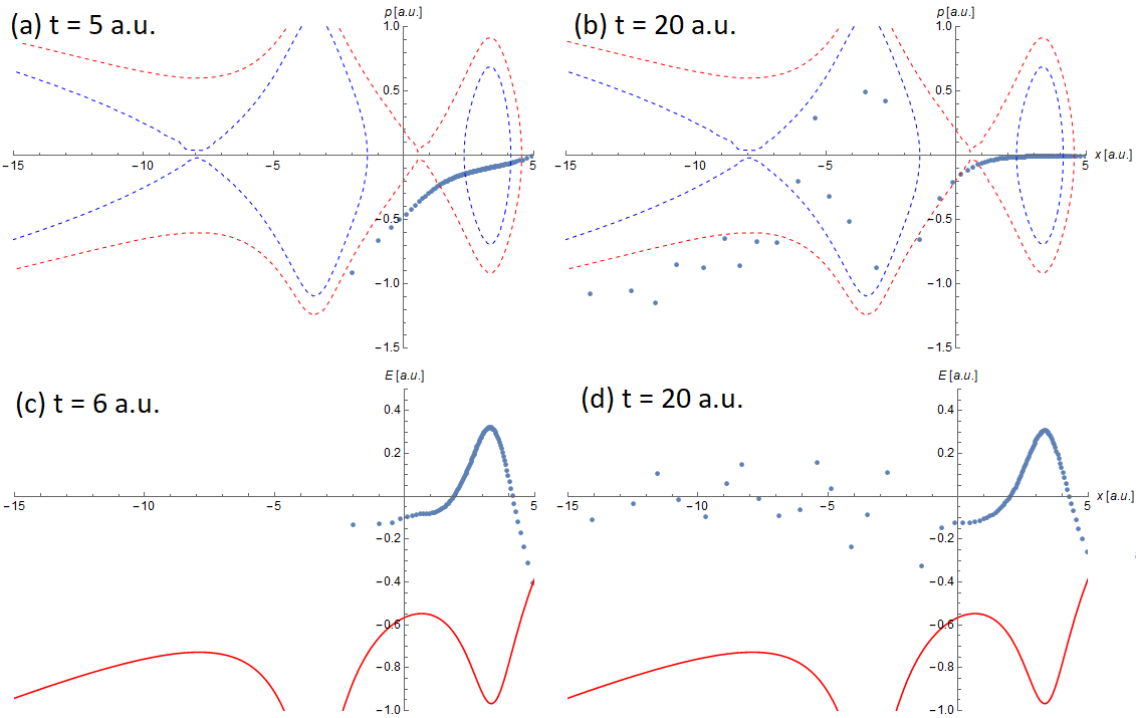

Figure 4.5: [First row] Phase space representation of the evolution of each individual 101 quantum trajectories (in blue) in a molecular soft core potential [Eq. (4.3.1)] with internuclear distance $R = 6.8$ a.u. under the influence of a static laser field of strength $E_0 = 0.0534$ a.u. for (a) $t = 5$ a.u. and (b) $t = 20$ a.u.. The red and blue dashed lines are the two separatrices, see section 2.1. These conditions matches those of Figure 3.10 (a') and (c') from Chapter 3. [second row] Value of the quantum potential of 101 trajectories in the same conditions and the effective potential (red line) for (c) $t = 6$ a.u. and (d) $t = 20$ a.u..

their propagation becomes unstable. The is the case as soon as trajectories reach the downfield potential well. The issue worsens when using an initially delocalised wavepacket, or propagating the trajectories for longer time periods.

4.4 Conclusion

In this Chapter, we have attempted to apply the QTM propagation using a discretised density method to expand on the non-classical evolution of the momentum gates and their quantum bridging mechanism. This is first done by improving the method in [211, 212, 213] to more accurately display the quantum potential of the boundary trajectory. When investigating atomic tunneling in a static field, we provide a link between the ionisation dynamics and the evolution of the quantum potential for individual trajectories. Core trajectories having a high quantum potential, tunneling trajectories having a oscillating quantum potential and trajectories following the semiclassical escape pathway with a quantum potential tending to zero. Those trajectories also follow classical phase space equi-energy curves.

However, one should note that the beginning of numerical issues of this method

arise around the peak density (where the trajectories are the most compacted), or when the quantum potential encounters rapid change. This makes using these trajectories in double well potentials numerically challenging (confirming observations from [213]). Unfortunately, this means we were unable to provide clear conclusions on the evolution of quantum trajectories in momentum gates.

In the following Chapter, we will instead focus on the non-classical frequency of the momentum gates by isolating the phenomenon, fully discern the frequencies involved analytically, and understand the behaviour observed for time-dependent fields.

Chapter 5

Time scales of quantum bridges

In this Chapter we will investigate the frequency of momentum gates and their interplay with the external field. Momentum gates, which have been first identified in the context of strong-field enhanced ionisation in position-momentum phase space using Wigner quasiprobability distributions [76], are lines of approximately constant momentum through which there is a direct intra-molecular quasiprobability flow from one molecular centre to the other. They have been attributed to the non-adiabatic effect of a transient electron localisation at one of the wells due to the presence of a strong laser field. In Chapter 3 we have shown that a time-dependent field is not a necessary prerequisite for the momentum gates to occur and that the strong quasi-probability transfers may occur through a "quantum bridge". These are highly non-classical, cyclic structures that form due to quantum interference. The aim of this Chapter is to provide an analytical justification for the behaviour found numerically in Chapter 3 and to expand our conclusions to a time-dependent external field system. We will do this by separating this Chapter into two parts. In part 5.1, we focus on a field-free system to isolate the quantum bridging phenomenon and quantify its evolution for different initial wavepackets. Using this model enables the analytical method described in section 2.5. In section 5.1.1 we obtain the autocorrelation function as well as the eigenfrequencies involved. We also check the correspondence of the numerical method of Chapter 3 and the analytical method of [215] throughout. Following that, in section 5.1.2, we focus on the system's phase-space evolution using the Wigner quasiprobability distribution. Finally, we extend these conclusions by adding a static field in section 5.1.3. Then, in part 5.2, using these conclusions along with the system explored in chapter 3, we investigate the presence and effect of momentum gates in a time-dependent field. This is done with various initial states and internuclear distances. Finally, we end this chapter with a conclusion on the behaviour of momentum gates and their interplay with time-dependent fields in section 5.3.

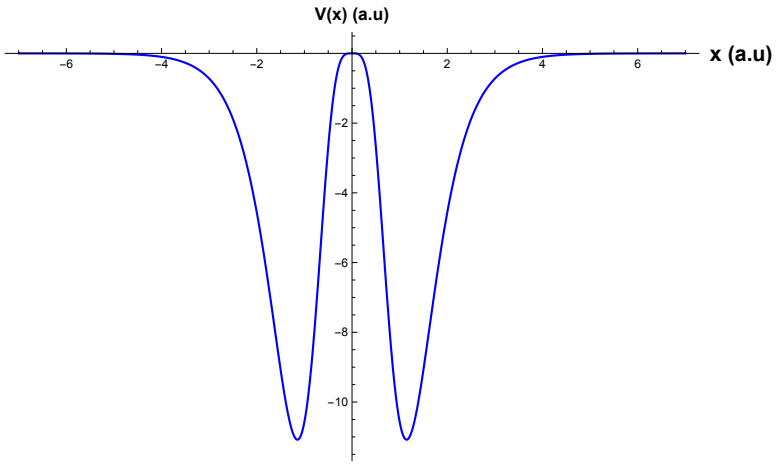

Figure 5.1: Plot of the hyperbolic double-well potential [Eq. (5.1.1)] with parameters $V_0 = 74.785$ a.u., $d = 1$ a.u. used throughout this section.

5.1 Insight from analytical model

Here we will apply the analytical model developed in [215] and introduced in section. 2.5 to the tunneling dynamics of an electronic wave packet, with focus on non-adiabatic temporal evolution. Indeed, it is ideally placed for an in-depth study of how the initial electronic wavepacket influences this motion, and how it is related to the system's eigenfrequencies. Specifically, a hyperbolic double well potential has several desirable properties for the molecular toy model. First, the limit $V(x) \to 0$ as $x \to \pm\infty$ allows for the existence of continuum of a states for positive electron energies. This is in contrast to the models of double-well potential by e.g. [223] or [224] for which $V(x) \to \infty$ as $x \to \pm\infty$. Second, it allows to faithfully model the binding potential in the region of interest (i.e. close to the central barrier as seen in Chapter 3). Third, the location of the (symmetric) wells and peak value of $V(x)$ may be independently tuned. Finally, although other hyperbolic double-well models such as those developed by [225] or [226] can reliably model the central potential barrier, the one we are using leads to an impenetrable barrier by classical means. This is important to rule out other population-transfer mechanisms.

5.1.1 Temporal evolution of the wavepacket

The hyperbolic binding potential

$$V(x) = -V_0 \frac{\sinh^4(x/d)}{\cosh^6(x/d)}, \tag{5.1.1}$$

where V_0 specifies the depth of the potential and d its peak location, is used throughout this section for the reasons explained above. It is represented in Figure 5.1. The wavepacket, the eigenenergies and the eigenfunctions are calculated analytically as discussed in section 2.5. The eigenfunctions corresponding to the potential in Fig-

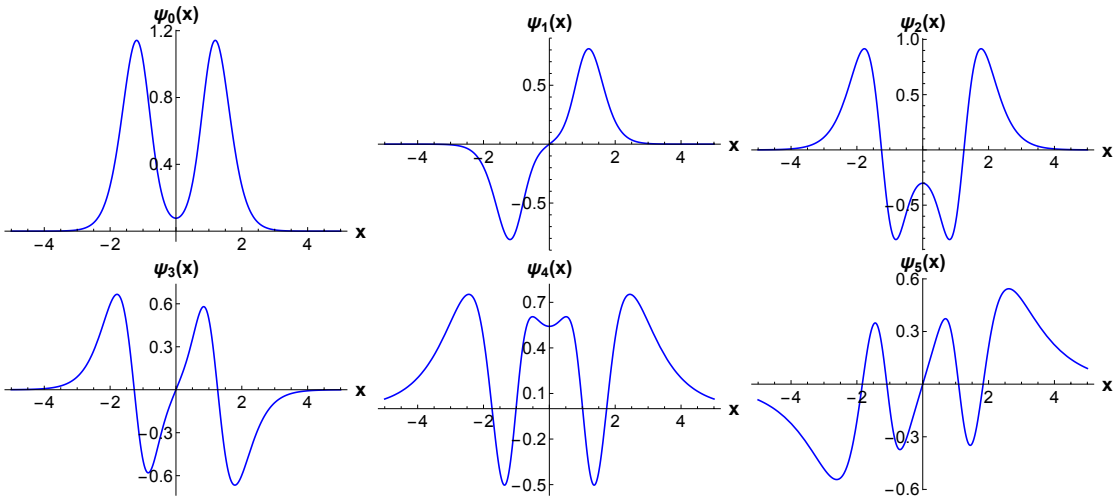

Figure 5.2: Plots of all the bound-state eigenfunctions for the hyperbolic potential [Eq. (5.1.1)] with parameters $V_0 = 74.785$, $d = 1$ shown in Figure 5.1. The corresponding eigenenergies (displayed to three significant figures) are: $E = \{-8.153, -8.141, -3.419, -3.298, -0.697, -0.441\}$.

ure 5.1 are shown in Figure 5.2.

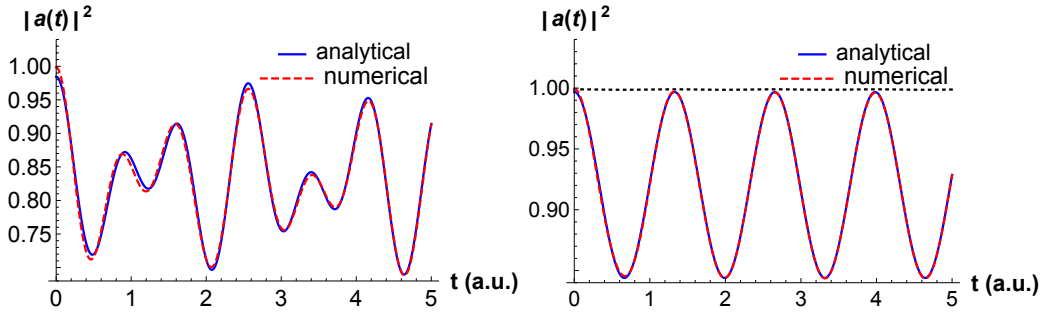

(a) (b)

Figure 5.3: Comparison of behaviour of $|a(t)|^2$ calculated using a potential defined by Eq.(5.1.1) and the analytical method (blue, solid line) described in Sec. 2.5 or the numerical method (red, dashed line) in 2.2. In panel (a) $c = 4$, $\Omega = 1/4$ and in panel (b) $c = 7$, $\Omega = 1/4$. The horizontal, black, dotted line in panel (b) corresponds to parameters $c = 7, \Omega = 3/10$, for which the initial wave packet very closely resembles the $\psi_0(x)$ eigenstate, hence having only a minute time dependence. The parameters of the potential [Eq. (5.1.1)] are $V_0 = 74.785$ a.u., $d = 1$ a.u. which corresponds to internuclear distance $R \approx 2.28$ a.u..

The even-parity, delocalised initial wavepacket $\psi_{\mathrm{DLE}}(\xi, c, \Omega)$, where

$$\psi_{\mathrm{DLE}}(\xi, c, \Omega) = \frac{\xi^{c\Omega} e^{-c\xi}}{\sqrt[4]{\pi}\sqrt{{}_1\tilde{F}_1\left(2c\Omega; 2c\Omega + \frac{1}{2}; -2c\right)}\sqrt{\Gamma(2c\Omega)}}, \tag{5.1.2}$$

admits two parameters, c and Ω, that respectively specify the width of the wavepacket and the location of its peak. Indeed, the x-space peak locations can be retrieved from Ω by inverting the $x \to \xi$ mapping to produce $x = \pm d \cosh^{-1}\left(1/\sqrt{\Omega}\right)$. To infer the time evolution of a wavepacket the autocorrelation function Eq. (2.2.5) will be

obtained analytically using

$$a(t) = \int_{-\infty}^{+\infty} \Psi^*(x,t)\Psi(x,0)dx = \sum_n |\Lambda_n|^2 \exp\left(\frac{iE_n t}{\hbar}\right),$$

where Λ_n are the overlap integrals defined in Eq. (2.5.5). Therefore

$$|a(t)|^2 = \sum_n \sum_m |\Lambda_n|^2 |\Lambda_m|^2 \exp\left(i(E_m - E_n)t/\hbar\right). \tag{5.1.3}$$

Any time dependence of $|a(t)|^2$ will stem from the differences in eigenenergies. Note that if $|\Lambda_n| \neq 0$ and $|\Lambda_m| \neq 0$ only for one pair of n and m with $n \neq m$ then $|a(t)|^2$ will oscillate with a single frequency. Otherwise, the time evolution will be more involved.

The results are presented here for two different sets of parameters, each corresponding to a different limit behaviour. The absolute value squared of the autocorrelation function $|a(t)|^2$ is displayed in Fig. 5.3 for even-parity delocalised wavepackets of different widths defined by Eq. (2.5.11) in the double well potential defined by Eq. (5.1.1). They have been computed analytically using the method described in section 2.5, and numerically using the method in Chapter 3. The agreement is excellent, with the analytical and numerical curves being practically indistinguishable and the temporal behaviours depending critically on the width.

In Fig. 5.3(a) this behaviour is quite intricate with two main frequencies: $\omega_{20} = 4.73$ a.u. and $\omega_{40} = 7.46$ a.u.. This is due to the coupling of $n = 0$ with $n = 2$, and $n = 0$ with $n = 4$ eigenstates (as Λ_2 and Λ_4 are small the $n = 2$ with $n = 4$ coupling may be safely neglected). In contrast, in Fig. 5.3(b), one can identify a single frequency for $|a(t)|^2$, namely $\omega_{20} = 4.73$ a.u., which corresponds to only one *pair* of states with non-vanishing overlap integrals: Λ_0 and Λ_2. Finally, the straight horizontal line in panel (b) corresponds to an initial wavepacket being very close to an eigenstate. As expected, this leads to a constant $|a(t)|^2$ within the precision used here. Minor discrepancies between the analytical and numerical results are related to the former not including overlaps with scattering states.

5.1.2 Phase-space dynamics

Next we will investigate the wave packet's phase space evolution, with emphasis on the quantum bridges and their periodic motion. For that purpose, we will employ the Wigner quasiprobability distributions given by Eq. (2.3.1). In the analytical model $W(x,p,t)$ may be calculated by numerical integration of Eq. (2.3.1), with the temporal evolution of the wavepacket $\Psi(x,t)$ given by Eq. (2.5.4).

Throughout, we will focus on the scenario for which the quantum bridges are strong, namely initially delocalised wave packets and intermediate internuclear separations. The results comparing the present analytical model and the numerical

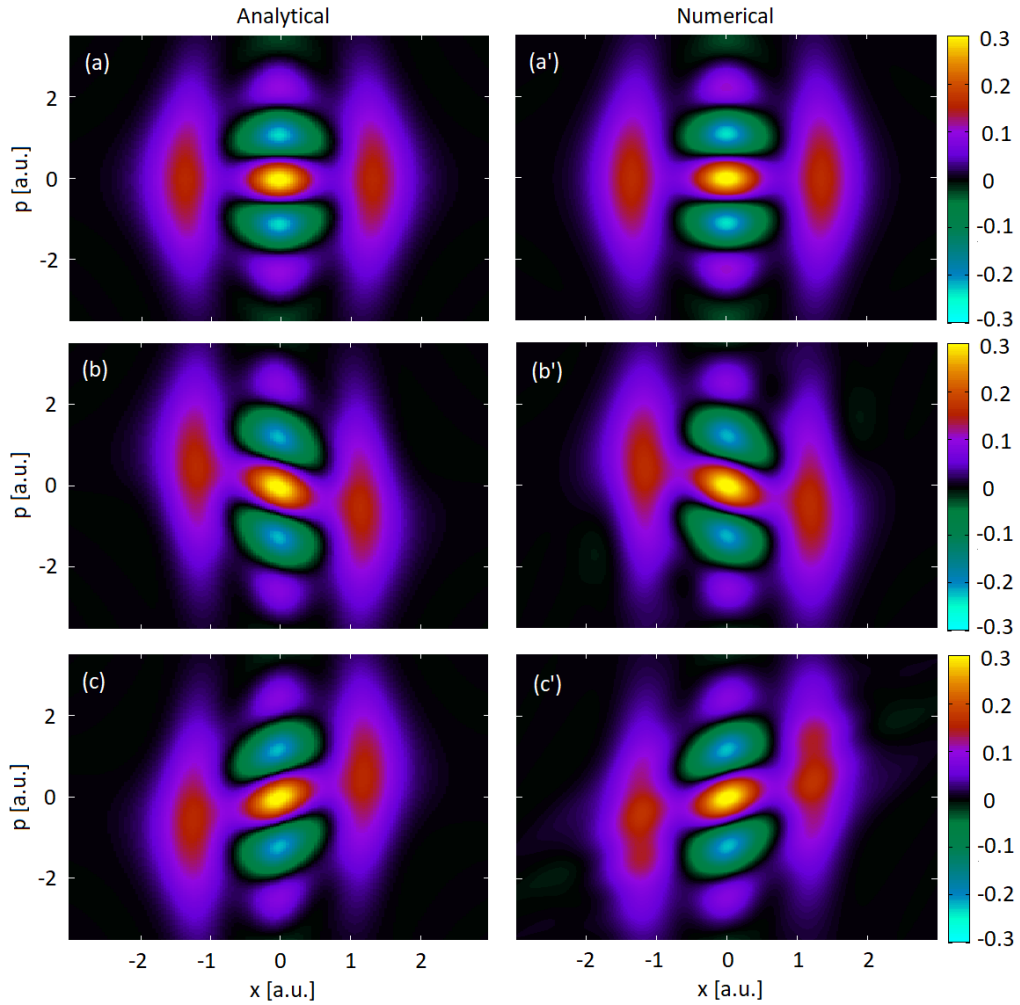

Figure 5.4: Comparison of Wigner quasiprobability distributions using the same parameters as in Fig. 5.3(b) ($c = 7, \Omega = 1/4$, $R = 2.28$) computed analytically (left panels) and numerically (right panels) for the times (a) $t = 0$, (b) $t = 0.4$ and (c) $t = 1.0$.

results in Chapter 3 are displayed in Figs. 5.4 and 5.5. Fig. 5.4 corresponds to an initial wave packet leading to a single oscillation frequency in the autocorrelation function, while in Fig. 5.5 a more involved scenario with superimposed oscillations is explored. Overall, the agreement between the numerical and analytical results is excellent, which once more shows that the present model is reliable and can be used to determine the temporal evolution of the quantum bridges exactly.

In Fig. 5.4, we display the Wigner quasiprobability distribution computed using the initial wavepacket in Fig. 5.3(b). The figure shows a quasiprobability flow from one centre to the other, with a strong quantum bridge near $p = 0$. As the time flows, there is a motion of frequency $\omega_{20} = 4.73$ a.u., which corroborates the statement that only the overlap integral between the ground and second excited state is relevant to the problem at hand. The plot corresponds to almost a whole period of the autocorrelation function, and illustrate an oscillating behavior in the Wigner quasiprobability distribution. The bridges become slanted, change slope and then

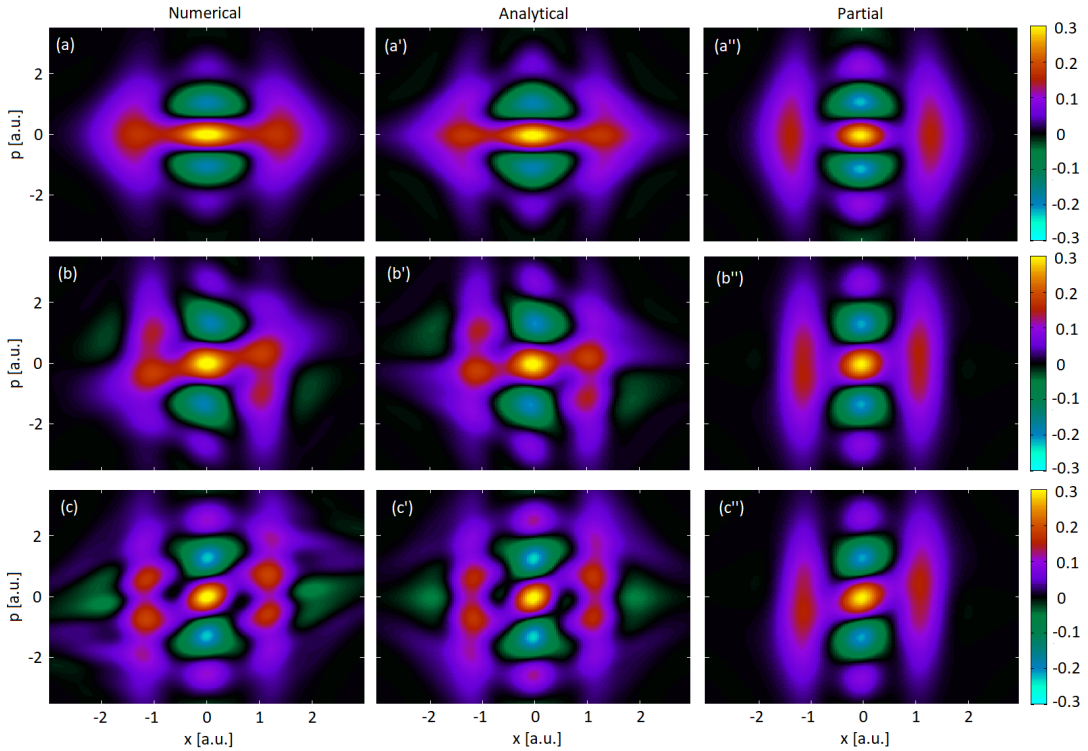

Figure 5.5: Comparison of Wigner quasiprobability distributions using the same parameters as in Fig. 5.3(b) ($c = 4, \Omega = 1/4$, $R = 2.28$) computed numerically (left panels) and analytically (middle panels) for the times (a), (a') and (a") $t = 0$; (b), (b') and (b") $t = 0.7$; and (c), (c') and (c") $t = 2.1$. In the rightmost panels the Wigner quasiprobability distribution is computed using the analytical model for the partial coherent superposition in Eq. (5.1.4).

return to their original configuration at $T \approx 1.33$ a.u. (not shown).

Fig. 5.5, in contrast, illustrates the phase-space evolution if we use the parameters in Fig. 5.3(a). The quasiprobability flow behaves in a much more convoluted way, with additional maxima near the quantum bridge and in both wells. For longer times, there will also be tails in the Wigner functions moving away from the potential wells, which indicate an overlap with a delocalised eigenstate, or in some cases ionisation. These tails are visible in the bottom panels of Fig. 5.5.

From the autocorrelation function, we expect that the frequencies ω_{20} and ω_{40} will play a role. This convoluted behavior will be discussed in the rightmost column of Fig. 5.5, in which, instead of constructing Wigner quasiprobability distributions using the full analytical wavefunction, we consider only a coherent superposition

$$\Psi_{20}(x,t) = \Lambda_0 \exp\left(-iE_0 t/\hbar\right) \psi_0(x) + \Lambda_2 \exp\left(-iE_2 t/\hbar\right) \psi_2(x), \tag{5.1.4}$$

between the ground and second excited state, where the overlap integrals $\Lambda_n (n = 0, 2)$ are given by Eq. (2.5.5). The partial Wigner quasiprobability flow mirrors the overall behavior reported in the central column of Fig. 5.5 except for the substructure and the tails. It determines the existence of the quantum bridges and their

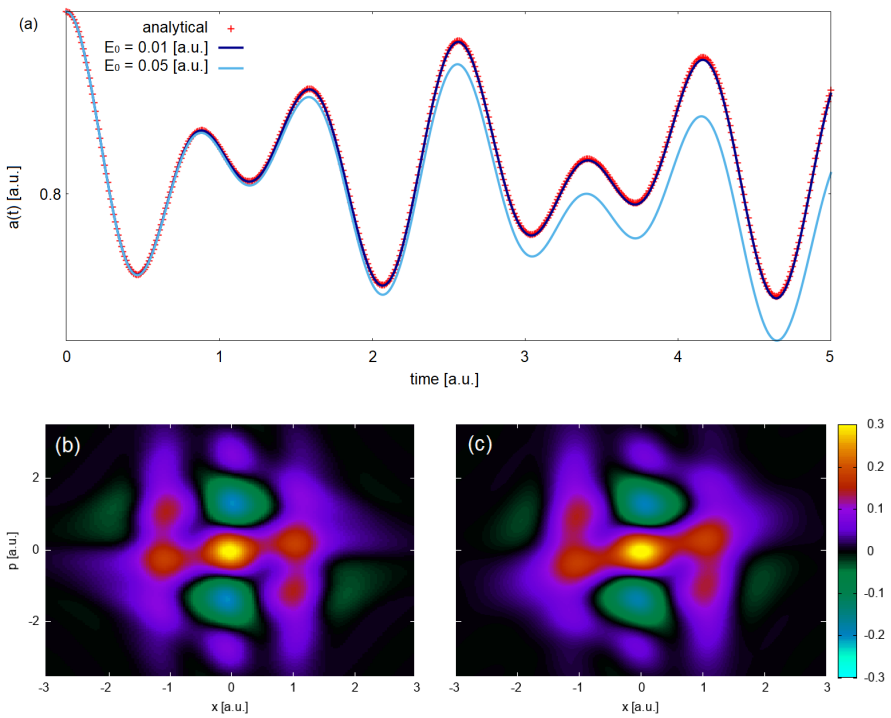

Figure 5.6: (a) Comparison between the absolute value of the autocorrelation function $|a(t)|^2$, see Eq. (2.2.5), calculated using the analytical method in section 2.5 in a field free system (red, dotted line) and numerical computations from section 2.2 using the hyperbolic potential [Eq. (5.1.1)] with $V_0 = 74.785$ a.u., $d = 1$ a.u. but with a static field of strength $\mathcal{E}_0 = 0.01$ a.u. ($I = 3.51 \times 10^{12}\mathrm{W/cm^2}$) (dark blue solid line) and $\mathcal{E}_0 = 0.05$ a.u. ($I = 1.72 \times 10^{14}\mathrm{W/cm^2}$)(light blue solid line). [Bottom row] Wigner quasiprobability distributions using the same parameters as (a) at time $t = 0.7$ a.u. using in panel (b) the analytical method in section 2.5 for a field free system and in panel (c) the numerical method from section 2.2 for a static field of strength $\mathcal{E}_0 = 0.05$ a.u. ($I = 1.7 \times 10^{14}\mathrm{W/cm^2}$).

slopes, whose time evolution has the frequency ω_{20}. This shows the dominance of this specific coupling and is expected, as tunneling should be dominated by the lower frequency. However, a modulation is introduced due to the non-vanishing overlap between the ground and the fourth excited state and its higher frequency ω_{40}. Furthermore, the tails are absent in the partial results. This is due to the missing overlap integral with the fourth excited eigenstate, which is significantly broader (see Fig. 5.2).

5.1.3 Static external field

Finally, we will verify that for this model potential the frequencies computed analytically are quite robust upon inclusion of an external static field. This is illustrated in Fig. 5.6. Indeed, from the autocorrelation function in Fig. 5.6 (a), the inclusion of a static field of strength $E_0 = 0.01$ a.u. has negligible effect on the autocorrelation function (and by extension the frequency of the quantum bridging mechanism). Even a stronger external static field, $E_0 = 0.05$ a.u., maintains the overall pattern.

This is also reflected in Fig. 5.6 (b) and (c), where we compare snapshots of the Wigner quasiprobability distribution between a field-free system and with an additional static field $E_0 = 0.05$ a.u.. The features attributed to the quantum bridges prevail despite the inclusion of the static field.

5.2 Interplay of the time dependent external field

In molecular enhanced ionisation, it is paramount to understand the timescale of formation of the quantum bridge as well as its cyclical motion, and how it relates to the frequency of the time-dependent field. As seen in the previous section, the quantum bridge and its frequency is inherent to the molecular system and due to the coupling of different eigenstates. In this section, following the thorough analysis of ionisation in static and vanishing fields, we can now finally disentangle the effects shown by the Wigner function in a time-dependent field.

In the previous analytical calculations and their numerical counterparts, a parabolic potential model was employed. This was done to facilitate the analytical investigation. For the remainder of the Chapter we will modify our system to numerically look at a time-dependent field, solving the TDSE following the method in section 2.2, and instead use the molecular binding potential $V(x)$ given by

$$V(x) = V_{\text{sc}}(x - R/2) + V_{\text{sc}}(x + R/2), \tag{5.2.1}$$

where each potential well V_{sc} is chosen be the soft-core potential defined in Eq. (2.1.5), and R is the internuclear distance.

The external laser field $\mathcal{E}(t)$ is chosen as a linearly polarised monochromatic wave

$$\mathcal{E}(t) = E_0 \cos(\omega t), \tag{5.2.2}$$

of strength E_0 and frequency ω.

The initial wavepacket chosen is a delocalised wavepacket

$$\Psi_{\text{cat}}(x, 0) = \frac{\Psi_{\text{down}}(x, 0) + \Psi_{\text{up}}(x, 0)}{\sqrt{2\,(1 + \mathcal{I}_o)}}, \tag{5.2.3}$$

where $\mathcal{I}_o$ is the overlap integral, $\Psi_{\text{down}}(x, 0)$ is a wavefunction localised around the downfield well and $\Psi_{\text{up}}(x, 0)$ localised around the upfield well. The localised wavefunctions are approximated by Gaussian wavepackets defined in Eq (2.2.4). The binding potential Eq. (5.2.1) and initial wavepacket Eq. (5.2.3) are identical to those used throughout Chapter 3, and will allow direct comparison with the static field results.

A key issue is how the periodicity of the external field will affect that of the quantum bridges and their cyclic motion. These are shown in Figure 5.7 using a

initial delocalised state and inter-nuclear distances $R = 4$ a.u., $R = 6.8$ a.u. and $R = 14$ a.u..

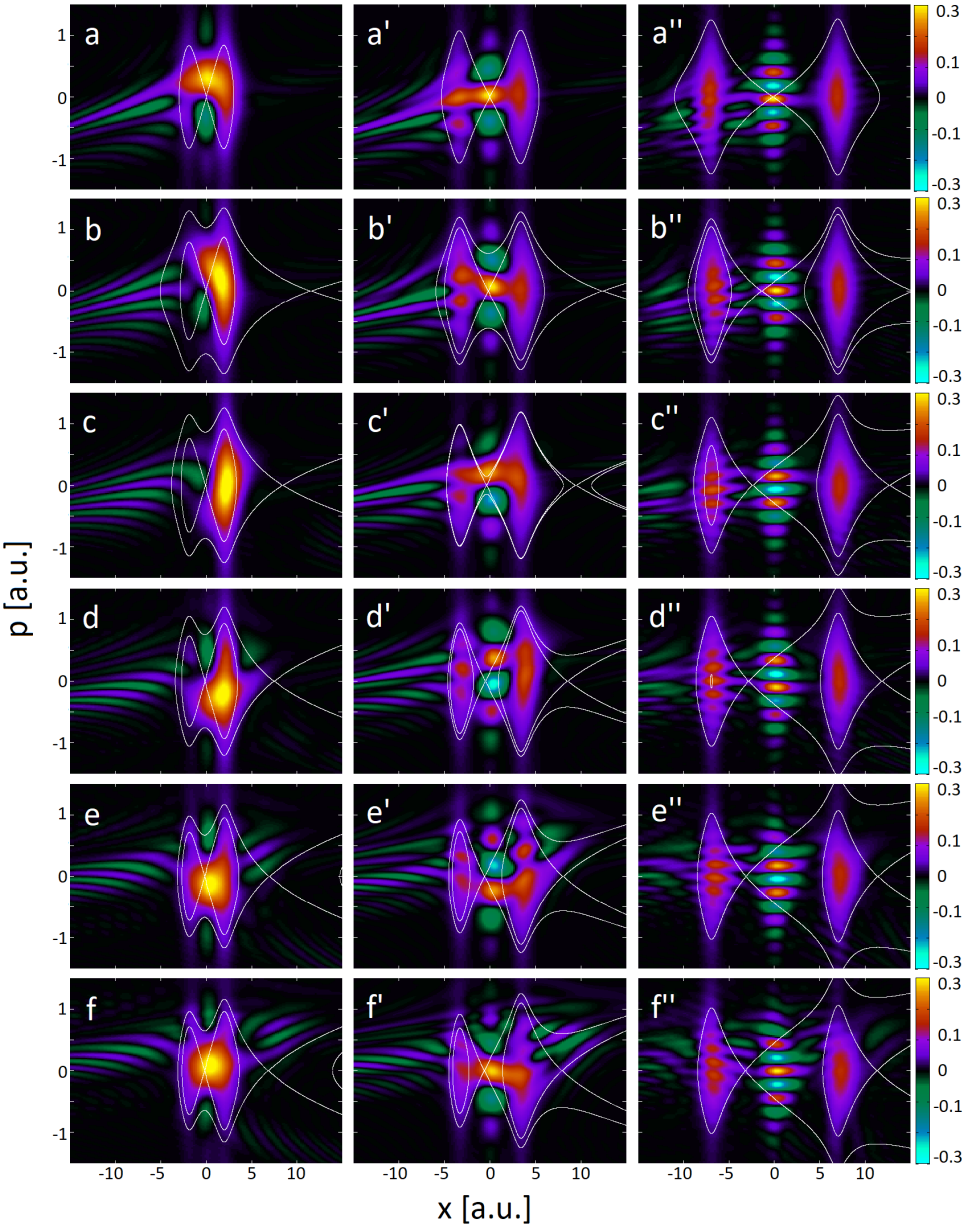

Figure 5.7: Wigner quasi probability distribution of a model H_2^+ molecule in a monochromatic laser field given by Eq. (5.2.2) of wavelength $\lambda = 800$nm and strength $E = 0.0534$ a.u. (intensity $I = 10^{14}\mathrm{W/cm}^2$) with inter-nuclear distance $R = 4$ (left), $R = 6.8$ (middle) and $R = 14$ (right) at different instants of time: $t = 0.25T$ [(a), (a′) and (a″)], $t = 0.30T$ [(b), (b′) and (b″)], $t = 0.35T$ [(c), (c′) and (c″)], $t = 0.40T$ [(d), (d′) and (d″)], $t = 0.45T$ [(e), (e′) and (e″)]and $t = 0.50T$[(f), (f′) and (f″)] from top to bottom, where T is the laser period and $T = 110.2$ a.u. (or $T = 2.7$ fs).

The Wigner function is plotted over a quarter of the field cycle, from a field crossing [top panels, denoted (a), (a′) and (a″)] to a maximum field amplitude [bottom panels, denoted (f), (f′) and (f″)]. Prior to that, we have allowed the Wigner function to evolve over a quarter of a cycle, from the previous field extremum to the crossing. This is evidenced by the tails on the left-hand side of the top panels.

That way we can emphasise the influence of the changing field gradients on the quasiprobability flow and still carry residual features from the previous evolution.

With the use of a time-dependent field come time-dependent separatrices. At the field crossing [Fig. 5.7(a)], the separatrix is equal to that of the field-free case. For both $R = 4$ a.u. and $R = 14$ a.u. the system is in the same configuration as the static field case, closed and open separatrices respectively. However, for $R = 6.8$ a.u., the system changes phase-space configurations from nested [Fig. 5.7(b′)] to open [Fig. 5.7(d′)] separatrices in a quarter cycle and spends roughly half of the time in each configuration.

The shift in momentum gate is again present, and follows the same clockwise cycle discussed in previous sections. The quasiprobability distribution flows via the positive momentum gate from the left to right potential well [see Fig. 5.7(a) and Fig. 5.7(c′)], and within the same quarter cycle follows the negative momentum gate [see Fig. 5.7(d) and Fig. 5.7(e′)] from the now downfield (right) to upfield (left) potential wells, seemingly opposing the direction of the field.

There are however key differences, with regard to the static-field case. Depending on the instantaneous phase-space configuration and on the interplay between the field gradient and the momentum gates, the time-dependence of the field may aid or hinder their clockwise motion and/or ionisation. For instance, in the first column of Fig. 5.7, the bound part of the Wigner function moves to the right [Fig. 5.7(a)], but is subsequently hindered by the field gradient to move back towards the left [Fig. 5.7(b) and (c)].

If the inter-nuclear distance is such that that the phase-space configuration changes from nested to open separatrices within half a field cycle, the dynamics are more complicated. A good example is provided in the middle panels of Fig. 5.7, for which there is initially a quantum bridge feeding directly into the tails on the left-hand side [Fig. 5.7(a′)]. When the field changes direction [Fig. 5.7(b′)], its gradient helps the clockwise motion towards the right. Nonetheless, because the separatrices are nested there will be population trapping, and, consequently an enhancement in the cyclic motion back to the left (upfield) centre, as shown in Fig. 5.7(c′). The Wigner function will only "spill" towards the continuum and form tails to the right when the separatrices open [Figs. 5.7(d′) to (f′)]. A remarkable feature in this optimal configuration is that population trapping only occurs when it actually should, i.e., at the times in which the quantum bridges are building up. As the peak-field times are approached, the separatrices open and ionisation bursts occur. However, they do not necessarily follow the field. For larger inter-nuclear distances (right column in Fig. 5.7), the separatrices are always open but the quantum bridges are rather weak. Therefore ionisation mainly occurs via the quasistatic pathway close to the equienergy curves.

The time evolution of such gates is better studied by looking at the autocorre-

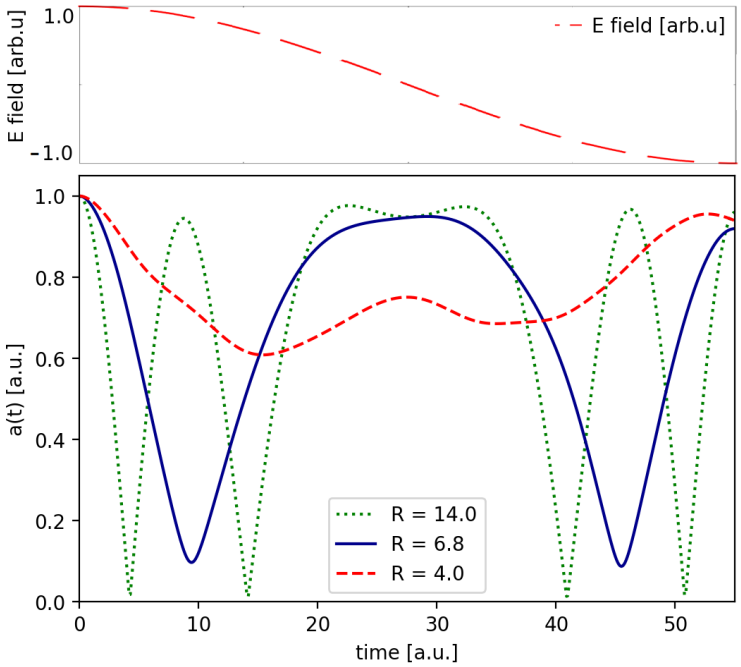

Figure 5.8: Absolute value of the auto-correlation function shown in the [lower panel] over a half-cycle of a monochromatic laser field given by Eq. (5.2.2) of wavelength $\lambda = 800$ nm and strength $E = 0.0534$ a.u. (intensity $I = 10^{14}\mathrm{W/cm}^2$). The starting wavepacket is delocalised in a model H_2^+ molecule with inter-nuclear distances of $R = 4$ a.u. (red dashed), $R = 6.8$ a.u. (blue) and $R = 14$ a.u. (green dotted). The time profile of the laser field is indicated by the dashed red line in the [upper panel] in arbitrary units.

lation function plotted in Fig. 5.8 over a half field cycle. Around the maximum and minimum of the laser field, the oscillations of the Wigner function are similar both in frequency and amplitude to those of the static case. Qualitatively, the situation is the same. However, around the field crossing the population has an additional shift, changing direction and following the laser field. It then continues its normal rhythm following the momentum gates around the field minimum. For example, for $R = 6.8$ a.u. the population escapes by the negative momentum gate up to around $t = 5$ a.u. or $t = T/16$, where T is the laser period and $T = 110.2$ a.u. (or $T = 2.7$ fs). The Wigner function then shifts to a positive momentum gate at $t = 10$ a.u. or $t = T/8$ (despite the laser field still being in the same direction) going back to its initial distribution. Then, at $t = 30$ a.u. or $t = T/4$, where the regular cycle of the Wigner function would create a strong negative momentum gate, the quantum bridge has near zero momentum [Fig 5.7(a′)] because the direction of the laser field has changed and now counters this movement (instead of adding to it). The autocorrelation function stays more or less constant instead of reaching the minimum associated with a negative momentum gate (see Fig 3.12 for comparison). The positive momentum gate before $t = 45$ a.u. or $t = 3T/8$, now following the direction of the laser field, leads the population away from its initial distribution [Fig 5.7(c′)]. Finally the negative momentum gate (now countering the laser field)

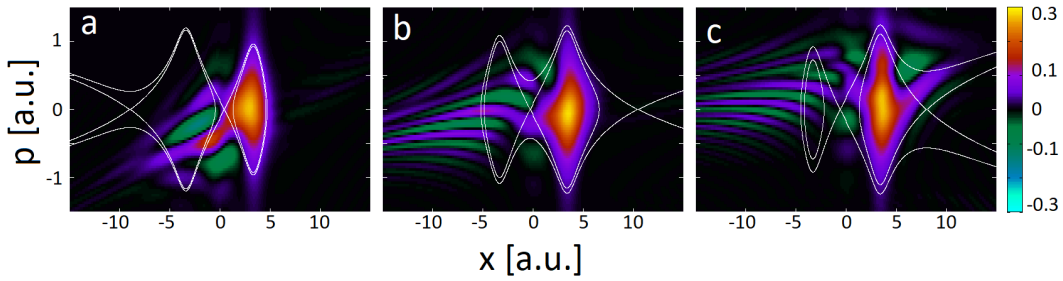

Figure 5.9: Wigner quasi probability distribution of a model H_2^+ molecule in a monochromatic laser field given by Eq. (5.2.2) of wavelength $\lambda = 800$nm and strength $E = 0.0534$ a.u. (intensity $I = 10^{14}\mathrm{W/cm}^2$) with inter-nuclear distance $R = 6.8$a.u. and a starting wave packet localised upfield at different instants of time: $t = 0.13T$ (a), $t = 0.33T$ (b), $t = 0.45T$ (c), where T is the laser period and $T = 110.2$ a.u. (or $T = 2.7$ fs).

shifts the population back to its initial position Fig 5.7(e′), and the autocorrelation function increases.

Finally, if the initial wave packet is localised upfield, i.e. $\Psi = \Psi_{\mathrm{up}}(x, 0)$, there are significant differences from the static case. This is shown in Fig. 5.9, for the optimal inter-nuclear distance of $R = 6.8$ a.u. During the initial quarter of a cycle,the quantum bridge builds up and directly feeds the ionisation tails [Fig. 5.9(a)]. After the field reaches a crossing and switches side, the wave packet will be located in the downhill (right) well. For the time intervals in which the separatrices are nested [Fig. 5.9(b)], population trapping will still help a quasiprobability transfer against the field gradient via the momentum gate. However, as the field peak is approached and the separatrices are no longer nested [Fig. 5.9(c)], this pathway will be strongly suppressed and quasi-static ionisation will prevail (see tails forming on the right-side of the figure). At the subsequent crossing the field will change its direction again, and the quantum bridge towards the left centre will rebuild. Hence, the stationary quantum bridges discussed in Chapter 3.2.2 are no longer an advantage. Within the timescale of a field cycle, the upfield wave packet does not become a cat state. Longer times will make the interpretation difficult, as, apart from ionisation, there will also be rescattering as an oscillatory field may drive the wave packet back to the core. This will leave imprints in the Wigner functions [151, 87].

5.3 Conclusion

Throughout this Chapter, the autocorrelation functions and Wigner quasiprobability distributions exhibit a periodic motion that can be precisely determined using the system's eigenfrequencies. These dynamics are strongly dependent on the width of the initial wavepacket, and the time-independent overlap integrals obtained for an eigenfunction basis has greatly facilitated those studies. In addition to that, the present phase-space studies support the conclusions from Chapter 3, that the

intra-center quasiprobability flows caused by quantum interference and forming a 'quantum bridge' have their time evolution determined by frequencies intrinsic to the system, instead of a non-adiabatic response to an external driving field as proposed in [76]. Moreover, for the specific, field-free case studied in section 5.1, we have determined such frequencies exactly for a hyperbolic double-well, thus going beyond the estimates in Chapter 3. This also sheds light on the behaviour observed for time dependent fields. The frequency of the quantum bridge being higher than that of the laser field, the quasiprobability distribution will sometimes counter-intuitively flow in the direction opposed to the electric-field gradient. The strength of this return is again dependent on the inter-nuclear distance. Remarkably, the frequencies obtained in the present work are within the range of those observed in [76], which is around four times that of a typical near-IR field ($\lambda \simeq 800$nm). We have also observed that the quasiprobability flow into the continuum occurs in well-defined temporal bursts, being strongest in the interval for which the separatrices open and there is no population trapping. A key qualitative difference between static and time-dependent fields is that, in the latter case, an initial wave packet localised upfield is no longer preferable to a delocalised (cat) state. This happens because initial upfield states foster the appearance of static quantum bridges, which will be suppressed for a whole quarter of a cycle when the wave packet is upfield. In contrast, initial delocalised states support cyclic bridges building up close to the central saddle, which may be synchronised to the external driving field. Finally, the fact that enhanced ionisation is an optimisation problem suggests that the ionisation mechanisms encountered and analysed in this Chapter can be controlled by appropriate coherent superpositions of states, targets and driving fields. This will be the focus of the following Chapter.

Chapter 6

Classification and control of enhanced ionisation with machine learning

Manipulating coherent superpositions of quantum states and nonclassical pathways has been a central question to many areas of science, such as coherent control [227, 228, 229] and quantum information [230]. Important applications include controlling chemical reactions [231] or electron dynamics in ultrafast molecular dissociation [232, 233, 234, 235], creating quantum switches [236, 237, 230] and enhancing nonclassicality in extended systems such as light-harvesting compounds [238, 239]. In this wide range of scenarios, decoherence must be kept at bay, so that the timescales of interest are much shorter than the decoherence times. This brings one's attention to how coherent superpositions of quantum states and nonclassical pathways may be controlled in attoscience. Previous analyses in Chapters 3 and 5 focused on understanding the physical mechanisms behind the quantum bridges, and were restricted to a homonuclear molecular potential in the field-free setting, or under a strong static or monochromatic laser field. The initial wavepacket was taken to be an upfield or downfield localised Gaussian, or a symmetric coherent superposition thereof known as a cat state [13]. Here, we focus on how the quantum bridges can be manipulated by using different relative phases and wavepacket localisations in the initial superposition state, molecular potentials of heteronuclear type, where each well is weighted asymmetrically, and electric field configurations. This is a complex task: with a wealth of tunable parameters, such as internuclear separation, relative phase and wavepacket localisation in the initial wave packet, differing nuclear charges, laser intensity and frequency as well as the pulse shape, it necessitates optimisation techniques. Machine learning methods have been explored in a wide range of scenarios in quantum physics (see the reviews [240, 241, 242] and the recent tutorial [243]) and ultrafast photonics [244]. Recently, they have been employed in the attosecond science context to control attosecond pulses [245], retrieve the structure

of a large molecule from laser-induced electron diffraction patterns [246], track quantum pathways within a spatio-temporal Feynman path integral framework [247] or retrieve the molecular internuclear distance from holographic interference patterns [248].

In this Chapter, we aim at controlling the pathways behind enhanced ionisation. We begin with an overview of the methods used throughout the whole Chapter in section 6.1, with a focus on the use of dimensionality reduction. Indeed we employ machine-learning techniques for dimensionality reduction, such as the T-Distributed Stochastic Neighbour Embedding (t-SNE) [217] and Principal-Component Analysis (PCA) [249] to find overall trends and patterns that allow us to establish a hierarchy of parameters and classify different regimes for strong-field ionisation. Following that, in section 6.2 we employ a model molecule in a static field to both extend the analysis of the effect of various parameters started in Chapters 3 and 5 and as a proof of concept of the t-SNE dimensionality reduction technique. In section 6.3, we apply the t-SNE on a time-dependent two-colour driving field, where the autocorrelation function exhibits several distinct behaviours in time, including a stepwise profile in which ionisation is switched on or off. Aided by a qualitative phase-space analysis, we also provide a physical interpretation for these features. We end this Chapter with a conclusion in section 6.4.

6.1 Method

6.1.1 System

We solve the TDSE following the method in section 2.2. The molecular binding potential is given by

$$V(x) = Z_{\mathrm{r}} V_{sc}(x - R/2) + Z_{\mathrm{l}} V_{sc}(x + R/2), \tag{6.1.1}$$

where R is the internuclear distance. The first and second term appearing on the right-hand side of equation (6.1.1) shall be called the right and left potential wells, respectively. The homonuclear case is recovered by setting $Z_{\mathrm{l}} = Z_{\mathrm{r}} = 1$. The symbol Z is chosen in reference to the nuclear charge; however, in this toy model, Z_i is allowed to be a continuous variable. The external laser field $\mathcal{E}(t)$ is either taken to be static, that is $\mathcal{E}(t) = E_0$, or a time-dependent linearly polarised polychromatic field such that

$$\mathcal{E}(t) = E_0 \left[\cos(\omega t) + r_t \cos(b\omega t + \phi)\right], \tag{6.1.2}$$

where b is the frequency ratio between the first and the second driving wave, r_t is the field-strength ratio, ϕ is the relative phase between the two driving waves, and ω is the frequency of the fundamental.

The initial wavefunction is approximated by coherent superpositions of Gaussians

wavepackets $\Psi_{\mathrm{l}}(x,0)$ and $\Psi_{\mathrm{r}}(x,0)$

$$\Psi_{\mathrm{l,r}}(x,0) = \langle x|\Psi(0)\rangle = \left(\frac{\gamma_{\mathrm{l,r}}}{\pi}\right)^{\frac{1}{4}} \exp\left\{-\frac{\gamma_{\mathrm{l,r}}}{2}(x-q_{\mathrm{l,r}})^2 + ip_0(x-q_{\mathrm{l,r}})\right\} \tag{6.1.3}$$

of width $\gamma_{\mathrm{l,r}}$, centred at vanishing initial momentum $p_0 = 0$ and initial coordinate $q_l = -R/2$ localised around the left well or $q_r = R/2$ localised around the right well.

We then introduce asymmetry between the initial left and right wavepackets. As such, the initial state including a relative phase $\theta \in [-\pi, \pi]$ and a localisation parameter $\alpha \in [0,1]$ is described by the generalised expression

$$\Psi_{\alpha,\theta}(x,0) \coloneqq \frac{\sqrt{\alpha}\Psi_{\mathrm{l}}(x,0) + \sqrt{1-\alpha}e^{i\theta}\Psi_{\mathrm{r}}(x,0)}{\sqrt{1+2\sqrt{\alpha(1-\alpha)}\cos(\theta)\mathcal{I}_o}}. \tag{6.1.4}$$

The constant of normalisation in the denominator depends on the initial state overlap $\mathcal{I}_0$:

$$\mathcal{I}_0 = \int \Psi_{\mathrm{l}}^*(x,0)\Psi_{\mathrm{r}}(x,0)\mathrm{d}x = 2 + 2\frac{\sqrt{2}(\gamma_{\mathrm{l}}\gamma_{\mathrm{r}})^{\frac{1}{4}}}{\sqrt{\gamma_{\mathrm{l}}+\gamma_{\mathrm{r}}}} e^{-\gamma_{\mathrm{l}}\gamma_{\mathrm{r}}(q_l-q_r)^2/(2(\gamma_{\mathrm{l}}+\gamma_{\mathrm{r}}))} \tag{6.1.5}$$

Note that $\Psi_{1,\theta}(x,0) = \Psi_{\mathrm{l}}(x,0)$ and $\Psi_{0,\theta}(x,0) = \Psi_{\mathrm{r}}(x,0)$ (up to a global phase), whilst intermediate values of α produce coherent superpositions of varying weight. If one considers $\Psi_{\frac{1}{2},0}(x,0)$ and $\Psi_{\frac{1}{2},\pi}(x,0)$, this will lead to even and odd cat states, see Eq.(3.1.4), for which the wavepacket localisation in each centre are equally weighted.

6.1.2 Time evolution characterisation

In order to understand the system dynamics through the use of dimensionality reduction methods, we wish to characterise the electronic dynamics by a single value. In section 6.2, we will employ the ionisation rate Γ from time $t = 0$ to $t = T$ quantified as Eq.(3.1.9) in Chapter 3. For the time-dependent case in section 6.3 we choose to quantify the shape of the autocorrelation function (2.2.5), as it carries more temporal information. A preliminary investigation showed that the autocorrelation function can take three distinct shapes (Figure 6.1): 'steps', 'constant', and 'other', which represent different behaviours.

The classification of autocorrelation functions into the defined categories is performed by a simple deterministic decision tree algorithm. First, we check whether a function is 'constant', that is, if it does not fall below a given threshold value. Next, we look for the steps. Steps are characterised by the intervals where the autocorrelation function stays approximately constant, followed by a steep decline. Hence, if we find a constant interval longer than some 'critical length', we categorise it as a 'step'. We define a constant interval as an interval where the difference of any two values is smaller than a critical threshold, 'ϵ'. If the function is not caught by

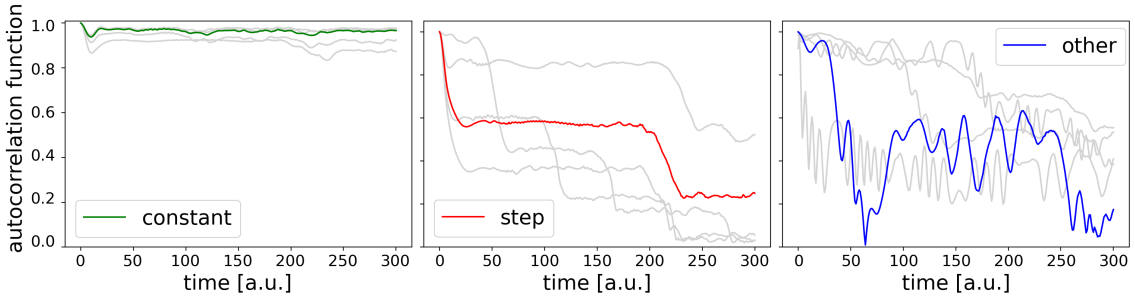

Figure 6.1: Examples of the three potential outputs of the autocorrelation function sorting algorithm. The parameters used vary greatly but are all within the range shown in Table. 6.1.

these checks, it is classified as 'other'. In the results presented in this Chapter the threshold value is set to 0.8, the critical length is set to 100, while the critical ϵ is 0.03. All of the autocorrelation function arrays used have 3000 elements.

6.1.3 Dimensionality reduction

The present problem depends on many parameters: The initial wavepacket localisation α, its widths γ_l and γ_r and relative phase θ; molecular parameters like the weights Z_l and Z_r and the inter-nuclear distance R; and many external electric-field parameters such as ϕ, r_t, b and E_0. The main challenge to overcome when studying the effect of a large number of parameters simultaneously is how to visualise the results. Indeed, each data point will exist in a high-dimensional space (the number of dimensions equal to the number of parameter used), and ideally we would like to project our results down to a two-dimensional space.

In order to understand and visualise the effect of various field and molecular parameters on the time evolution characteristic parameter, we will generate multi-dimensional data points and project them to two-dimensions using both the t-SNE and PCA projections described in Chapter 2.6.

While we will visualise our results using the t-SNE, we will have compared all projections to PCA. Indeed, t-SNE is stochastic, so each run can yield different results. It focuses on preserving the local structure of the data and is a non-linear technique. On the other hand, PCA is linear, deterministic, and preserves global properties while potentially losing low-variance deviations between neighbours. Therefore by comparing both projections we can guarantee the accuracy of the t-SNE results. The PCA projections are presented in the Appendix B.

To obtain a data point, $N-1$ parameters are randomly uniformly distributed within the range shown in Table. 6.1. The electronic wavefunction is then evolved using the TDSE (See Chapter 2.2) and we characterise the time evolution information by a single value as described in the above section. In the case of a static external field as studied in section 6.2 this is done by computing the ionisation rate Γ (Eq. (3.1.9)). For the time-dependent field in section 6.3 we quantify the shape

Static Field	α	θ	γ_r	γ_l	R	Z_r	Z_l	E_0
min	0.0	-π	0.2	0.2	3.0	1.0	1.0	0.04
max	1.0	π	1.0	1.0	12.0	2.0	2.0	0.08

Time-dependent Field	α	θ	γ_r	γ_l	R	Z_r	Z_l	E_0	b	r_t	ϕ
min	0.0	-π	0.2	0.2	4.0	1.0	1.0	0.04	0.5	0.0	-π
max	1.0	π	1.0	1.0	10.0	1.5	1.5	0.08	2.0	1.0	π

Table 6.1: Table of all parameters used throughout this chapter with the minimum and maximum value of the range they are randomly chosen from.

of the autocorrelation function (see section 6.1.2). The $N-1$ parameters chosen randomly as well as the single value characterising the time evolution form a data point of size N.

In certain situations specific data points are removed from the final data set in order to focus the visualisation on the matter at hand. For example in section 6.3.1, only 1332 data points are used from the 500 000 originally computed using random parameters. Indeed, in order to focus on the 'step' output of the autocorrelation function, approximately 99% of data points with outputs 'constant' and 99.95% of data points with output 'other' are removed.

The t-SNE is then used to reduce our N-dimensional data points to 2 dimensions, projecting the data set onto the two axis y_1 and y_2. Because the t-SNE is inherently nonlinear, it is not possible to reverse-transform its output to the original dataset. Therefore, these axes have no clear meaning with relation to the original dataset and they act solely as two dimensions in which the results are visualized. The data points will have clustered into different groups, the nature of which will be understood by plotting the projection as a function of one of the input parameters. This will allow us to determine which parameter or which combination of parameters influence the ionisation rate or the autocorrelation function step, and to what degree. The overall method described here and used throughout this chapter is summarised schematically in Fig. 6.2. Finally, the PCA method is used to ensure that the observed behaviour is neither a remnant of the stochastic nature of the algorithm, nor due to the removing of data points from the data set.

6.2 Static fields

We will start with an analysis of enhanced ionisation in static fields. While the ultimate goal of this chapter is to understand and control enhanced ionisation in time-dependent fields, the purpose of this static field section is two-fold:

- Obtain an in depth understanding of how certain parameters influence the system, and expand on the conclusions drawn in Chapters 3 and 5.

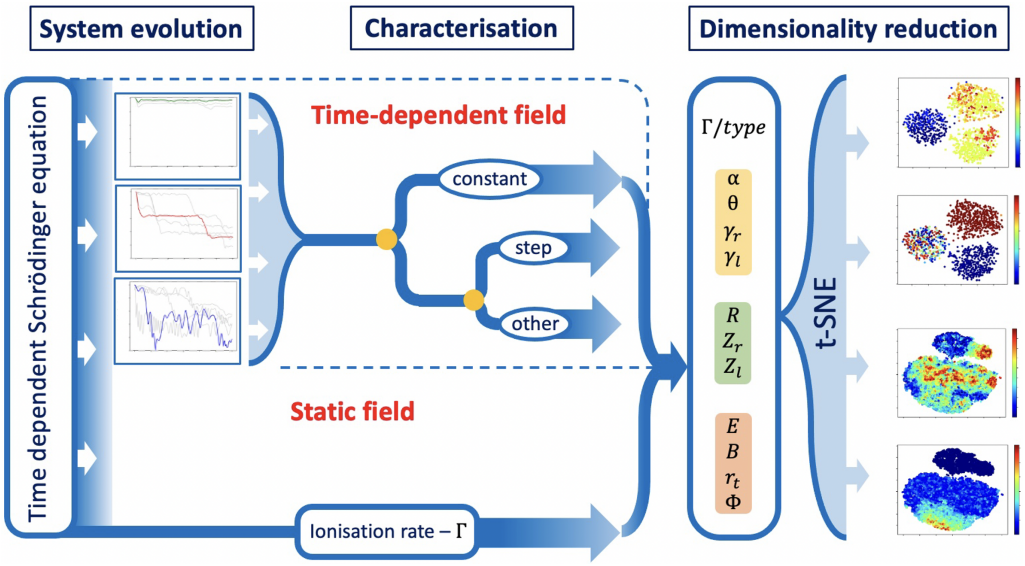

Figure 6.2: Schematic outline of the methodology used throughout this Chapter.

- Establish the effectiveness of the t-SNE dimensionality reduction technique as a method of simultaneous multi-parameter analysis. This will allow us to use it as a primary tool in section 6.3.

6.2.1 Qualitative analysis

As a starting point, we will perform a qualitative investigation of how specific parameters influence the quantum bridges and the ionisation rate in a static field using the generalised initial wavepacket given by Eq. (6.1.4). The static field in this chapter is chosen in such a way that the left well is located downfield and the right well upfield.

Initial electron wavepacket.

A conclusion from Chapter 3 was that a major predictor of enhanced ionisation is the localisation of the initial electron wavepacket. However, only three configurations were studied: localised around the right well, localised around the left well, and delocalised equally around both centres. Here we start with a more thorough analysis of this parameter by considering it a continuous variable, α, see Eq. (6.1.4). As shown in Fig. 6.3, the ionisation rate is linearly proportional to the electron localisation, with $\alpha = 0.0$ (initially localised upfield) leading to the highest ionisation rate. This can be understood as the downfield centre narrowing the effective-potential barrier for the upfield centre, hence enhancing upfield ionisation.

In addition to a continuous localisation parameter, the state of the initial electron wavepacket is varied by a relative phase factor θ, see Eq. (6.1.4), between the superposition of Ψ_r and Ψ_l. When using an equally delocalised wavepacket, $\alpha = 0.5$, the ionisation rate as a function of θ (in rad) peaks around $\theta = 2.4$ and is minimal for

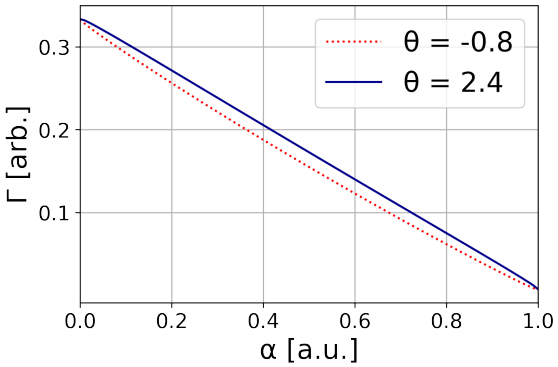

Figure 6.3: Ionisation rate Γ for an initial wave packet $\Psi_{\alpha,\theta}(x,0)$ with respect to the localisation parameter α, comparing maximum $\theta = 2.4$ and minimum $\theta = -0.8$. The external static field has strength $E_0 = 0.06$, and the molecular parameter used are internuclear distance $R = 7$, $Z_r = 1.0$ and $Z_l = 1.0$.

$\theta = -0.8$. This has little overall influence on the ionisation rate as seen in Fig. 6.3.

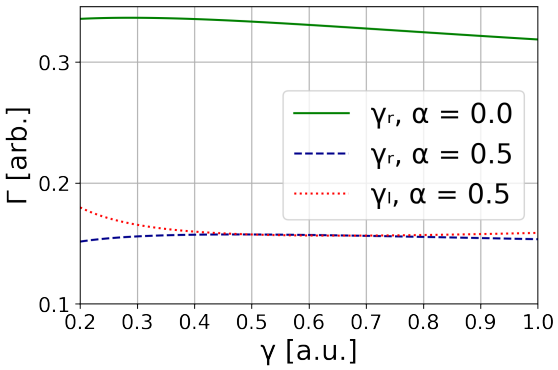

Figure 6.4: Ionisation rate Γ for an initial wave packet $\Psi_{0.5,0}(x,0)$ with respect to the wavepacket width γ, comparing the effect of γ_r (blue-dashed line) and γ_l (red-dotted line). Additionaly, the effect of the wavepacket width γ_r for an initially localised wavepacket $\Psi_{0,0}(x,0)$ is shown (green line). The external static field has strength $E_0 = 0.06$, and the molecular parameter used are internuclear distance $R = 7$, $Z_r = 1.0$ and $Z_l = 1.0$.

Finally, the initial wavepacket widths γ_r and γ_l, see Eq. (6.1.4), are set to differ from $\gamma = 0.5$, which is the minimal ground-state energy of a field free single-centre soft-core potential with softening parameter $a = 1.0$. The result of this change is shown in Fig. 6.4 with both an initially localised upfield wavepacket ($\alpha = 0.0$) and an initially delocalised wavepacket ($\alpha = 0.5$). This has no major influence on the ionisation rate. A slight increase in the ionisation rate is present when the downfield wavepacket width γ_l decreases below $\gamma_l = 0.5$ when $\alpha = 0.5$. For an initially localised upfield wavepacket ($\alpha = 0.0$), increasing the wavepacket width above $\gamma_r = 0.5$ slightly decreases the ionisation rate.

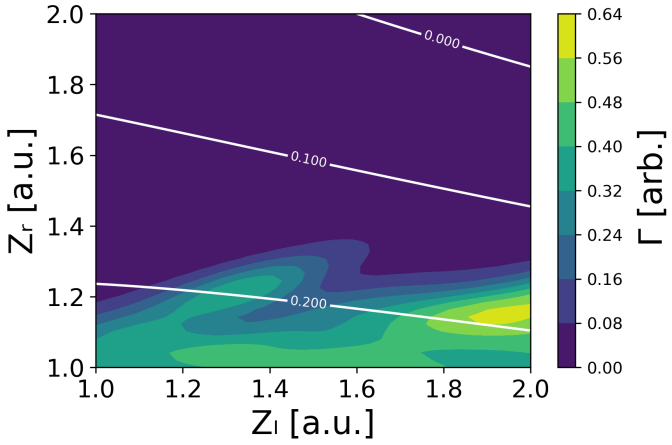

Figure 6.5: Contour plot of the ionisation rate Γ as a function of Z_l and Z_r using an external static field $E_0 = 0.06$ with internuclear distance $R = 7$. The white lines indicate the separatrix energy difference ΔE, with the 0.0 line indicating the transition from open separatrices ($\Delta E > 0$) to closed separatrices ($\Delta E < 0$).

Heteronuclear molecule $Z_{l,r}$

Finally, we expand our study to include heteronuclear molecules. We analyse the ionisation rate while varying the value of molecular weights Z_r and Z_l, of Eq. 6.1.1. The study of heteronuclear molecules is motivated by the enabling of a change in the critical internuclear distance and in the dynamics of the quantum bridges. Fig. 6.5 shows the ionisation rate as a function of both charges Z_r and Z_l simultaneously. There, a large region of suppressed ionisation is observed when $Z_r > 1.3$. The effect of Z_l is a lot less pronounced, leading to high ionisation rates even at $Z_l = 2.0$. While open separatrices do not guarantee a high ionisation rate, closed separatrices always suppress ionisation. To have a better understanding of the sharp decrease in ionisation rate with respect to Z_r, we look at the Wigner quasi-probability distribution in Fig. 6.6. Comparing the bound region around the right molecular centre in (a) and (b), as Z_r increases, the right molecular well deepens greatly. This leads the upfield population to stay trapped and greatly suppresses ionisation. On the other hand, the increase of the left bound region in (c) due to an increase in Z_l does not greatly influence the ionisation rate. This is because in enhanced ionisation the majority of the ionised population comes from the upfield centre, as shown in Chapter 3. There is very little change to the upfield (right-hand-side here) centre when increasing Z_l.

Now, a more complete overview would go through the effect of Z_l and Z_r with respect to various parameters, which would be slow and exhaustive. Instead we propose in the following section to use the t-SNE to analyse the effect of multiple parameters at once.

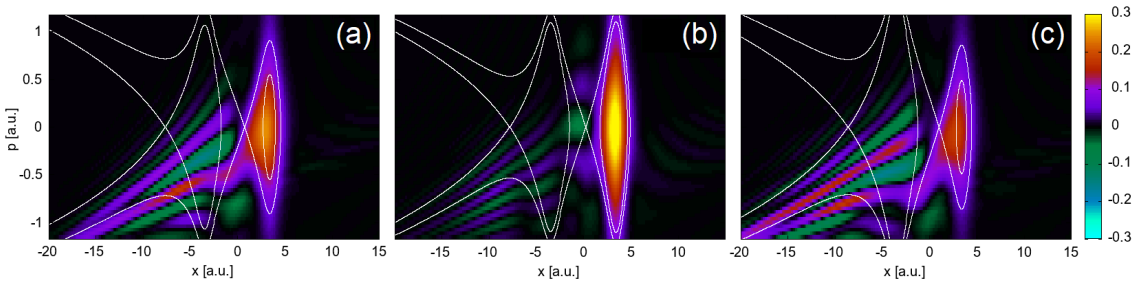

Figure 6.6: Wigner quasi-probability distribution of the ionisation from a static field $E_0 = 0.06$ with internuclear distance $R = 7$ for (a) $Z_r = 1.0$ and $Z_l = 1.0$, (b) $Z_r = 1.5$ and $Z_l = 1.0$ and (c) $Z_r = 1.0$ and $Z_l = 1.5$. The snapshots are taken at $t = 25$ a.u..

6.2.2 Proof of concept - machine learning techniques

We now aim to study the effect of multiple parameters on the ionisation rate, starting with a limited number in order to fully understand the results and to focus on the effect of the chosen parameters. Those are the internuclear distance R, the width of the initial superposed gaussian upfield and downfield wavepackets γ_l and γ_r, the phase difference θ between them, and the localisation parameter of the wavepacket α. The value of these parameters is chosen from a predetermined range described in section 6.1.

Data points comprised of these five parameters as well as the ionisation rate are projected onto two axis y_1 and y_2 using the t-SNE algorithm, shown in Figure 6.7. We see that the projected data bring into focus the connection between the ionisation rate, the internuclear distance and the electron localisation. These match the results from Chapter 3 and section 6.2.1. That is, peak ionisation yield is present at and around the peak internuclear distance of $R = 6.8$ a.u., shown in Figure 6.7(b), and when the initial wavepacket is localised upfield, shown in Figure 6.7(c). The low ionisation rate regions, seen in Figure 6.7(a), split into two distinct parts seen in Fig. 6.7(b) which correspond respectively to regions of too low and too high internuclear distance, studied in depth in Chapter 3. The ionisation rate falls linearly as the electron localisation changes from localised upfield to localised downfield, as seen in Fig. 6.3. The effect of the gaussian widths γ and the phase difference θ is a lot weaker as seen by the patterns in Fig. 6.7(d)(e)(f).

We will now look at the full range of parameters. In addition to the previous six, these following results will include the effects of the nuclear weight number Z_r and Z_l, and the electric field strength E_0. Because of these additional parameters, we posit that there is no longer a clear internuclear distance peak, but instead a larger range of optimal internuclear distances, dependent on E_0, Z_r and Z_l. For that reason the difference in energy between the central and Stark separatrix ΔE will also be analysed, but will not be an input parameter.

As seen in Figure 6.8(a), the algorithm successfully separates two clusters of low

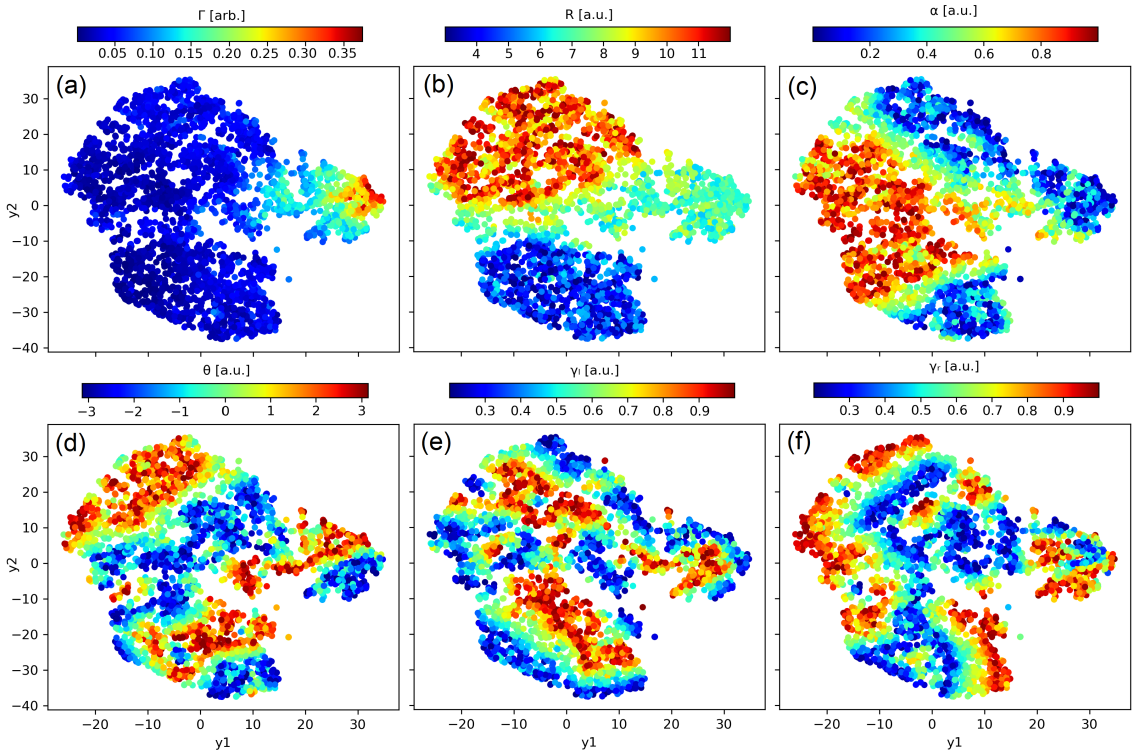

Figure 6.7: Plot of the 3000 6-dimensional data points that have been projected onto two axis y_1 and y_2 using the t-SNE dimensional reduction technique described in section 2.6. Each subplot has the projected data plotted as a function of an initial input parameter. The initial input parameters include (a) the ionisation rate Γ (given in arbitrary units), (b) the internuclear distance R, (c) the electron localisation α, (d) the phase difference between the left and right initial wavepackets θ, (e) the wavepacket width γ_l and (f) the right wavepacket width γ_r. The external field is taken to be static with $E_0 = 0.0534$ and the molecular weights $Z_r = 1.0$ and $Z_l = 1.0$, matching the results from Chapters 3.

($\Gamma < 0.002$) and high ($\Gamma > 0.05$) ionisation yield. Within the high ionisation cluster, the data points are further distinguished by a very high ($\Gamma > 0.3$) ionisation yield region. From the distribution of other parameters in these two clusters, we can determine which one leads to a high ionisation yield.

The strongest predictor of high ionisation rate is the nuclear depth factor Z_r, [see Fig. 6.8(b)], which in this configuration is associated to the upfield molecular well. As shown in Figure 6.5, the ionisation rate falls of sharply as soon as $Z_r > 1.0$. While the value of Z_r is originally chosen randomly in the range [1:2], the average value of Z_r in the high ionisation yield cluster is 1.16, and 1.12 in the $\Gamma > 0.3$ region. Indeed, 90% of the $\Gamma > 0.3$ ionisation yield data points have $Z_r < 1.25$.

In Fig. 6.8(c), echoing the conclusions from Fig. 6.7 and Fig. 6.3, only 4% of the high ionisation yield data points have the initial wavepacket of the electron localised downfield, with $\alpha > 0.8$. Similarly, 30% of the high ionisation yield cluster data points are for an initial wavepacket localised upfield, with $\alpha < 0.2$. This proportion goes up to 72% for $\Gamma > 0.3$.

From Fig. 6.8(d), the median initial field strength E_0 of the high ionisation yield cluster is 0.07, despite the parameter being originally randomly chosen from a [0.04:0.08] range. This means the majority of high ionisation yield data points have a high field strength. Indeed, 82% of data points have $E_0 > 0.06$ a.u. in that cluster and 88% in the $\Gamma > 0.3$ region.

As hypothesised earlier, the clear internuclear distance peak from Fig. 6.7 is now less pronounced in Fig. 6.8 (e) as we are now also varying the molecular weights Z and the field amplitude E_0. Still, 72% of data points within the very high, $\Gamma > 0.3$, ionisation yield region have internuclear distances R in the range $6 < R < 9$. This is surprising as the initial range for R is randomly taken from [3:12]. Therefore, one would expect that one third of the data points would be in this range.

Finally, in Figure 6.8(f), we can deduce the effect of the separatrices on the ionisation yield. Indeed if the separatrices are nested (see Fig. 3.1), meaning that $E_S > E_C$, or $\Delta E < 0$, then the ionisation rate is suppressed. In contrast, 99.5% data points in the high ionisation yield cluster have $\Delta E > -0.5$, and 86% of them have $\Delta E > 0$. This separation is present despite ΔE not being used as an input parameter.

In conclusion, the t-SNE enables us to visualise the effect of multiple parameters simultaneously. All the conclusions drawn in section 6.2.1 are visualised in Fig. 6.8. Parameters with little to no effect are swiftly identified and separated from relevant parameters. Not only that, but a hierarchy of the effect of different parameters is also established much more rapidly. For example the effect of Z_l on the ionisation rate being greater than that of α. Because of this we will be able to use the t-SNE in the following section to rapidly assert what parameters are relevant and to what degree.

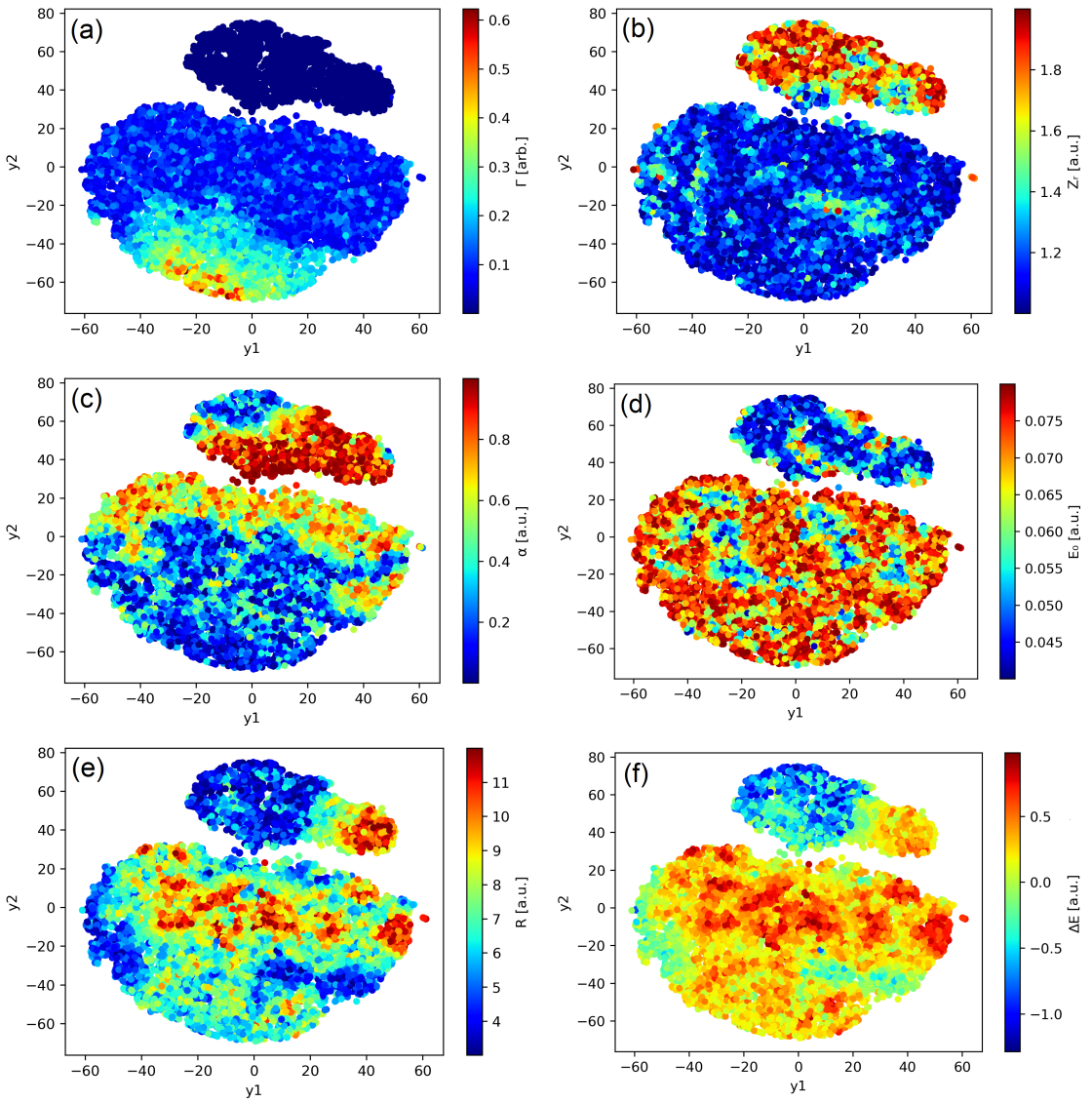

Figure 6.8: Plot of the 16 995 9-dimensional data points that have been projected onto two axis y_1 and y_2 using the t-SNE dimensional reduction technique described in section 2.6. Each subplot has the projected data plotted as a function an initial input parameter. The initial input parameters include (a) the ionisation rate Γ, (b) the right molecular well depth Z_r, (c) the electron localisation α, (d) the field strength E_0, (e) the internuclear distance R. Also included but not shown here are the left molecular well depth Z_l, the left initial wavepacket width γ_l, the right wavepacket width γ_r and the phase difference between the left and right initial wavepackets θ. In subplot (f) the separatrix energy difference ΔE is shown for each data point, however it is not one of the input parameters. The input data set has been reduced from 100 000 data points to only have either $\Gamma < 0.002$ or $\Gamma > 0.05$. PCA distributions using the original 100 000 data points are shown in Appendix B.

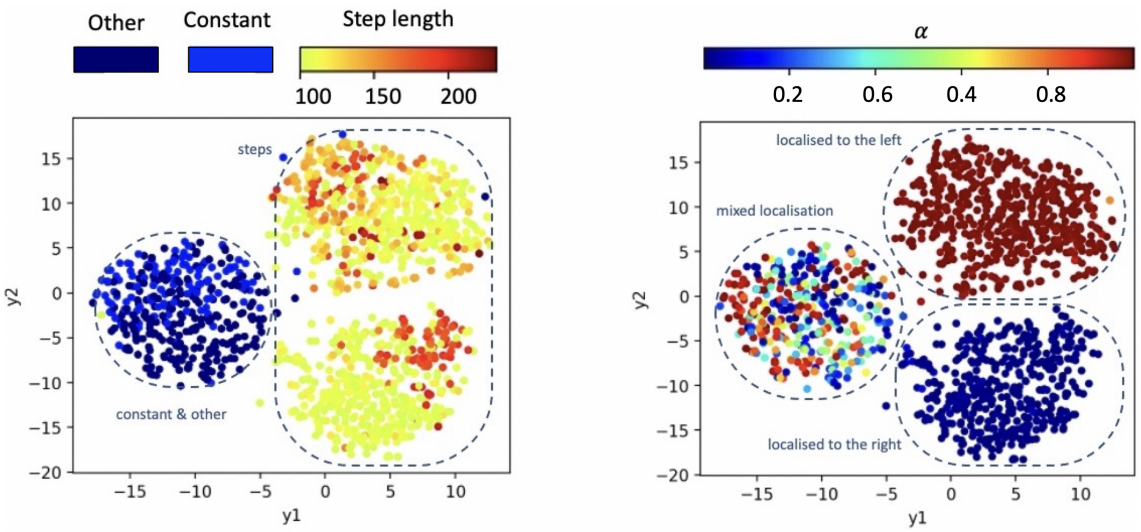

Figure 6.9: Plot of the 1332 12-dimensional data points that have been projected onto two axis y_1 and y_2 using the t-SNE dimensionality reduction technique described in section 2.6. Each subplot has the projected data plotted as a function of an initial input parameter (shown by the colour bar). All units are in [a.u.]. unless stated otherwise. The input parameters shown in this figure are (a) The step function shape obtained by the sorting algorithm in section 6.1.2 that outputs 'constant', 'other', or the length of the step in the autocorrelation function and (b) The initial electron wavepacket localisation represented by the parameter α in Eq. (6.1.4). The full list of input parameters as well as details on the initial data set used can be found in section 6.1. PCA distributions using 500 000 data points are shown in Appendix B.

6.3 Time dependent fields - optimising autocorrelation step functions

As seen in Chapter 5, when using a time-dependent field, the interplay between the frequency of the quantum bridge and the external field leads to quite complex structures. When using a polychromatic field (see Eq. 6.1.2) and specific parameters, we can obtain a 'controlled' ionisation release, which translates to a step function in the autocorrelation function plot. In the following section we will be looking at what parameters lead to step functions and why specific configurations lead to a controlled ionisation release.

6.3.1 t-SNE application to step functions

The 3 clusters and electron localisation

The t-SNE algorithm separates the data into three different clusters, whose nature can be seen in the two plots of Fig. 6.9. Therein, the data points are coloured with respect to (a) their autocorrelation function type and (b) their initial electron localisation α. Indeed, one cluster groups all autocorrelation functions classified as 'constant' or 'other', while the other two contain the autocorrelation functions

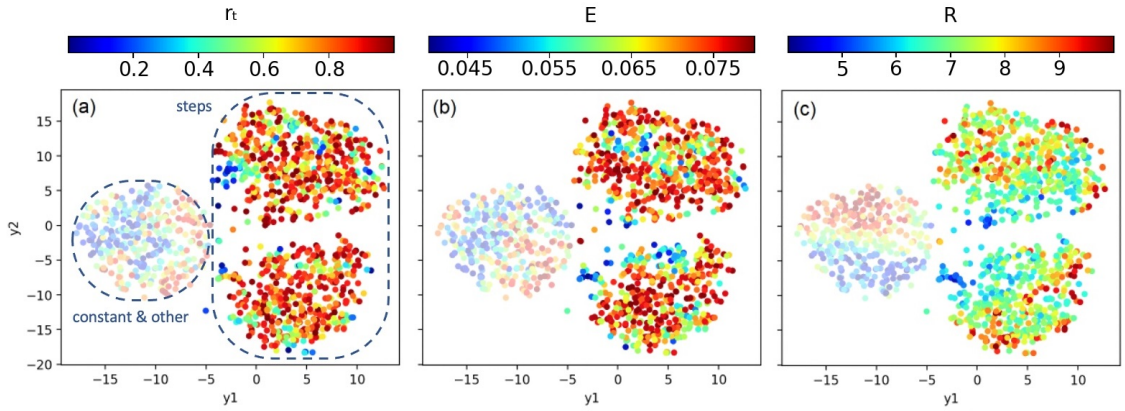

Figure 6.10: Plot of the 1332 12-dimensional data points that have been projected onto two axis y_1 and y_2 using the t-SNE dimensional reduction technique described in section 2.6. Each subplot has the projected data plotted as a function an initial input parameter (shown by the colour bar). All units are in [a.u.]. unless stated otherwise. The input parameter shown in this figure are (a) The ratio r_t between the two colour field amplitudes, (b) the overall field amplitude E_0 in Eq. (6.1.2) and (c) the internuclear distance R. The full list of input parameters as well as details on the initial data points used can be found in section 6.1.

classified as 'steps'. Those two clusters are understood by looking at the distribution with respect to the initial electron localisation. All autocorrelation functions that are classified as 'steps' have their initial electron wavepacket localised completely at one centre. The clusters are separated between having the initial electron wavepacket localised at the left centre ($\alpha > 0.95$, or dark red) and localised at the right centre ($\alpha < 0.05$, or dark blue). From this it is clear that the initial wavepacket must be localised either to the left or to the right for there to be steps. This is explained when looking at Fig. 6.14, in section 6.3.2.

Difference between the two 'step' clusters and the 'other' and 'constant' cluster

From looking at the different clusters, we can find other correlations, shown in Fig. 6.10, between certain parameters and the presence of step functions, most notably, the field ratio r_t between the two driving waves, in subplot (a). Indeed, while originally the value of r_t is chosen randomly from a range [0:1], the two step clusters have a median r_t value of 0.81 and an average of 0.75. Moreover, longer step lengths (more than 150 a.u., or orange/red) have a r_t median value of 0.85 and an average of 0.8.

Next, the overall electric field strength E_0, chosen at random from a range of [0.04:0.08], has an median and average value of $E_0 = 0.07$ a.u.. These can be understood by seeing that both a high field ratio r_t and a high field strength E_0 lead to a higher field peak during which more of the population will escape, causing a deeper drop in the autocorrelation function.

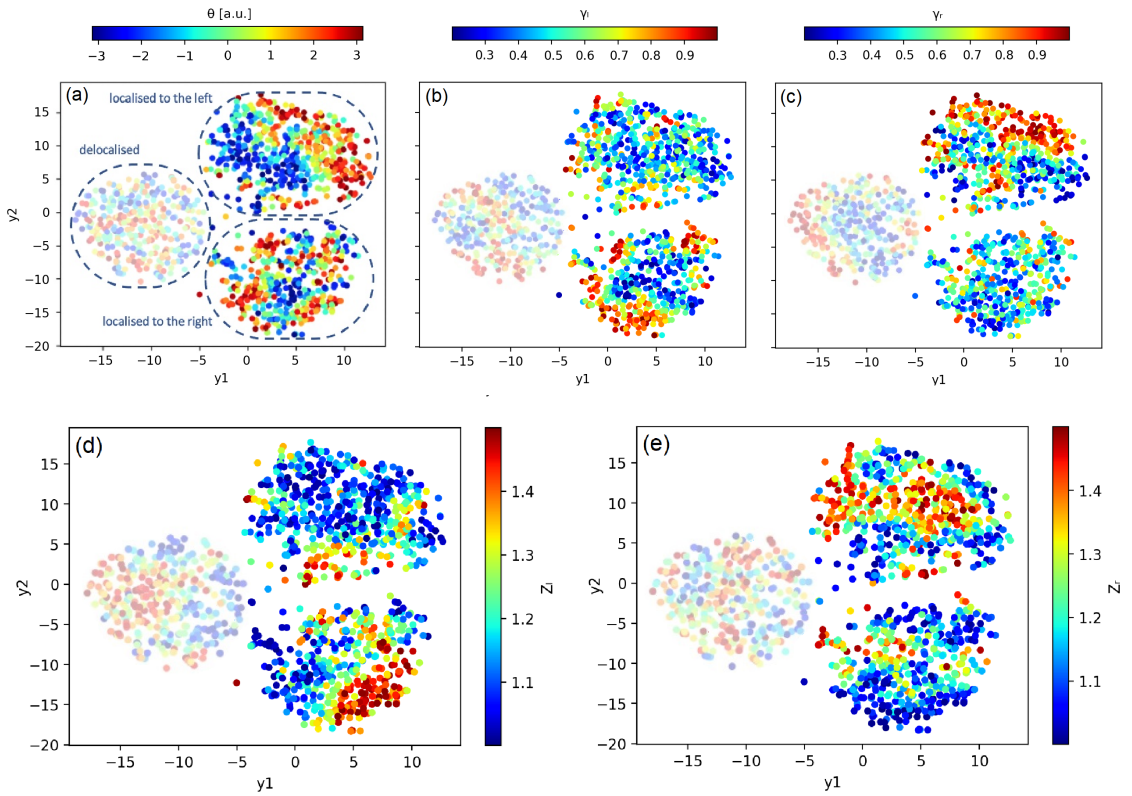

Figure 6.11: Plot of the 1332 12-dimensional data points that have been projected onto two axis y_1 and y_2 using the t-SNE dimensionality reduction technique described in section 2.6. Each subplot has the projected data plotted as a function an initial input parameter (shown by the colour bar). All units are in [a.u.]. unless stated otherwise. The input parameters shown in this figure are (a) the phase difference between the left and right initial wavepackets θ, (b) the left initial wavepacket width γ_l, (c) the right wavepacket width γ_r, (d) the left molecular well depth Z_l and (e) the right molecular well depth Z_r. The full list of input parameters as well as details on the initial data points used can be found in section 6.1.

Finally, the internuclear distance is clearly closer to the peak internuclear distance of $R = 7$ a.u., which is also confirmed by the standard deviation being only 1.05 instead of 1.3. R is also for 92.6% of all data in the step clusters above a minimum internuclear distance of $R = 6$ a.u.. The cause of this effect is more complex, and is discussed in detail in section 6.3.2.

Symmetry between the 'localised to the left' and 'localised to the right' step clusters

The value of α is not the only difference between the two step clusters. The next series of parameters, shown in Fig. 6.11, are connected to the symmetry between the left and right molecular wells. First, there is quite naturally the distribution of γ_l and γ_r. From their definition in Eq. (6.1.4), γ_l only influences the initial wavepacket localised to the left. Therefore, if the initial wavepacket was localised to the left, only the initial left wavepacket width γ_l is a relevant parameter, and vice versa. Since, as shown in Fig. 6.9, both step clusters use initially localised wavepackets exclusively,

only one γ parameter influences each cluster and the θ parameter (subplot (a)) has no effect on them. As seen in Fig. 6.11 (b) and (c), 22.8% of γ_l in the localised right step cluster are above 0.8, but only 6.8% are above 0.8 in the localised left step cluster. Similarly, 27.5% of γ_r in the localised left step cluster are above 0.8, while 5.3% are above 0.8 in the localised right step cluster. The width $\gamma = 0.5$ corresponds to the minimal ground-state energy of a field free single-centre soft-core potential with our current parameters, and the vast majority of step functions have a γ value that is within the range $[0.2 : 0.8]$. As γ deviates from 0.5, part of the initial wavepacket bleeds out of the bound region despite being initially localised. This leads to oscillations during the flat 'step' portion of the autocorrelation function and explains the absence of initial wavepacket widths γ above 0.8 in the step clusters.

The other set of parameters symmetric with respect to the left/right direction are the molecular weights Z_l and Z_r. Their effect on one cluster should be mirrored on the other. From Figs. 6.11(d) and (e), while there is no clear connection between the localised left cluster and Z_r, Z_l is more likely to be close to 1.0 (and vice-versa). Indeed there are 42% of data points that have $Z_l < 1.2$ in the localised right cluster, but 70% in the localised left cluster. Similarly, 39% of data points have $Z_r < 1.2$ in the localised left cluster, but 67% in the localised right cluster. This is further investigated in section 6.3.2.

Link between different parameters and the step length

Going back to the distribution with respect to the autocorrelation function type in Fig. 6.9, those two 'step' clusters are then also distinguished into regions of 'short' (less than 150 a.u., or lime yellow) and 'long' (more than 150 a.u., or orange/red) step length. From Fig. 6.12, we can already glean that the field-frequency ratio b affects the step length. However, there is no clear link with the field offset ϕ. This is further expanded upon in section 6.3.2.

6.3.2 Analysis of step functions

In order to obtain a controlled burst of ionisation, two pre-requisites are needed: First, a time interval in which the population stays bounded, and, second, a short burst of enhanced ionisation. Following the conclusions drawn from section 6.3.1, we already know what parameter range is required or preferred. In this section, we will provide an intuitive, physics-based analysis for the controlled-ionisation burst conditions.

Electron localisation

From Fig. 6.9, it is clear that the initial electron wavepacket must be localised, either around the left or right molecular well. Fig. 6.13 illustrates the difference between

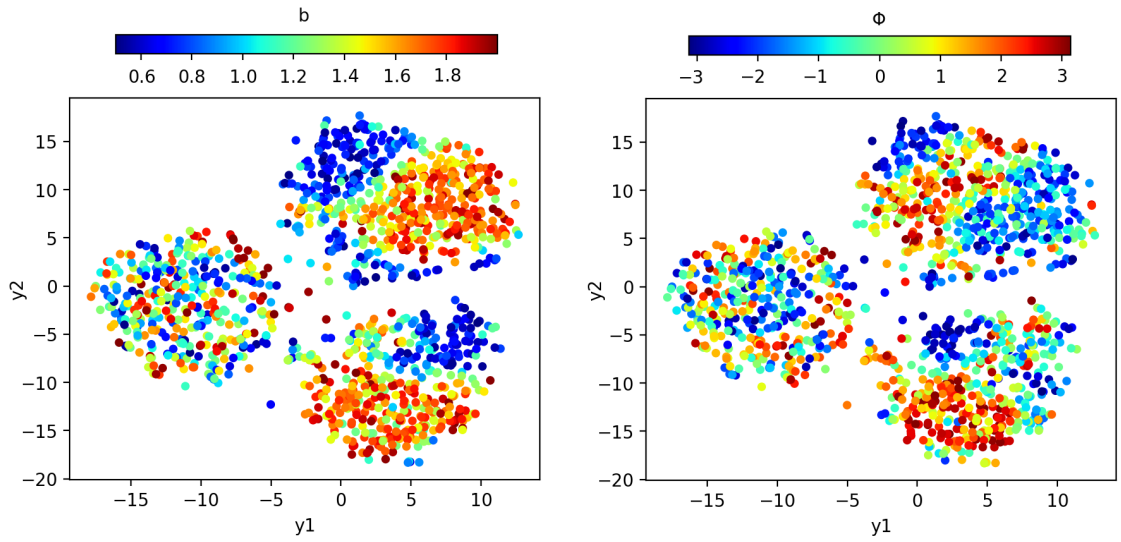

Figure 6.12: Plot of the 1332 12-dimensional data points that have been projected onto two axis y_1 and y_2 using the t-SNE dimensionality reduction technique described in section 2.6. Each subplot has the projected data plotted as a function of an initial input parameter (shown by the colour bar). All units are in [a.u.] unless stated otherwise. The input parameters shown in this figure are (a) The field-frequency ratio b and (b) the field offset ϕ in Eq. (6.1.2). The full list of input parameters as well as details on the initial data points used can be found in section 6.1.

using an initial localised wavepacket and a delocalised wavepacket. This, along with the Wigner function shown in Fig. 6.14, allows us to understand the mechanism behind the controlled ionisation release.

To obtain a burst of enhanced ionisation, the system must be in an optimal configuration. This was initially found in a study using static fields in Chapter 3, and further expanded upon in section 6.2. A key point is that the initial wavepacket must be localised upfield. This allows the population to escape directly through the quantum bridge to the semiclassical escape pathway and ultimately the continuum. It also stops the quantum bridge from cycling through the momentum space and bringing the population back to the upfield centre. Similarly, the population must stay bounded for an interval of time, meaning that the system must be in the configuration with lowest ionisation rate. As seen in Fig. 6.3, for static fields, this happens when the initial wavepacket is localised downfield. For the time dependent polychromatic field, the terms 'upfield' and 'downfield' become relative as the configuration changes with the direction of the field. However, in either case the initial wavepacket must be localised on one of the molecular centres. As seen in the behaviour of the Wigner function in Fig. 6.14 [right column] these two conditions are not possible if the initial wavepacket is delocalised. As seen in Chapter 3, because of the quantum interference between the two molecular centres, there is always the cyclic motion of the quantum bridge.

The localisation of the wavepacket must work in conjunction with the sign of

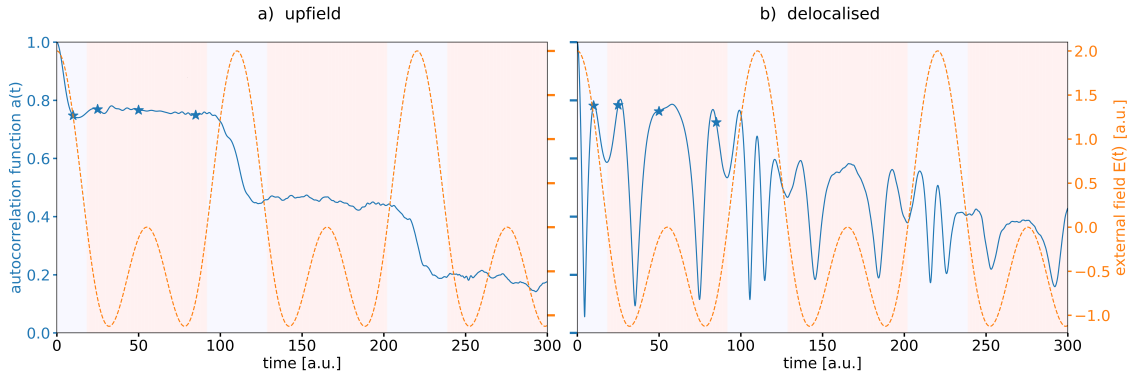

Figure 6.13: Comparison of auto-correlation functions at R = 6.8 a.u. with initial wavepacket localised upfield or delocalised. Direction of the field is denoted by the colour of the background, blue regions are positive values, pink are negative. The field is shown as the orange dashed lines with values shown on the rightmost y-axis and has form $\mathcal{E} \propto \cos\omega t + \cos 2\omega t$ where $\omega = 0.057$ a.u. The stars denote autocorrelation function values at times $t = 10$ a.u., $t = 25$ a.u., $t = 50$ a.u., and $t = 85$ a.u..

the external field for the stepwise behaviour to be present in the autocorrelation function. If the wavepacket is localised to the left and the external field $\mathcal{E}(t)$ is positive, or if the wavepacket is localised to the right and $\mathcal{E}(t)$ is negative, this will result in downfield localisation. Alternatively, upfield localisation occurs for a wavepacket localised to the left and negative $\mathcal{E}(t)$, or a wavepacket localised to the right and positive $\mathcal{E}(t)$.

In order to obtain a step function, the localisation must be upfield during the drop and downfield during the flat part of the step. In Fig. 6.13, the different field signs are shown by the different coloured shaded areas. Indeed, during the initial drop, the external field is positive and the population localised to the right, and therefore upfield. It escapes rapidly through the quantum bridge as seen by the Wigner function in Fig. 6.14(a) and the separatrices are open. As soon as the field changes sign, the approximately constant behaviour in the autocorrelation function begins. As seen in Figs. 6.14(b), (c) and (d), during that time the wavepacket localisation is now downfield. Because of that, despite the separatrices being sometimes open, like in subplots (b) and (d), ionisation is suppressed. When the field is no longer strongly negative around $t = 60$, the separatrices are closed, as shown in subplot (c). This also stops the population from escaping. The autocorrelation function therefore has a step until the field becomes positive again, with the separatrices strongly open. From this analysis and the clustering obtained by the t-SNE distribution, it is clear the electron localisation is the most important parameter in obtaining a controlled ionisation release.

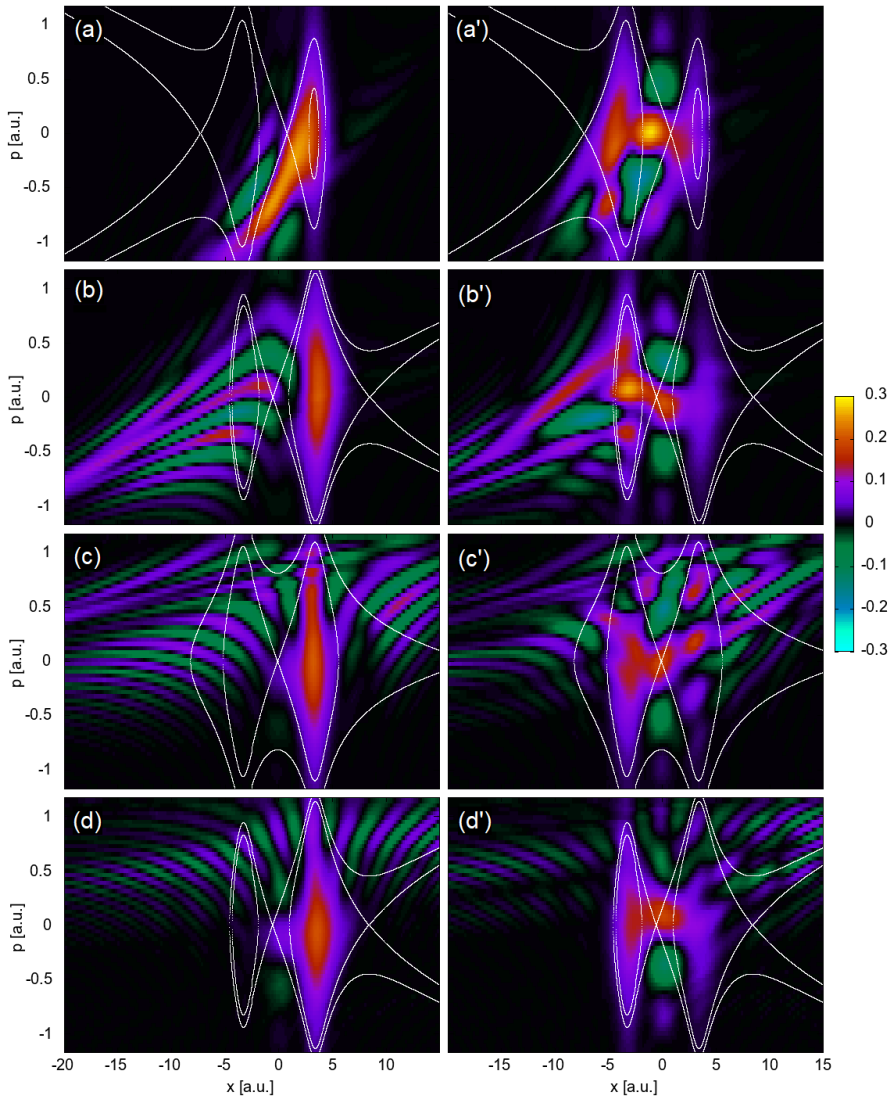

Figure 6.14: Wigner quasiprobability distributions computed for internuclear distances R = 6.8 a.u. with initial wavepacket localised at the right potential well ($\alpha = 0.0$) [left column] or delocalised between the two molecular wells ($\alpha = 0.5$)[right column]. The external field has frequency $\omega = 0.057$ a.u. and strength $E_0 = 0.0534$ a.u.. The snap shots are taken at times $t = 10$ a.u. for (a) and (a'), $t = 25$ a.u. for (b) and (b'), $t = 50$ a.u. for (c) and (c'), and $t = 85$ a.u. for (d) and (d'). These times are indicated by stars in Fig. 6.13.

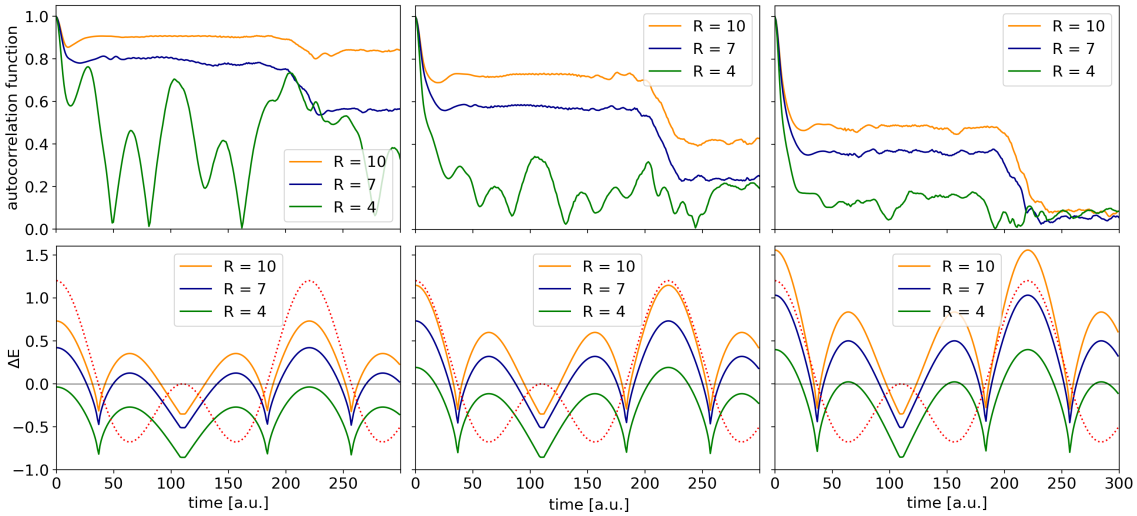

Figure 6.15: Different plots of autocorrelation functions [Top row] and ΔE [Bottom row] for $R = 4$ a.u., $R = 7$ a.u. and $R = 10$ a.u. with [Left column] $E_0 = 0.04$ a.u., [Middle column] $E_0 = 0.06$ a.u. and [Right column] $E_0 = 0.08$ a.u.. The external laser field is represented by the red dotted line (not to scale). We consider an initial wavepacket localised to the right, with $\gamma_r = 0.5$, and equal molecular weights $Z_r = Z_l = 1.0$. The external field amplitude and frequency ratios are $r_t = 1.0$ and $b = 0.5$, respectively.

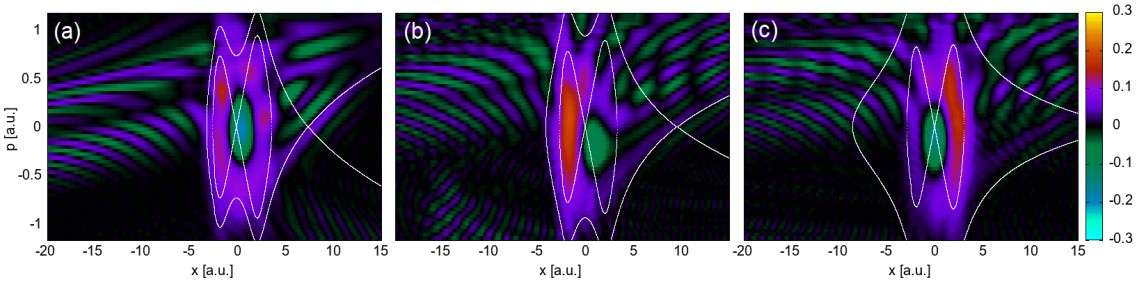

Figure 6.16: Evolution of the Wigner function with internuclear distance $R = 4$ a.u. and external field parameters $r_t = 1.0$, $b = 0.5$ and $E_0 = 0.04$ a.u.. The snap shots are taken at times (a) $t = 65$ a.u., (b) $t = 85$ a.u. and (c) $t = 100$ a.u.. Initial wavepacket localised to the right, with $\gamma_r = 0.5$. Molecular weights $Z_r = Z_l = 1.0$.

Separatrices

On top of the electron localisation, the presence of step functions is strongly dependent on the value of E_0, r_t and R, as seen in Fig. 6.10 and Fig. 6.11. Both E_0 and r_t have a similar effect on the external laser field: when r_t is close to 1.0 and when E_0 is large, the field peak increases in absolute value. As shown in Fig. 6.8, when using a static field, increasing E_0 leads to higher ionisation yield. In our time-dependent case, when E_0 or r_t is high, the value of ΔE at the field peak is much higher, meaning the separatrices are wide open. This phenomenon is best seen in Fig. 6.15 for a fixed value of R. In the second row it is clear that the increase in E_0 leads to higher maximum values of ΔE. For example, at internuclear distance $R = 10$, $E_0 = 0.04$ has $\Delta E = 0.7$ at the field maximum, while $E_0 = 0.08$ has $\Delta E = 1.6$. Compared to the corresponding autocorrelation functions in the first row, we see that when matched by the correct electron localisation, this will lead to a much steeper drop during the decreasing part of the autocorrelation function step. Using our previous example, at $E_0 = 0.04$ the first step plateaus at 0.9, while $E_0 = 0.08$ at 0.5.

The effect of the internuclear distance R is at a glance not clear. When focusing on the initial drop, the connection between ΔE and the initial drop of the correlation seem contradictory. Intuitively one would expect that a higher maximum ΔE lead to a steeper drop of the autocorrelation function, as was the case for varying r_t and E_0. But the opposite appears true with varying R. This is understood by the results in Chapter 3, and illustrated in Fig. 6.15. As R becomes too large, the quantum bridge between the two molecular wells weakens and the ionisation rate falls. In consequence the initial drop of the autocorrelation function is low. With E_0 being low as well, this leads to a 'constant' autocorrelation function as seen in Fig. 6.15 for $R = 10$ and $E = 0.04$. When R is too small, the quantum bridges between the molecular wells are at their strongest, and initially facilitate population transfer, leading to a steeper drop. However, as seen in section 6.2, a small R does not lead to a high ionisation rate. This is illustrated by the Wigner functions in Fig. 6.16: the quantum bridge brings population back to the right-side core. This cyclic motion does not follow the direction of the external field. As a consequence, the quasiprobability distribution does not stay within one centre during the 'flat' portion of the step autocorrelation function, as illustrated in Fig. 6.15.

Symmetric effect

While the effect of Z_l and Z_r differs greatly depending on the step cluster analysed, their effect is also mirrored, so conclusions on one cluster can be expanded to both. Focusing on the initially localised to the right cluster from Fig. 6.11, we see that while Z_l has little influence, the vast majority of step autocorrelation functions has $Z_r < 1.2$. This is illustrated in Fig. 6.17: The initial drop of the step autocorrelation function greatly reduces as Z_r increases. From the corresponding ΔE plot, the peak

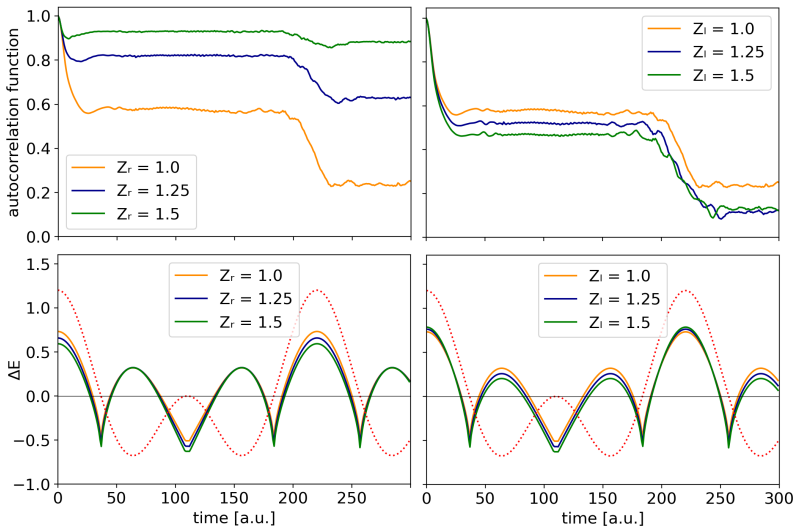

Figure 6.17: Different plots of autocorrelation functions and ΔE for [Left column] $Z_r = 1.0$ a.u., $Z_r = 1.25$ a.u. and $Z_r = 1.5$ a.u. with $Z_l = 1.0$ a.u.. and [Right column] $Z_l = 1.0$ a.u., $Z_l = 1.25$ a.u. and $Z_l = 1.5$ a.u. with $Z_r = 1.0$ a.u.. The initial wavepacket is localised to the right and other parameters are set to $R = 7$ a.u., $E_0 = 0.06$ a.u., $r_t = 1.0$ and $b = 0.5$. The external laser field is represented by the red dotted line (not to scale).

separatrix energy difference goes from 0.7 for $Z_r = 1.0$ to 0.6 for $Z_r = 1.5$. Compared to the effect of the separatrix energy difference of E_0 and its effect on the initial autocorrelation function drop, it appears something else must be at play. A better understanding is obtained when looking at the ionisation rate in static fields as a function of Z_r and Z_l. As explained in section 6.2.1, the biggest difference between Fig. 6.6 is not the separatrix energy difference, but the range of the bound region, especially in the momentum space. Back to the time dependent situation, as Z_r increases, the population (here initially localised to the right) stays trapped at the right molecular well, and the initial step drop will be much shorter.

Finally, the other parameters governing the initial wavepacket configuration are

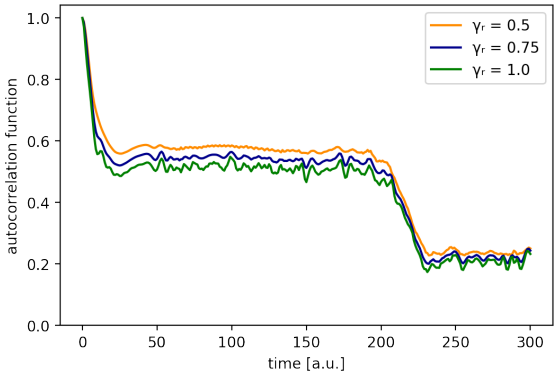

Figure 6.18: Different plots of autocorrelation functions $\gamma_r = 0.5$ [a.u.], $\gamma_r = 0.75$ [a.u.] and $\gamma_r = 1.0$ [a.u.] with $E_0 = 0.06$ [a.u.], $R = 7.0$ [a.u.], initial wavepacket localised to the right, with molecular weights $Z_r = Z_l = 1.0$. External field parameters are $r_t = 1.0$ and $B = 0.5$.

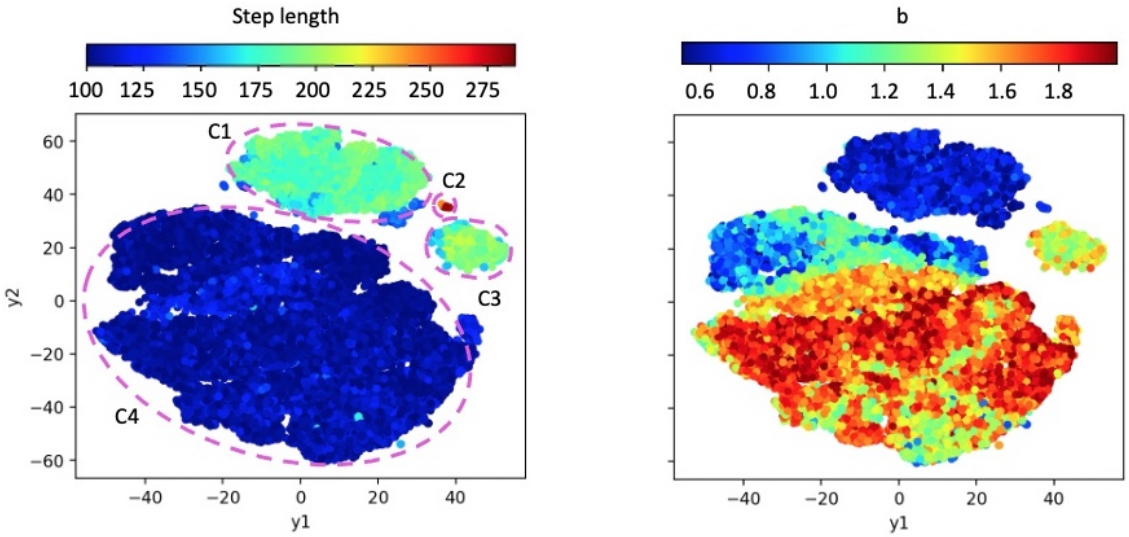

Figure 6.19: Plot of the 27 194 8-dimensional data points that have been projected onto two axis y_1 and y_2 using the t-SNE dimensional reduction technique described in section 2.6. All units are in [a.u.]. unless stated otherwise. Each subplot has the projected data plotted as a function a initial input parameter. The initial input parameters include (a) The output of the step function algorithm from section 6.1.2 that is the length of the step in the autocorrelation function and (b) the frequency-ratio of the second colour field b as well as not shown here the offset of the second field ϕ, the field ratio r_t, the internuclear distance R, the left molecular well depth Z_l, the right molecular well depth Z_r, the right initial wavepacket width γ_r. All data points use an initially localised to the right wavepacket with $E_0 = 0.07$. The input data set has been reduced from 1 000 000 data points to only look at step autocorrelation functions. PCA distributions using the original 1 000 000 data points have been analysed for accuracy (not shown).

γ_l and γ_r, the initial wavepacket widths. From Fig. 6.11, most step autocorrelation functions have γ around 0.5, and at least within the range [0.2:0.8]. Indeed, $\gamma = 0.5$ corresponds to the minimal ground-state energy of a field free single-centre soft-core potential with our current parameters. Fig. 6.18 shows what the change in γ does to the autocorrelation function. The oscillations during the "flat" section of the step function intensify as γ deviates from 0.5. That is because, despite being an initially localised wavepacket, part of the initial wavepacket bleeds out of the bound region.

Step length and two colour field frequencies

From Fig. 6.12 we can already observe that the step length is connected to the value of the two colour field frequency ratio b. Indeed, while step functions of step length less than 110 [a.u.] have on average $b = 1.5$, step functions of step length greater than 150 [a.u.] have on average $b = 0.9$.

In order to view the relationship between the step length and other parameters in greater detail, we will use a modified data set and perform the t-SNE dimensional reduction algorithm again. First, we only conserve data points with ‘step’

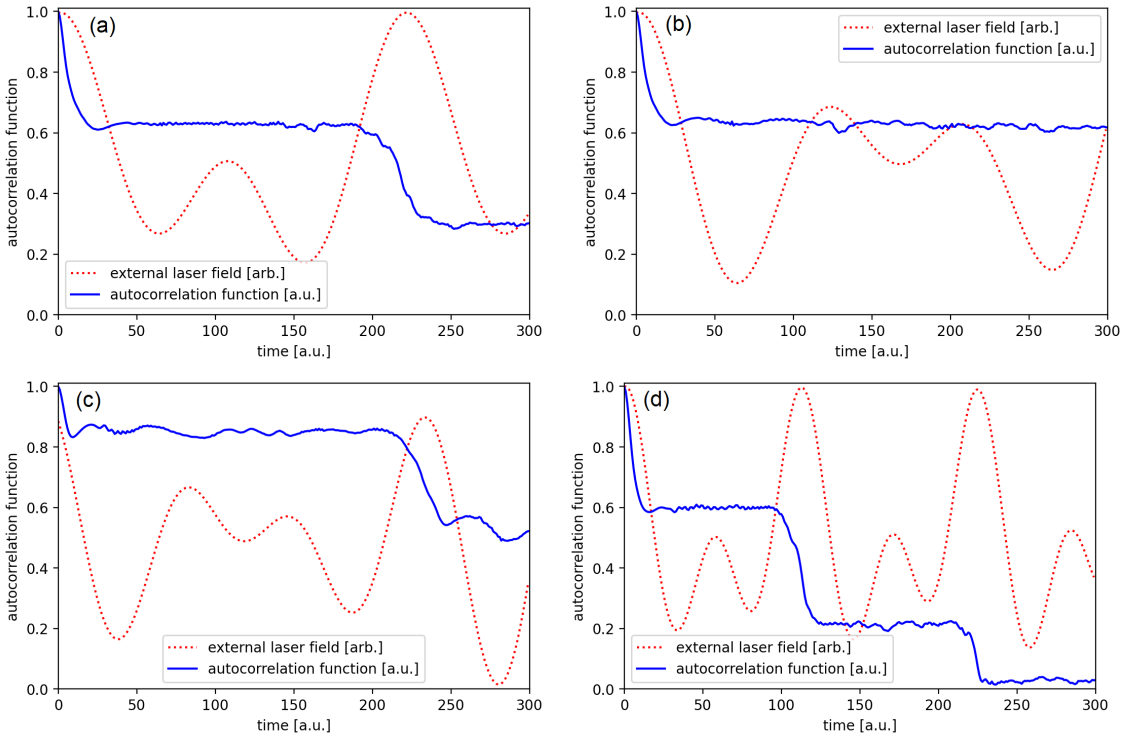

Figure 6.20: Plot of the corresponding autocorrelation function and external field in each of the four different clusters in Fig. 6.19, in order of increasing field frequency ration b. Constant parameters are $E_0 = 0.07$, $R = 7$, $\alpha = 0.0$, $\gamma_r = 0.5$. The parameters used in each subplot are (a) from C1; $b = 0.5$, $r_t = 1.0$, $\phi = -0.2$, $Z_r = 1.2$ and $Z_l = 1.2$, (b) from C2; $b = 0.7$, $r_t = 1.0$, $\phi = -0.2$, $Z_r = 1.2$ and $Z_l = 1.2$, (c) from C3; $b = 1.3$, $r_t = 1.0$, $\phi = 1.0$, $Z_r = 1.1$ and $Z_l = 1.1$ and (d) from C4; $b = 2.0$, $r_t = 1.0$, $\phi = -0.13$, $Z_r = 1.05$ and $Z_l = 1.5$.

autocorrelation functions. Next, we set the initial wavepacket to be localised at the right centre. This is equivalent to focusing only on the 'localised to the right' cluster of Fig. 6.9. Because of this, we also remove the initial wavepacket width γ_l and θ parameters. Finally, we fix the field strength to $E_0 = 0.07$ a.u.. These results are shown in Fig. 6.19.

The t-SNE algorithm separates the data into four different clusters. The C1 and C3 clusters represent step lengths between 110 and 260. They are distinguished by the value of the frequency ratio b of the two-color fields: the largest C1 having an average of $b = 0.65$ and the smallest C3 $b = 1.32$. Next, the C2 cluster is the smallest and corresponds to all autocorrelation functions with a very long (greater than 260) step length. Finally, the C4 cluster is the largest cluster and corresponds to all autocorrelation functions with a short step length. Here the average step length is 1.09. An example of autocorrelation function and external field within each cluster is shown in Fig. 6.20.

As seen in the previous sections, the temporal location of the field peak, when matched with the population localisation, determines the step drop. From this, we can assume that the specific times for which the field peaks occur match the step length. This can be seen in Fig. 6.20 (a) and (b), when increasing the second field frequency-ratio from $b = 0.5$ to $b = 0.7$, the distance between two field peaks increases and the step length goes from 187 to 285. This is also confirmed when looking at an example step function from clusters (c) and (d): The distance between field peaks matches the step length.

6.4 Conclusion

In this Chapter we use dimensionality reduction techniques, namely the the t-distributed stochastic neighbor embedding (t-SNE) method and Principal component analysis (PCA) to investigate the effect of multiple parameters at once in enhanced ionisation. We show how quantum effects in strong-field ionisation of stretched diatomic molecules may be understood, classified and synchronised with the external laser field in order to create tailored ionisation bursts. Thereby, the t-SNE was crucial to establish a hierarchy of parameters, and manipulate the relevant time scales. These time scales are either dictated by the field, or by the molecular system. The latter is associated with quantum-interference structures that provide a direct, intra-molecular population transfer via a quantum pathway in phase space: the quantum bridges studied in Chapters 3, 4 and 5. The results presented here have been mainly obtained with the t-SNE, while the PCA was used to rule out possible algorithm-dependent artefacts.

The effectiveness and accuracy of the t-SNE is first showcased on the ionisation rate using a static field. The expected results are found using phase-space

arguments and Wigner quasiprobability distributions. They completely match the conclusions drawn from the t-SNE distributions. Furthermore, a hierarchy in the importance of different parameters is quickly and effectively demonstrated. Because of this, we confidently used the t-SNE to project data of autocorrelation functions and their parameters for time-dependent fields. Using a two-colour field, we obtained a controlled ionisation release, which translates to a stepwise behaviour in the autocorrelation function. By using the t-SNE to project multi-dimensional data sets into 2 dimensions, ionisation profiles obtained while varying multiple parameters at once are organised and understood.

A conclusion from Chapters 3 and 5 was that a key to understand enhanced ionisation is the interplay between the intra-molecular quantum bridges and the external field. This also holds for controlled ionisation release (represented by a step function in the autocorrelation function), where the system requires a short burst of enhanced ionisation followed by a time interval during which the population stays bounded.

Quantum bridges are tied to many predictors for a step function in the autocorrelation function, including the strongest one: electron localisation. A delocalised initial wavepacket creates an interference pattern in both positive and negative momentum space. This leads to ionisation bursts that do not follow the external field. Therefore, we cannot obtain a time interval for which the population stays bounded. Moreover, the quantum bridges are highly tied to the internuclear distance. For that reason, configurations that suppress momentum gates do not lead to the burst of ionisation needed. This is the case when the internuclear distance is too large. Alternatively, a too small internuclear distance leads to cyclic motion in the momentum space, regardless of the initial state. This also stops the population from staying bounded at one centre.

On the other hand, a higher field peak maximum leads to stronger ionisation bursts. A stronger field peak is achieved by increasing the field amplitude E_0 or adding a second field. This is neatly quantifiable by the separatrix energy difference ΔE. From this we determine bounded regions with closed separatrices and ionisation burst regions when the localisation is upfield with open separatrices. The timing of these field peaks matching with the upfield population lead to the start of the autocorrelation function drops. The field frequency determines the distance between the field peaks and is therefore the key to controlling the length of the steps. Finally, changing the molecular weights $Z_{r,l}$ affects the presence of step functions. As the upfield molecular weight increases, the upfield bound region increases and this greatly suppresses ionisation.

In summary, we can understand the physical cause and requirements for controlled ionisation release by separating the phenomenon into two steps, a short burst of enhanced ionisation and a time interval where the population stays bounded. For

static fields, the optimal configuration for enhanced ionisation is pinpointed to an initial wavepacket localised upfield at optimal internuclear distance with a high intensity external field and a low upfield molecular weight. The separatrices are open with a high separatrix energy difference. This also holds during the time-dependent ionisation burst time interval, and will be periodic as the upfield and downfield configurations will change along with the sign of the external field, matching the field frequency. For the population to stay bounded, either the field strength must be low, separatrices closed or barely open, or the population must be localised in the downfield centre and therefore not follow the changes in the field strength and direction. In addition, the population must not cycle around through momentum gates, meaning the internuclear distance cannot be too short. The t-SNE was greatly effective at separating results into clusters and therefore visualising results due to specific combinations of parameters. For example, an overall analysis of the effect of Z_r on the step function autocorrelation function reveals only negligible effects. However, the step function results were separated into two clusters $\alpha < 0.2$ and $\alpha > 0.8$. The effect of the increased bound region and ionisation suppression from Z_r only affecting the $\alpha < 0.2$ cluster is brought into focus. Moreover, the t-SNE presented a hierarchy of the correlation between different parameters and the quantity of study. From that, the role of electron localisation was pinpointed as the key parameter.

The importance of electron localisation is in agreement with the findings by several groups, reported over many years. In fact, resolving and ultimately controlling electron localisation in extended or dissociating molecules holds the promise of steering chemical reactions. This has led to many studies, both theoretical and experimental, employing, for instance, pump-probe schemes [183, 250, 233, 234, 251, 235], CEP stabilised few-cycle pulses [252, 232], long-wavelength fields [253, 254] or synthesised wave forms [255]. Moreover, orthogonally polarised fields have also been applied to trace or control the ionisation site [182, 256, 181]. Regarding enhanced ionisation, electron localisation in the upfield well, together with coupled charge-resonant states, were widely mentioned in the literature as major contributing factors. This holds both for seminal enhanced ionisation papers [162, 165] and more recent work in which models for time-dependent ionisation bursts have been developed [257, 75, 258, 259].

Since potential wells occur in a wide range of physical systems, the present techniques can be applied not only to more realistic molecular models, but also to solids and nanostructures. Thereby, a crucial issue would be to incorporate other degrees of freedom, multielectron dynamics and assess the role of decoherence. Loss of coherence can be caused by many physical mechanisms, such as coupling with additional degrees of freedom, intensity fluctuations, and incoherent emission from across the focal volume (for a brief discussion of some decoherence mechanisms in the context of strong-field quantum sensing see [260]). Recent studies using pump-

probe schemes in H_2 have shown that coupling of electronic and vibrational degrees of freedom affects coherence and may hinder electron localisation [261]. Still, studies in large molecules indicate that phase relations may be preserved even in systems with many degrees of freedom [262], and could even be controlled leading to tailored ionisation enhancement or suppression [263]. This simplified model is meant as a proof of concept and a first step towards more realistic scenarios.

Chapter 7

Summary

The main topic of this thesis is non-classical features in strong field enhanced ionisation, at the attosecond scale. In order to understand the dynamics of our system, we mainly use both classical and quantum phase space tools. We begin this thesis with an overview of phase space methods in attoscience in Chapter 1, including a broad overview of the existing landscape, with a focus on strong-field ionisation and rescattering, high-order harmonic generation, stabilisation and free-electron lasers. Furthermore we provide an overview of enhanced ionisation, a phenomenon that happens to stretched molecules in low frequency, high intensity fields that consists of a sharp increase of the ionisation rate at specific internuclear distances. In H_2^+, several ionisation bursts that do not follow the time profile of the external field have been identified. When using Wigner quasi-probability distributions, structures that cycle through the momentum space, called momentum gates [76] have been associated with this phenomenon. In Chapter 3, we investigate the momentum gates and find that they can occur even when using a static field. By considering various initial wavepackets and internuclear distances and using Wigner quasiprobability distributions, we conclude that their primary cause is an interference-induced bridging mechanism that occurs if both wells in the molecule are populated. When the initial wavepacket is delocalised, or when the internuclear distance leads to nested separatrices, the Wigner function performs a clockwise rotation whose period is intrinsic to the molecule. At a critical nuclear distance, with an initial wavepacket localised upfield, the optimal conditions for enhanced ionisation occur. The molecular wells are close enough to allow a quantum bridge between them to form, but not so close as to cycle the population back to the upfield well. There the quantum bridge provides a direct pathway for the upfield wavepacket to the downfield well, which then follows the semiclassical escape pathway to the continuum. As seen using the quantum Liouville equation, the evolution of the Wigner function around the momentum gates is essentially non-classical (as opposed to its evolution at the semiclassical escape pathway). This means estimating the frequency of the quantum bridging mechanism with classical arguments provides limited results.

We continue the investigation of the quantum evolution of the momentum gates using the QTM. In Chapter 4 we aim at propagating directly quantum trajectories by discretising the density, following the work of [211, 212, 213]. By modifying the computational method to improve on its accuracy, and more specifically on the evolution of boundary trajectories, similar results can be obtained using a much smaller number of trajectories. The goal of these improvements was to limit the computational issues that arise when the trajectories are clustered together and eventually allow an investigation of the non-classical effects in enhanced ionisation with quantum trajectories. While this allowed the investigation of the quantum potential as a non-classicality criteria for atomic tunnel ionisation, it fails for the propagation of quantum trajectories in double well potential systems because of the rapid changes in the quantum potential.

Instead, using a hyperbolic potential model in a field-free system in Chapter 5 enabled us to apply an analytical approach to study the frequency of the cyclic motion of the momentum gates. This novel analytical model, presented in [215], leads to obtaining the eigenfrequencies at play. From those we can conclude that the pure frequency qualitatively observed is caused by the presence of only two even Fourier coefficients Λ. These frequencies are robust upon the inclusion of an external static field, and allow for the study of the interplay between an external time-dependent field frequency and the dynamics of the quantum bridging mechanism. Indeed, the momentum gates (having the highest frequency) may at times aid or hinder enhanced ionisation. The quasiprobability distribution at times counter-intuitively flows against the field gradient. These mechanisms could be optimised using the appropriate initial states and driving fields.

Since the large number of tunable parameters involved in this system limits the qualitative assessment of each individual parameter, Chapter 6 brings machine learning dimensional reduction techniques to the forefront. The effectiveness of the t-SNE projection is demonstrated within the ionisation mechanisms of a stretched molecule in a static field. The results match those found using phase space arguments and Wigner quasiprobability distributions. Furthermore, the t-SNE is fast, presents a clear hierarchy of parameters, and allows the visualisation of non-linear effects due to combinations of parameters. Consequently we applied this method to the more complex issue of controlled bursts of ionisation. Indeed, when using a polychromatic field, the autocorrelation function can present a stepwise behaviour. After projecting our dataset onto 2-dimensions with the t-SNE, we conclude that the system requires a localised initial wavepacket in order to admit both bursts of enhanced ionisation and periods of suppressed ionisation, whose length is determined by the frequency ratio of the external two-colour field.

Moving forward, as the t-SNE is purposefully made for the projection of very high dimensional datasets, the model system used throughout this thesis can be expanded

in complexity (pulse shape, multi-dimensional model, etc). More generally, the phase-space and machine learning tools presented in this thesis can be applied to many areas of strong field and attosecond sciences.

Appendix A

Atomic units

Throughout this thesis we use atomic units, meaning $\hbar = m = e^2 = 1.$. In the table below the value of different unit quantities is displayed.

Length	$\frac{\hbar^2}{me^2} = 5.29177249\ 10^{-11}$ m
Velocity	$\frac{e^2}{\hbar} = 2.18769142\ 10^{6}$ m/s
Time	$\frac{\hbar^3}{me^4} = 2.41888433\ 10^{-17}$ s
Intensity	$3.51\ 10^{16}$ W/cm^2
Electric field strength	$\frac{m^2e^5}{\hbar^4} = 5.14220826\ 10^{11}$ V/m
Frequency	$\frac{me^4}{\hbar^3} = 4.13413732$ Hz $\Rightarrow \lambda = 45.56$ nm
Energy	$\frac{me^4}{\hbar^2} = 27.2113962$ eV

Appendix B

Principal Component Analysis

In this Appendix we will present a few of the PCA results obtained throughout Chapter 6. The aim of PCA is to compute the eigenvectors of the covariance matrix (principal components) of the multidimensional data set and recast the data along the two largest eigenvectors. In other words, the first principal component can be defined as the direction that maximises the variance of the projected data. Throughout Chapter 6 all t-SNE distributions were computed along with PCA distributions for comparison. In this appendix we present two examples, one from the static field analysis in section 6.2 and one from the time-dependent step autocorrelation function analysis in section 6.3, Fig. B.1 and Fig. B.2 respectively.

The PCA distribution in Fig. B.1, obtained for the ionisation rate data set calculated using the static field, does not exhibit individual clusters corresponding to different ionisation rates. However, the distribution is organised following the different ionisation rates. From this we can see that both upfield electron localisation ($\alpha = 0$) and a right molecular weight $Z_r = 1.0$ lead to the highest ionisation rates.

When it comes to the time-dependent autocorrelation function, the PCA distribution in Fig. B.2 does break into three distinct clusters corresponding to the different autocorrelation outputs: constant, step, and other. This allows us to draw similar conclusions to those obtained with the t-SNE, for instance that the electron must be localised to the right or left in order for the autocorrelation function to have a stepwise shape. However, contrary to the t-SNE distribution shown in Fig. 6.9, the step autocorrelation initially localised to the right data points and those initially localised to the left are not separated. That means that parameters that affect those two groups differently will not have their effect visually represented, for example Z_r and Z_l.

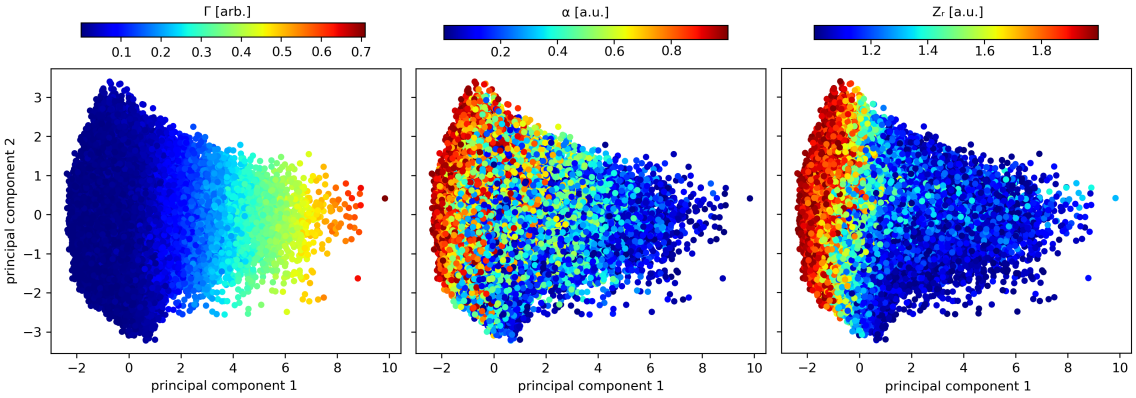

Figure B.1: Plot of the 100 000 9-dimensional data points that have been projected onto their two principal component axis using PCA. The initial parameters used are equal to that of Figure. 6.8. Each subplot has the projected data plotted as a function an initial input parameter. The initial input parameters include (a) the ionisation rate Γ, (b) the electron localisation α and (c) the right molecular well depth Z_r.

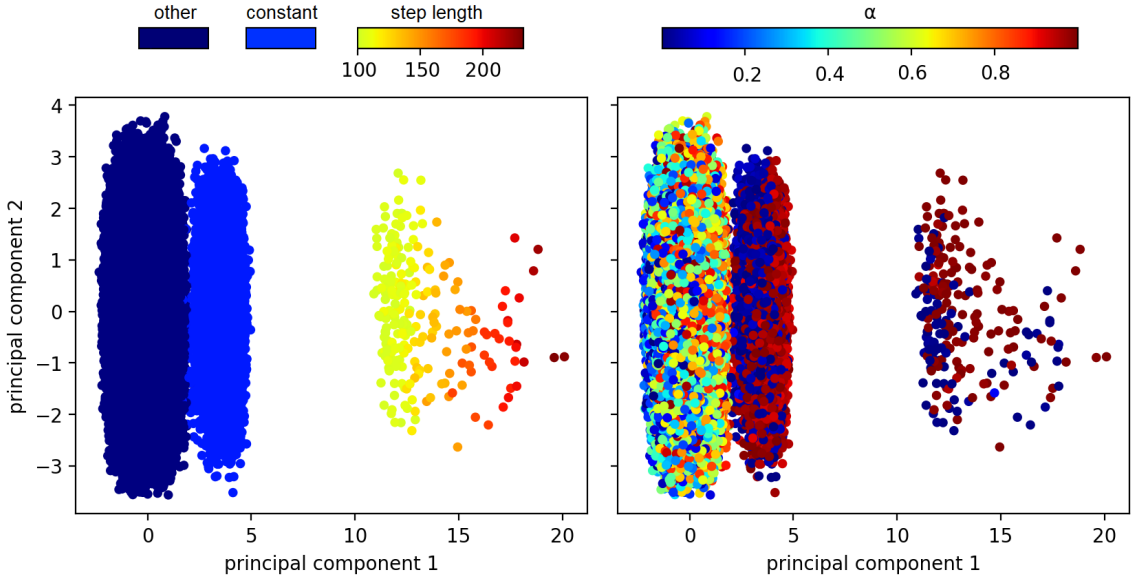

Figure B.2: Plot of the 500 000 12-dimensional data points that have been projected onto their two principal component axis using PCA. The initial parameters used are equal to that of Figure. 6.9. Each subplot has the projected data plotted as a function an initial input parameter. The initial input parameters include (a) The step function shape obtained by the sorting algorithm in section 6.1.2 that outputs 'constant', 'other', or the length of the step in the autocorrelation function and (b) the electron localisation α.

Bibliography

[1] J. Weinbub and D. K. Ferry. “Recent advances in Wigner function approaches”. In: *Applied Physics Reviews* 5.4 (2018), p. 041104. DOI: 10.1063/1.5046663. eprint: https://doi.org/10.1063/1.5046663. URL: https://doi.org/10.1063/1.5046663.

[2] J. Liouville. “Note sur la Théorie de la Variation des constantes arbitraires.” In: *Journal de Mathématiques Pures et Appliquées* (1838), pp. 342–349. URL: http://eudml.org/doc/234417.

[3] Carl Gustav Jakob Jacobi et al. *Jacobi’s Vorlesungen über Dynamik: Gehalten an der Universität zu Königsberg im Wintersemester 1842-1843 und nach einem von C.W. Borchart ausgearbeiteten Hefte*. Berlin :G. Reimer, 1884. URL: https://www.biodiversitylibrary.org/item/58380.

[4] D. L. Goroff. “Henri Poincaré: New methods of celestial mechanics.” In: *Hist. Mod. Phys. Astron.* 13 (Jan. 1993).

[5] D. Nolte. “The tangled tale of phase space”. In: *Physics Today* 63 (2010), pp. 33–38.

[6] E. Wigner. “On the Quantum Correction For Thermodynamic Equilibrium”. In: *Phys. Rev.* 40 (5 June 1932), pp. 749–759. DOI: 10.1103/PhysRev.40.749. URL: https://link.aps.org/doi/10.1103/PhysRev.40.749.

[7] Eric J. Heller. “Wigner phase space method: Analysis for semiclassical applications”. In: *The Journal of Chemical Physics* 65.4 (1976), pp. 1289–1298. DOI: 10.1063/1.433238. eprint: https://doi.org/10.1063/1.433238. URL: https://doi.org/10.1063/1.433238.

[8] M. Hillery et al. “Distribution functions in physics: Fundamentals”. In: *Physics Reports* 106.3 (1984), pp. 121–167. ISSN: 0370-1573. DOI: https://doi.org/10.1016/0370-1573(84)90160-1. URL: https://www.sciencedirect.com/science/article/pii/0370157384901601.

[9] Hai-Woong Lee. “Theory and application of the quantum phase-space distribution functions”. In: *Physics Reports* 259.3 (1995), pp. 147–211. ISSN: 0370-1573. DOI: https://doi.org/10.1016/0370-1573(95)00007-4. URL: http://www.sciencedirect.com/science/article/pii/0370157395000074.

[10] K. E. Cahill and R. J. Glauber. "Density Operators and Quasiprobability Distributions". In: *Phys. Rev.* 177 (5 Jan. 1969), pp. 1882–1902. DOI: 10.1103/PhysRev.177.1882. URL: https://link.aps.org/doi/10.1103/PhysRev.177.1882.

[11] G. S. Agarwal and E. Wolf. "Calculus for Functions of Noncommuting Operators and General Phase-Space Methods in Quantum Mechanics. I. Mapping Theorems and Ordering of Functions of Noncommuting Operators". In: *Phys. Rev. D* 2 (10 Nov. 1970), pp. 2161–2186. DOI: 10.1103/PhysRevD.2.2161. URL: https://link.aps.org/doi/10.1103/PhysRevD.2.2161.

[12] Kin'ya Takahashi and Nobuhiko Saitô. "Chaos and Husimi Distribution Function in Quantum Mechanics". In: *Phys. Rev. Lett.* 55 (7 Aug. 1985), pp. 645–648. DOI: 10.1103/PhysRevLett.55.645. URL: https://link.aps.org/doi/10.1103/PhysRevLett.55.645.

[13] W.P. Schleich. *Quantum Optics in Phase Space*. Wiley, 2011. ISBN: 9783527635009. URL: https://books.google.co.uk/books?id=2jUjQPW-WXAC.

[14] Stephen M. Barnett and Paul M. Radmore. *Methods in theoretical quantum optics*. Clarendon Press, 2005.

[15] Miguel A. Alonso. "Wigner functions in optics: describing beams as ray bundles and pulses as particle ensembles". In: *Adv. Opt. Photon.* 3.4 (Dec. 2011), pp. 272–365. DOI: 10.1364/AOP.3.000272. URL: http://aop.osa.org/abstract.cfm?URI=aop-3-4-272.

[16] G. S. Agarwal. "Relation between atomic coherent-state representation, state multipoles, and generalized phase-space distributions". In: *Phys. Rev. A* 24 (6 Dec. 1981), pp. 2889–2896. DOI: 10.1103/PhysRevA.24.2889. URL: https://link.aps.org/doi/10.1103/PhysRevA.24.2889.

[17] Jonathan P. Dowling, G. S. Agarwal, and Wolfgang P. Schleich. "Wigner distribution of a general angular-momentum state: Applications to a collection of two-level atoms". In: *Phys. Rev. A* 49 (5 May 1994), pp. 4101–4109. DOI: 10.1103/PhysRevA.49.4101. URL: https://link.aps.org/doi/10.1103/PhysRevA.49.4101.

[18] A Czirják and M G Benedict. "Joint Wigner function for atom - field interactions". In: *Quantum and Semiclassical Optics: Journal of the European Optical Society Part B* 8.5 (Oct. 1996), pp. 975–981. DOI: 10.1088/1355-5111/8/5/003. URL: https://doi.org/10.1088/1355-5111/8/5/003.

[19] M. G. Benedict and A. Czirják. "Wigner functions, squeezing properties, and slow decoherence of a mesoscopic superposition of two-level atoms". In: *Phys. Rev. A* 60 (5 Nov. 1999), pp. 4034–4044. DOI: 10.1103/PhysRevA.60.4034. URL: https://link.aps.org/doi/10.1103/PhysRevA.60.4034.

[20] Roy J. Glauber. "Coherent and Incoherent States of the Radiation Field". In: *Phys. Rev.* 131 (6 Sept. 1963), pp. 2766–2788. DOI: 10.1103/PhysRev.131.2766. URL: https://link.aps.org/doi/10.1103/PhysRev.131.2766.

[21] E. C. G. Sudarshan. "Equivalence of Semiclassical and Quantum Mechanical Descriptions of Statistical Light Beams". In: *Phys. Rev. Lett.* 10 (7 Apr. 1963), pp. 277–279. DOI: 10.1103/PhysRevLett.10.277. URL: https://link.aps.org/doi/10.1103/PhysRevLett.10.277.

[22] Samuel L. Braunstein and Peter van Loock. "Quantum information with continuous variables". In: *Rev. Mod. Phys.* 77 (2 June 2005), pp. 513–577. DOI: 10.1103/RevModPhys.77.513. URL: https://link.aps.org/doi/10.1103/RevModPhys.77.513.

[23] Alessio Serafini. *Quantum continuous variables: a primer of theoretical methods*. CRC Press, Taylor and Francis Group, 2017.

[24] V V Dodonov. "'Nonclassical' states in quantum optics: a 'squeezed' review of the first 75 years". In: *Journal of Optics B: Quantum and Semiclassical Optics* 4.1 (Jan. 2002), R1–R33. DOI: 10.1088/1464-4266/4/1/201. URL: https://doi.org/10.1088/1464-4266/4/1/201.

[25] B. M. Garraway and P. L. Knight. "Comparison of quantum-state diffusion and quantum-jump simulations of two-photon processes in a dissipative environment". In: *Phys. Rev. A* 49 (2 Feb. 1994), pp. 1266–1274. DOI: 10.1103/PhysRevA.49.1266. URL: https://link.aps.org/doi/10.1103/PhysRevA.49.1266.

[26] B. M. Garraway and P. L. Knight. "Evolution of quantum superpositions in open environments: Quantum trajectories, jumps, and localization in phase space". In: *Phys. Rev. A* 50 (3 Sept. 1994), pp. 2548–2563. DOI: 10.1103/PhysRevA.50.2548. URL: https://link.aps.org/doi/10.1103/PhysRevA.50.2548.

[27] Victor Veitch et al. "Negative quasi-probability as a resource for quantum computation". In: *New Journal of Physics* 14.11 (Nov. 2012), p. 113011. DOI: 10.1088/1367-2630/14/11/113011. URL: https://doi.org/10.1088/1367-2630/14/11/113011.

[28] A. Ketterer et al. "Quantum information processing in phase space: A modular variables approach". In: *Phys. Rev. A* 94 (2 Aug. 2016), p. 022325. DOI: 10.1103/PhysRevA.94.022325. URL: https://link.aps.org/doi/10.1103/PhysRevA.94.022325.

[29] Robert Raussendorf et al. “Phase-space-simulation method for quantum computation with magic states on qubits”. In: *Phys. Rev. A* 101 (1 Jan. 2020), p. 012350. DOI: 10.1103/PhysRevA.101.012350. URL: https://link.aps.org/doi/10.1103/PhysRevA.101.012350.

[30] K. Vogel and H. Risken. “Determination of quasiprobability distributions in terms of probability distributions for the rotated quadrature phase”. In: *Phys. Rev. A* 40 (5 Sept. 1989), pp. 2847–2849. DOI: 10.1103/PhysRevA.40.2847. URL: https://link.aps.org/doi/10.1103/PhysRevA.40.2847.

[31] B M Garraway and P L Knight. “Quantum superpositions, phase distributions and quasi-probabilities”. In: *Physica Scripta* T48 (Jan. 1993), pp. 66–76. DOI: 10.1088/0031-8949/1993/t48/010. URL: https://doi.org/10.1088/0031-8949/1993/t48/010.

[32] Anatoli Polkovnikov. “Phase space representation of quantum dynamics”. In: *Annals of Physics* 325.8 (2010), pp. 1790–1852. ISSN: 0003-4916. DOI: https://doi.org/10.1016/j.aop.2010.02.006. URL: https://www.sciencedirect.com/science/article/pii/S0003491610000382.

[33] William H. Miller. “The Semiclassical Initial Value Representation: A Potentially Practical Way for Adding Quantum Effects to Classical Molecular Dynamics Simulations”. In: *The Journal of Physical Chemistry A* 105.13 (Apr. 2001), pp. 2942–2955. ISSN: 1089-5639. DOI: 10.1021/jp003712k. URL: https://doi.org/10.1021/jp003712k.

[34] William H. Miller. “Quantum dynamics of complex molecular systems”. In: *Proceedings of the National Academy of Sciences* 102.19 (2005), pp. 6660–6664. ISSN: 0027-8424. DOI: 10.1073/pnas.0408043102. eprint: https://www.pnas.org/content/102/19/6660.full.pdf. URL: https://www.pnas.org/content/102/19/6660.

[35] Benjamin Lasorne, Graham A. Worth, and Michael A. Robb. “Non-adiabatic Photochemistry: Ultrafast Electronic State Transitions and Nuclear Wavepacket Coherence”. In: *Molecular Quantum Dynamics: From Theory to Applications*. Ed. by Fabien Gatti. Berlin, Heidelberg: Springer Berlin Heidelberg, 2014, pp. 181–211. ISBN: 978-3-642-45290-1. DOI: 10.1007/978-3-642-45290-1_7. URL: https://doi.org/10.1007/978-3-642-45290-1_7.

[36] P.B. Blakie et al. “Dynamics and statistical mechanics of ultra-cold Bose gases using c-field techniques”. In: *Advances in Physics* 57.5 (2008), pp. 363–455. DOI: 10.1080/00018730802564254. eprint: https://doi.org/10.1080/00018730802564254. URL: https://doi.org/10.1080/00018730802564254.

[37] Göran Wahnström, Benny Carmeli, and Horia Metiu. "The calculation of the thermal rate coefficient by a method combining classical and quantum mechanics". In: *The Journal of Chemical Physics* 88.4 (1988), pp. 2478–2491. DOI: 10.1063/1.454028. eprint: https://doi.org/10.1063/1.454028. URL: https://doi.org/10.1063/1.454028.

[38] Haobin Wang, Xiong Sun, and William H. Miller. "Semiclassical approximations for the calculation of thermal rate constants for chemical reactions in complex molecular systems". In: *The Journal of Chemical Physics* 108.23 (1998), pp. 9726–9736. DOI: 10.1063/1.476447. eprint: https://doi.org/10.1063/1.476447. URL: https://doi.org/10.1063/1.476447.

[39] A. O. Caldeira and A. J. Leggett. "Quantum tunnelling in a dissipative system". English (US). In: *Annals of Physics* 149.2 (Sept. 1983), pp. 374–456. ISSN: 0003-4916. DOI: 10.1016/0003-4916(83)90202-6.

[40] Eric J. Heller. "Time-dependent approach to semiclassical dynamics". In: *The Journal of Chemical Physics* 62.4 (1975), pp. 1544–1555. DOI: 10.1063/1.430620. eprint: https://doi.org/10.1063/1.430620. URL: https://doi.org/10.1063/1.430620.

[41] William H. Miller. "Semiclassical limit of quantum mechanical transition state theory for nonseparable systems". In: *The Journal of Chemical Physics* 62.5 (1975), pp. 1899–1906. DOI: 10.1063/1.430676. eprint: https://doi.org/10.1063/1.430676. URL: https://doi.org/10.1063/1.430676.

[42] Eric J. Heller. "Frozen Gaussians: A very simple semiclassical approximation". In: *The Journal of Chemical Physics* 75.6 (1981), pp. 2923–2931. DOI: 10.1063/1.442382. eprint: https://doi.org/10.1063/1.442382. URL: https://doi.org/10.1063/1.442382.

[43] Michael F. Herman and Edward Kluk. "A semiclasical justification for the use of non-spreading wavepackets in dynamics calculations". In: *Chemical Physics* 91.1 (1984), pp. 27–34. ISSN: 0301-0104. DOI: https://doi.org/10.1016/0301-0104(84)80039-7. URL: http://www.sciencedirect.com/science/article/pii/0301010484800397.

[44] Dmitrii V Shalashilin and Mark S Child. "The phase space CCS approach to quantum and semiclassical molecular dynamics for high-dimensional systems". In: *Chemical Physics* 304.1 (2004). Towards Multidimensional Quantum Reaction Dynamics, pp. 103–120. ISSN: 0301-0104. DOI: https://doi.org/10.1016/j.chemphys.2004.06.013. URL: http://www.sciencedirect.com/science/article/pii/S0301010404002824.

[45] Michael Werther, Sreeja Loho Choudhury, and Frank Großmann. "Coherent state based solutions of the time-dependent Schrödinger equation: hierarchy of approximations to the variational principle". In: *International Reviews in Physical Chemistry* 40.1 (2021), pp. 81–125. DOI: 10.1080/0144235X.2020.1823168. eprint: https://doi.org/10.1080/0144235X.2020.1823168. URL: https://doi.org/10.1080/0144235X.2020.1823168.

[46] M. J. Steel et al. "Dynamical quantum noise in trapped Bose-Einstein condensates". In: *Phys. Rev. A* 58 (6 Dec. 1998), pp. 4824–4835. DOI: 10.1103/PhysRevA.58.4824. URL: https://link.aps.org/doi/10.1103/PhysRevA.58.4824.

[47] Alice Sinatra, Carlos Lobo, and Yvan Castin. "The truncated Wigner method for Bose-condensed gases: limits of validity and applications". In: *Journal of Physics B: Atomic, Molecular and Optical Physics* 35.17 (Aug. 2002), pp. 3599–3631. DOI: 10.1088/0953-4075/35/17/301. URL: https://doi.org/10.1088/0953-4075/35/17/301.

[48] Anatoli Polkovnikov. "Evolution of the macroscopically entangled states in optical lattices". In: *Phys. Rev. A* 68 (3 Sept. 2003), p. 033609. DOI: 10.1103/PhysRevA.68.033609. URL: https://link.aps.org/doi/10.1103/PhysRevA.68.033609.

[49] Anatoli Polkovnikov and Daw-Wei Wang. "Effect of Quantum Fluctuations on the Dipolar Motion of Bose-Einstein Condensates in Optical Lattices". In: *Phys. Rev. Lett.* 93 (7 Aug. 2004), p. 070401. DOI: 10.1103/PhysRevLett.93.070401. URL: https://link.aps.org/doi/10.1103/PhysRevLett.93.070401.

[50] Lorenzo Isella and Janne Ruostekoski. "Nonadiabatic dynamics of a Bose-Einstein condensate in an optical lattice". In: *Phys. Rev. A* 72 (1 July 2005), p. 011601. DOI: 10.1103/PhysRevA.72.011601. URL: https://link.aps.org/doi/10.1103/PhysRevA.72.011601.

[51] L. Isella and J. Ruostekoski. "Quantum dynamics in splitting a harmonically trapped Bose-Einstein condensate by an optical lattice: Truncated Wigner approximation". In: *Phys. Rev. A* 74 (6 Dec. 2006), p. 063625. DOI: 10.1103/PhysRevA.74.063625. URL: https://link.aps.org/doi/10.1103/PhysRevA.74.063625.

[52] R. G. Scott, D. A. W. Hutchinson, and C. W. Gardiner. "Disruption of reflecting Bose-Einstein condensates due to interatomic interactions and quantum noise". In: *Phys. Rev. A* 74 (5 Nov. 2006), p. 053605. DOI: 10.1103/PhysRevA.74.053605. URL: https://link.aps.org/doi/10.1103/PhysRevA.74.053605.

[53] P. B. Corkum. “Plasma perspective on strong field multiphoton ionization”. In: *Phys. Rev. Lett.* 71 (13 Sept. 1993), pp. 1994–1997. DOI: 10.1103/PhysRevLett.71.1994. URL: https://link.aps.org/doi/10.1103/PhysRevLett.71.1994.

[54] M. Lewenstein et al. “Theory of high-harmonic generation by low-frequency laser fields”. In: *Phys. Rev. A* 49 (3 Mar. 1994), pp. 2117–2132. DOI: 10.1103/PhysRevA.49.2117. URL: https://link.aps.org/doi/10.1103/PhysRevA.49.2117.

[55] P. Salières et al. “Feynman’s Path-Integral Approach for Intense-Laser-Atom Interactions”. In: *Science* 292.5518 (2001), pp. 902–905. ISSN: 0036-8075. DOI: 10.1126/science.108836. eprint: https://science.sciencemag.org/content/292/5518/902.full.pdf. URL: https://science.sciencemag.org/content/292/5518/902.

[56] Ken Schafer, Ziyie Wei, and Marc Vrakking. “Special issue celebrating 25 years of re-collision physics”. In: *Journal of Physics B: Atomic, Molecular and Optical Physics* 50.17 (Aug. 2017), p. 170201. DOI: 10.1088/1361-6455/aa8052. URL: https://doi.org/10.1088/1361-6455/aa8052.

[57] D B Milošević et al. “Above-threshold ionization by few-cycle pulses”. In: *Journal of Physics B: Atomic, Molecular and Optical Physics* 39.14 (July 2006), R203–R262. DOI: 10.1088/0953-4075/39/14/r01. URL: https://doi.org/10.1088/0953-4075/39/14/r01.

[58] W Becker et al. “The plateau in above-threshold ionization: the keystone of rescattering physics”. In: *Journal of Physics B: Atomic, Molecular and Optical Physics* 51.16 (July 2018), p. 162002. DOI: 10.1088/1361-6455/aad150. URL: https://doi.org/10.1088/1361-6455/aad150.

[59] C. Figueira de Morisson Faria and X. Liu. “Electron–electron correlation in strong laser fields”. In: *Journal of Modern Optics* 58.13 (2011), pp. 1076–1131. DOI: 10.1080/09500340.2010.543958. eprint: https://doi.org/10.1080/09500340.2010.543958. URL: https://doi.org/10.1080/09500340.2010.543958.

[60] Wilhelm Becker et al. “Theories of photoelectron correlation in laser-driven multiple atomic ionization”. In: *Rev. Mod. Phys.* 84 (3 July 2012), pp. 1011–1043. DOI: 10.1103/RevModPhys.84.1011. URL: https://link.aps.org/doi/10.1103/RevModPhys.84.1011.

[61] P. M. Paul et al. “Observation of a Train of Attosecond Pulses from High Harmonic Generation”. In: *Science* 292.5522 (2001), pp. 1689–1692. ISSN: 0036-8075. DOI: 10.1126/science.1059413. URL: https://science.sciencemag.org/content/292/5522/1689.

[62] M. Hentschel et al. “Attosecond metrology”. In: *Nature* 414.6863 (Nov. 2001), pp. 509–513. ISSN: 1476-4687. DOI: 10.1038/35107000. URL: https://doi.org/10.1038/35107000.

[63] Reinhard Kienberger, Zenghu Chang, and Chang Hee Nam. “10th anniversary of attosecond pulses”. In: *Journal of Physics B: Atomic, Molecular and Optical Physics* 45.7 (Mar. 2012), p. 070201. DOI: 10.1088/0953-4075/45/7/070201. URL: https://doi.org/10.1088/0953-4075/45/7/070201.

[64] P. B. Corkum and Ferenc Krausz. “Attosecond science”. In: *Nature Physics* 3.6 (June 2007), pp. 381–387. ISSN: 1745-2481. DOI: 10.1038/nphys620. URL: https://doi.org/10.1038/nphys620.

[65] Manfred Lein. “Molecular imaging using recolliding electrons”. In: *Journal of Physics B: Atomic, Molecular and Optical Physics* 40.16 (Aug. 2007), R135–R173. DOI: 10.1088/0953-4075/40/16/r01. URL: https://doi.org/10.1088/0953-4075/40/16/r01.

[66] Ferenc Krausz and Misha Ivanov. “Attosecond physics”. In: *Rev. Mod. Phys.* 81 (1 Feb. 2009), pp. 163–234. DOI: 10.1103/RevModPhys.81.163. URL: https://link.aps.org/doi/10.1103/RevModPhys.81.163.

[67] B. B. Augstein and C. Figueira De Morisson Faria. “High-order harmonic generation in diatomic molecules: Quantum interference, nodal structures and multiple orbitals”. In: *Modern Physics Letters B* 26.02 (2012), p. 1130002. DOI: 10.1142/S021798491130002X. eprint: https://doi.org/10.1142/S021798491130002X. URL: https://doi.org/10.1142/S021798491130002X.

[68] C Figueira de Morisson Faria and A S Maxwell. “It is all about phases: ultrafast holographic photoelectron imaging”. In: *Reports on Progress in Physics* 83.3 (Jan. 2020), p. 034401. DOI: 10.1088/1361-6633/ab5c91. URL: https://doi.org/10.1088/1361-6633/ab5c91.

[69] Kasra Amini et al. “Symphony on strong field approximation”. In: *Reports on Progress in Physics* 82.11 (Oct. 2019), p. 116001. DOI: 10.1088/1361-6633/ab2bb1. URL: https://doi.org/10.1088/1361-6633/ab2bb1.

[70] J. Bestle, V. M. Akulin, and W. P. Schleich. “Classical and quantum stabilization of atoms in intense laser fields”. In: *Phys. Rev. A* 48 (1 July 1993), pp. 746–751. DOI: 10.1103/PhysRevA.48.746. URL: https://link.aps.org/doi/10.1103/PhysRevA.48.746.

[71] J. B. Watson et al. “Quantum signatures in the stabilization dynamics”. In: *Phys. Rev. A* 52 (5 Nov. 1995), pp. 4023–4028. DOI: 10.1103/PhysRevA.52.4023. URL: https://link.aps.org/doi/10.1103/PhysRevA.52.4023.

[72] J. B. Watson et al. “Entropic measure of wave-packet spreading and ionization in laser-driven atoms”. In: *Phys. Rev. A* 54 (1 July 1996), pp. 729–735. DOI: 10.1103/PhysRevA.54.729. URL: https://link.aps.org/doi/10.1103/PhysRevA.54.729.

[73] M. J. Norman et al. “Nonlinear dynamics of ionization stabilization of atoms in intense laser fields”. In: *Phys. Rev. A* 91 (2 Feb. 2015), p. 023406. DOI: 10.1103/PhysRevA.91.023406. URL: https://link.aps.org/doi/10.1103/PhysRevA.91.023406.

[74] A. Czirják et al. “The Wigner function for tunneling in a uniform static electric field Dedicated to Marlan O. Scully on the occasion of his 60th birthday.1”. In: *Optics Communications* 179.1 (2000), pp. 29–38. ISSN: 0030-4018. DOI: https://doi.org/10.1016/S0030-4018(99)00591-X. URL: http://www.sciencedirect.com/science/article/pii/S003040189900591X.

[75] Norio Takemoto and Andreas Becker. “Multiple Ionization Bursts in Laser-Driven Hydrogen Molecular Ion”. In: *Phys. Rev. Lett.* 105 (20 Nov. 2010), p. 203004. DOI: 10.1103/PhysRevLett.105.203004. URL: https://link.aps.org/doi/10.1103/PhysRevLett.105.203004.

[76] N Takemoto and A Becker. “Time-resolved view on charge-resonance-enhanced ionization”. In: *Phys. Rev. A* 84 (2011), p. 023401. DOI: 101103/PhysRevA84023401.

[77] C. Zagoya et al. “Quantum and semiclassical phase-space dynamics of a wave packet in strong fields using initial-value representations”. In: *New J. Phys.* 16 (2014), p. 103040. DOI: 10.1088/1367-2630/16/10/103040.

[78] J. Dubois et al. “Capturing Photoelectron Motion with Guiding Centers”. In: *Phys. Rev. Lett.* 121 (11 Sept. 2018), p. 113202. DOI: 10.1103/PhysRevLett.121.113202. URL: https://link.aps.org/doi/10.1103/PhysRevLett.121.113202.

[79] Stefanie Gräfe, Jens Doose, and Joachim Burgdörfer. “Quantum phase-space analysis of electronic rescattering dynamics in intense few-cycle laser fields”. In: *Journal of Physics B: Atomic, Molecular and Optical Physics* 45.5 (Feb. 2012), p. 055002. DOI: 10.1088/0953-4075/45/5/055002.

[80] A. Kamor et al. “Recollision Scenario without Tunneling: Role of the Ionic Core Potential”. In: *Phys. Rev. Lett.* 112 (13 Apr. 2014), p. 133003. DOI: 10.1103/PhysRevLett.112.133003. URL: https://link.aps.org/doi/10.1103/PhysRevLett.112.133003.

[81] S. A. Berman, C. Chandre, and T. Uzer. “Persistence of Coulomb focusing during ionization in the strong-field regime”. In: *Phys. Rev. A* 92 (2 Aug. 2015), p. 023422. DOI: 10.1103/PhysRevA.92.023422. URL: https://link.aps.org/doi/10.1103/PhysRevA.92.023422.

[82] C. Zagoya et al. “Different time scales in plasmonically enhanced high-order-harmonic generation”. In: *Phys. Rev. A* 93 (5 May 2016), p. 053419. DOI: 10.1103/PhysRevA.93.053419. URL: https://link.aps.org/doi/10.1103/PhysRevA.93.053419.

[83] S. A. Berman et al. “Coherent buildup of high-order harmonic radiation: The classical perspective”. In: *Phys. Rev. A* 97 (6 June 2018), p. 061402. DOI: 10.1103/PhysRevA.97.061402. URL: https://link.aps.org/doi/10.1103/PhysRevA.97.061402.

[84] Lukas Medišauskas et al. “Signatures of attosecond electronic–nuclear dynamics in the one-photon ionization of molecular hydrogen: analytical model versus ab initio calculations”. In: *New Journal of Physics* 17.5 (May 2015), p. 053011. DOI: 10.1088/1367-2630/17/5/053011.

[85] D Busto et al. “Time–frequency representation of autoionization dynamics in helium”. In: *Journal of Physics B: Atomic, Molecular and Optical Physics* 51.4 (Jan. 2018), p. 044002. DOI: 10.1088/1361-6455/aaa057.

[86] Tihamér Geyer and Jan M Rost. “A quasi-classical approach to fully differential ionization cross sections”. In: *Journal of Physics B: Atomic, Molecular and Optical Physics* 34.2 (Jan. 2001), pp. L47–L53. DOI: 10.1088/0953-4075/34/2/105. URL: https://doi.org/10.1088/0953-4075/34/2/105.

[87] C. Baumann, H.-J. Kull, and G. M. Fraiman. “Wigner representation of ionization and scattering in strong laser fields”. In: *Phys. Rev. A* 92 (6 Dec. 2015), p. 063420. DOI: 10.1103/PhysRevA.92.063420. URL: https://link.aps.org/doi/10.1103/PhysRevA.92.063420.

[88] Attila Czirják et al. “Emergence of oscillations in quantum entanglement during rescattering”. In: *Physica Scripta* T153 (Mar. 2013), p. 014013. DOI: 10.1088/0031-8949/2013/t153/014013.

[89] D J Wells and H M Quiney. “Wigner function analysis of high harmonic generation in atoms”. In: *Journal of Physics Communications* 4.12 (Dec. 2020), p. 125007. DOI: 10.1088/2399-6528/abd10d. URL: https://doi.org/10.1088/2399-6528/abd10d.

[90] Manfred Lein, Volker Engel, and E. K. U. Gross. “Phase-space analysis of double ionization”. In: *Opt. Express* 8.7 (Mar. 2001), pp. 411–416. DOI: 10.1364/OE.8.000411. URL: http://www.opticsexpress.org/abstract.cfm?URI=oe-8-7-411.

[91] F. Mauger, C. Chandre, and T. Uzer. “From Recollisions to the Knee: A Road Map for Double Ionization in Intense Laser Fields”. In: *Phys. Rev. Lett.* 104 (4 Jan. 2010), p. 043005. DOI: 10.1103/PhysRevLett.104.043005. URL: https://link.aps.org/doi/10.1103/PhysRevLett.104.043005.

[92] F. Mauger, C. Chandre, and T. Uzer. "Dynamics of recollisions for the double ionization of atoms in intense laser fields". In: *Phys. Rev. A* 81 (6 June 2010), p. 063425. DOI: 10.1103/PhysRevA.81.063425. URL: https://link.aps.org/doi/10.1103/PhysRevA.81.063425.

[93] F. Mauger, C. Chandre, and T. Uzer. "Recollisions and Correlated Double Ionization with Circularly Polarized Light". In: *Phys. Rev. Lett.* 105 (8 Aug. 2010), p. 083002. DOI: 10.1103/PhysRevLett.105.083002. URL: https://link.aps.org/doi/10.1103/PhysRevLett.105.083002.

[94] A. Kamor et al. "Controlling double ionization of atoms in an intense bichromatic laser pulse". In: *Phys. Rev. E* 83 (3 Mar. 2011), p. 036211. DOI: 10.1103/PhysRevE.83.036211. URL: https://link.aps.org/doi/10.1103/PhysRevE.83.036211.

[95] F. Mauger et al. "Mechanism of Delayed Double Ionization in a Strong Laser Field". In: *Phys. Rev. Lett.* 108 (6 Feb. 2012), p. 063001. DOI: 10.1103/PhysRevLett.108.063001. URL: https://link.aps.org/doi/10.1103/PhysRevLett.108.063001.

[96] F. Mauger et al. "Delayed double ionization as a signature of Hamiltonian chaos". In: *Phys. Rev. E* 85 (6 June 2012), p. 066205. DOI: 10.1103/PhysRevE.85.066205. URL: https://link.aps.org/doi/10.1103/PhysRevE.85.066205.

[97] J. Dubois, C. Chandre, and T. Uzer. "Envelope-Driven Recollisions Triggered by an Elliptically Polarized Pulse". In: *Phys. Rev. Lett.* 124 (25 June 2020), p. 253203. DOI: 10.1103/PhysRevLett.124.253203. URL: https://link.aps.org/doi/10.1103/PhysRevLett.124.253203.

[98] J. Dubois, C. Chandre, and T. Uzer. "Nonadiabatic effects in the double ionization of atoms driven by a circularly polarized laser pulse". In: *Phys. Rev. E* 102 (3 Sept. 2020), p. 032218. DOI: 10.1103/PhysRevE.102.032218. URL: https://link.aps.org/doi/10.1103/PhysRevE.102.032218.

[99] Eckhardt, B. and Sacha, K. "Wannier threshold law for two-electron escape in the presence of an external electric field". In: *Europhys. Lett.* 56.5 (2001), pp. 651–657. DOI: 10.1209/epl/i2001-00570-7. URL: https://doi.org/10.1209/epl/i2001-00570-7.

[100] Krzysztof Sacha and Bruno Eckhardt. "Pathways to double ionization of atoms in strong fields". In: *Phys. Rev. A* 63 (4 Mar. 2001), p. 043414. DOI: 10.1103/PhysRevA.63.043414. URL: https://link.aps.org/doi/10.1103/PhysRevA.63.043414.

[101] Krzysztof Sacha and Bruno Eckhardt. "Nonsequential triple ionization in strong fields". In: *Phys. Rev. A* 64 (5 Oct. 2001), p. 053401. DOI: 10.1103/PhysRevA.64.053401. URL: https://link.aps.org/doi/10.1103/PhysRevA.64.053401.

[102] Krzysztof Sacha and Bruno Eckhardt. "Pathways to non-sequential multiple ionization in strong laser fields". In: *Journal of Physics B: Atomic, Molecular and Optical Physics* 36.19 (Sept. 2003), pp. 3923–3935. DOI: 10.1088/0953-4075/36/19/004. URL: https://doi.org/10.1088/0953-4075/36/19/004.

[103] Jakub S. Prauzner-Bechcicki et al. "Nonsequential double ionization of molecules". In: *Phys. Rev. A* 71 (3 Mar. 2005), p. 033407. DOI: 10.1103/PhysRevA.71.033407. URL: https://link.aps.org/doi/10.1103/PhysRevA.71.033407.

[104] Jakub S. Prauzner-Bechcicki et al. "Time-Resolved Quantum Dynamics of Double Ionization in Strong Laser Fields". In: *Phys. Rev. Lett.* 98 (20 May 2007), p. 203002. DOI: 10.1103/PhysRevLett.98.203002. URL: https://link.aps.org/doi/10.1103/PhysRevLett.98.203002.

[105] F. Mauger, C. Chandre, and T. Uzer. "Strong Field Double Ionization: The Phase Space Perspective". In: *Phys. Rev. Lett.* 102 (17 May 2009), p. 173002. DOI: 10.1103/PhysRevLett.102.173002. URL: https://link.aps.org/doi/10.1103/PhysRevLett.102.173002.

[106] F Mauger, C Chandre, and T Uzer. "Strong field double ionization: what is under the 'knee'?" In: *Journal of Physics B: Atomic, Molecular and Optical Physics* 42.16 (July 2009), p. 165602. DOI: 10.1088/0953-4075/42/16/165602. URL: https://doi.org/10.1088%2F0953-4075%2F42%2F16%2F165602.

[107] Gerd van de Sand and Jan M. Rost. "Irregular Orbits Generate Higher Harmonics". In: *Phys. Rev. Lett.* 83 (3 July 1999), pp. 524–527. DOI: 10.1103/PhysRevLett.83.524. URL: https://link.aps.org/doi/10.1103/PhysRevLett.83.524.

[108] Gerd van de Sand and Jan M. Rost. "Semiclassical description of multiphoton processes". In: *Phys. Rev. A* 62 (5 Oct. 2000), p. 053403. DOI: 10.1103/PhysRevA.62.053403. URL: https://link.aps.org/doi/10.1103/PhysRevA.62.053403.

[109] Carlos Zagoya et al. "Dominant-interaction Hamiltonians for high-order-harmonic generation in laser-assisted collisions". In: *Phys. Rev. A* 85 (4 Apr. 2012), p. 041401. DOI: 10.1103/PhysRevA.85.041401. URL: https://link.aps.org/doi/10.1103/PhysRevA.85.041401.

[110] Carlos Zagoya et al. “An analytical approach to high harmonic generation”. In: *New Journal of Physics* 14.9 (Sept. 2012), p. 093050. DOI: 10.1088/1367-2630/14/9/093050. URL: https://doi.org/10.1088/1367-2630/14/9/093050.

[111] Bernhard W. Adams et al. “X-ray quantum optics”. In: *Journal of Modern Optics* 60.1 (2013), pp. 2–21. DOI: 10.1080/09500340.2012.752113. eprint: https://doi.org/10.1080/09500340.2012.752113. URL: https://doi.org/10.1080/09500340.2012.752113.

[112] Ralf Röhlsberger, Jörg Evers, and Sharon Shwartz. “Quantum and Nonlinear Optics with Hard X-Rays”. In: *Synchrotron Light Sources and Free-Electron Lasers: Accelerator Physics, Instrumentation and Science Applications*. Ed. by Eberhard Jaeschke et al. Cham: Springer International Publishing, 2014, pp. 1–28. ISBN: 978-3-319-04507-8. DOI: 10.1007/978-3-319-04507-8_32-1. URL: https://doi.org/10.1007/978-3-319-04507-8_32-1.

[113] A. Bambini and S. Stenholm. “Unification of Free Electron Laser Theories”. In: *Optica Acta: International Journal of Optics* 27.2 (1980), pp. 201–213. DOI: 10.1080/713820204. eprint: https://doi.org/10.1080/713820204. URL: https://doi.org/10.1080/713820204.

[114] L. Procida and Hai-Woong Lee. “Quantum dynamics of electrons in a free electron laser”. In: *Optics Communications* 49.3 (1984), pp. 201–204. ISSN: 0030-4018. DOI: https://doi.org/10.1016/0030-4018(84)90264-5. URL: http://www.sciencedirect.com/science/article/pii/0030401884902645.

[115] C. Moritz Carmesin et al. “Quantum and classical phase-space dynamics of a free-electron laser”. In: *Phys. Rev. Research* 2 (2 Apr. 2020), p. 023027. DOI: 10.1103/PhysRevResearch.2.023027. URL: https://link.aps.org/doi/10.1103/PhysRevResearch.2.023027.

[116] R Bonifacio et al. “A quantum model for collective recoil lasing”. In: *Europhysics Letters (EPL)* 69.1 (Jan. 2005), pp. 55–60. DOI: 10.1209/epl/i2004-10308-1. URL: https://doi.org/10.1209/epl/i2004-10308-1.

[117] N. Piovella et al. “A Wigner function model for free electron lasers”. In: *Optics Communications* 274.2 (2007), pp. 347–353. ISSN: 0030-4018. DOI: https://doi.org/10.1016/j.optcom.2007.02.061. URL: http://www.sciencedirect.com/science/article/pii/S0030401807002234.

[118] N. Piovella et al. “Three-Dimensional Wigner-Function Description of the Quantum Free-Electron Laser”. In: *Phys. Rev. Lett.* 100 (4 Jan. 2008), p. 044801. DOI: 10.1103/PhysRevLett.100.044801. URL: https://link.aps.org/doi/10.1103/PhysRevLett.100.044801.

[119] Peter Kling et al. “What defines the quantum regime of the free-electron laser?” In: *New Journal of Physics* 17.12 (Dec. 2015), p. 123019. DOI: 10.1088/1367-2630/17/12/123019. URL: https://doi.org/10.1088/1367-2630/17/12/123019.

[120] R. Bonifacio, N. Piovella, and G.R.M. Robb. “The quantum free electron laser: A new source of coherent, short-wavelength radiation”. In: *Fortschritte der Physik* 57.11-12 (2009), pp. 1041–1051. DOI: https://doi.org/10.1002/prop.200900097. eprint: https://onlinelibrary.wiley.com/doi/pdf/10.1002/prop.200900097. URL: https://onlinelibrary.wiley.com/doi/abs/10.1002/prop.200900097.

[121] K Burnett, V C Reed, and P L Knight. “Atoms in ultra-intense laser fields”. In: *Journal of Physics B: Atomic, Molecular and Optical Physics* 26.4 (Feb. 1993), pp. 561–598. DOI: 10.1088/0953-4075/26/4/003. URL: https://doi.org/10.1088/0953-4075/26/4/003.

[122] J. H. Eberly and K. C. Kulander. “Atomic Stabilization by Super-Intense Lasers”. In: *Science* 262.5137 (1993), pp. 1229–1233. ISSN: 0036-8075. DOI: 10.1126/science.262.5137.1229. eprint: https://science.sciencemag.org/content/262/5137/1229.full.pdf. URL: https://science.sciencemag.org/content/262/5137/1229.

[123] Sydney Geltman. “Are atoms stabilized by ultraintense lasers?” In: *Chemical Physics Letters* 237.3 (1995), pp. 286–290. ISSN: 0009-2614. DOI: https://doi.org/10.1016/0009-2614(95)00315-U. URL: http://www.sciencedirect.com/science/article/pii/000926149500315U.

[124] Mihai Gavrila. “Atomic stabilization in superintense laser fields”. In: *Journal of Physics B: Atomic, Molecular and Optical Physics* 35.18 (Sept. 2002), R147–R193. DOI: 10.1088/0953-4075/35/18/201. URL: https://doi.org/10.1088/0953-4075/35/18/201.

[125] P. Eckle et al. “Attosecond Ionization and Tunneling Delay Time Measurements in Helium”. In: *Science* 322.5907 (2008), pp. 1525–1529. ISSN: 0036-8075. DOI: 10.1126/science.1163439. URL: http://science.sciencemag.org/content/322/5907/1525.

[126] Nicolas Eicke, Simon Brennecke, and Manfred Lein. “Attosecond-Scale Streaking Methods for Strong-Field Ionization by Tailored Fields”. In: *Phys. Rev. Lett.* 124 (4 Jan. 2020), p. 043202. DOI: 10.1103/PhysRevLett.124.043202. URL: https://link.aps.org/doi/10.1103/PhysRevLett.124.043202.

[127] Petrissa Eckle et al. “Attosecond angular streaking”. In: *Nature Physics* 4.7 (July 2008), pp. 565–570. ISSN: 1745-2481. DOI: 10.1038/nphys982. URL: https://doi.org/10.1038/nphys982.

[128] Adrian N. Pfeiffer et al. “Attoclock reveals natural coordinates of the laser-induced tunnelling current flow in atoms”. In: *Nature Physics* 8.1 (Jan. 2012), pp. 76–80. DOI: 10.1038/nphys2125.

[129] Alexandra S. Landsman and Ursula Keller. “Attosecond science and the tunnelling time problem”. In: *Physics Reports* 547 (2015). Attosecond science and the tunneling time problem, pp. 1–24. ISSN: 0370-1573. DOI: https://doi.org/10.1016/j.physrep.2014.09.002. URL: http://www.sciencedirect.com/science/article/pii/S0370157314003159.

[130] Lisa Torlina et al. “Interpreting attoclock measurements of tunnelling times”. In: *Nature Physics* 11.6 (June 2015), pp. 503–508. ISSN: 1745-2481. DOI: 10.1038/nphys3340. URL: https://doi.org/10.1038/nphys3340.

[131] Hongcheng Ni et al. “Tunneling criteria and a nonadiabatic term for strong-field ionization”. In: *Phys. Rev. A* 98 (1 July 2018), p. 013411. DOI: 10.1103/PhysRevA.98.013411. URL: https://link.aps.org/doi/10.1103/PhysRevA.98.013411.

[132] U. Satya Sainadh et al. “Attosecond angular streaking and tunnelling time in atomic hydrogen”. In: *Nature* 568.7750 (Apr. 2019), pp. 75–77. ISSN: 1476-4687. DOI: 10.1038/s41586-019-1028-3. URL: https://doi.org/10.1038/s41586-019-1028-3.

[133] Nicolas Douguet and Klaus Bartschat. “Dynamics of tunneling ionization using Bohmian mechanics”. In: *Phys. Rev. A* 97 (1 Jan. 2018), p. 013402. DOI: 10.1103/PhysRevA.97.013402. URL: https://link.aps.org/doi/10.1103/PhysRevA.97.013402.

[134] C. Hofmann, A. S. Landsman, and U. Keller. “Attoclock revisited on electron tunnelling time”. In: *Journal of Modern Optics* 66.10 (2019), pp. 1052–1070. DOI: 10.1080/09500340.2019.1596325. eprint: https://doi.org/10.1080/09500340.2019.1596325. URL: https://doi.org/10.1080/09500340.2019.1596325.

[135] N.L Balazs and A Voros. “Wigner’s function and tunneling”. In: *Annals of Physics* 199.1 (1990), pp. 123–140. ISSN: 0003-4916. DOI: https://doi.org/10.1016/0003-4916(90)90370-4. URL: http://www.sciencedirect.com/science/article/pii/0003491690903704.

[136] Szabolcs Hack et al. *Reconstruction of tunnel exit time and exit momentum in strong field ionization, based on phase space methods*. 2019. arXiv: 1904.05465 [quant-ph].

[137] Szabolcs Hack et al. “Quantum interference in strong-field ionization by a linearly polarized laser pulse and its relevance to tunnel exit time and momentum”. In: *Physical Review A* 104.3 (2021), p. L031102.

[138] Michael Spanner. “Strong Field Tunnel Ionization by Real-Valued Classical Trajectories”. In: *Phys. Rev. Lett.* 90 (23 June 2003), p. 233005. DOI: 10.1103/PhysRevLett.90.233005. URL: https://link.aps.org/doi/10.1103/PhysRevLett.90.233005.

[139] Srihari Keshavamurthy and William H. Miller. “Semi-classical correction for quantum-mechanical scattering”. In: *Chemical Physics Letters* 218.3 (1994), pp. 189–194. ISSN: 0009-2614. DOI: https://doi.org/10.1016/0009-2614(93)E1485-Y. URL: http://www.sciencedirect.com/science/article/pii/0009261493E1485Y.

[140] Frank Grossmann and Eric J. Heller. “A semiclassical correlation function approach to barrier tunneling”. In: *Chemical Physics Letters* 241.1 (1995), pp. 45–50. ISSN: 0009-2614. DOI: https://doi.org/10.1016/0009-2614(95)00605-4. URL: https://www.sciencedirect.com/science/article/pii/0009261495006054.

[141] Kenneth G. Kay. “Semiclassical tunneling in the initial value representation”. In: *The Journal of Chemical Physics* 107.7 (1997), pp. 2313–2328. DOI: 10.1063/1.475143. eprint: https://doi.org/10.1063/1.475143. URL: https://doi.org/10.1063/1.475143.

[142] N. T. Maitra and E. J. Heller. “Barrier Tunneling and Reflection in the Time and Energy Domains: The Battle of the Exponentials”. In: *Phys. Rev. Lett.* 78 (16 Apr. 1997), pp. 3035–3038. DOI: 10.1103/PhysRevLett.78.3035. URL: https://link.aps.org/doi/10.1103/PhysRevLett.78.3035.

[143] D. B. Milošević. “Phase space path-integral formulation of the above-threshold ionization”. In: *Journal of Mathematical Physics* 54.4 (2013), p. 042101. DOI: 10.1063/1.4797476. URL: https://doi.org/10.1063/1.4797476.

[144] X.-Y. Lai et al. “Influence of the Coulomb potential on above-threshold ionization: a quantum-orbit analysis beyond the strong-field approximation”. In: *Phys. Rev. A* 92 (4 Oct. 2015), p. 043407. DOI: 10.1103/PhysRevA.92.043407. URL: https://link.aps.org/doi/10.1103/PhysRevA.92.043407.

[145] A. S. Maxwell et al. “Coulomb-corrected quantum interference in above-threshold ionization: Working towards multi-trajectory electron holography”. In: *Phys. Rev. A* 96.2 (2017), p. 023420. DOI: 10.1103/PhysRevA.96.023420. eprint: 1705.01518.

[146] A. S. Maxwell and Carla Figueira de Morisson Faria. “Coulomb-free and Coulomb-distorted recolliding quantum orbits in photoelectron holography”. In: *J. Phys. B At. Mol. Phys.* 51 (2018), p. 124001. eprint: 1802.00789. URL: http://arxiv.org/abs/1802.00789.

[147] A. S. Maxwell, S. V. Popruzhenko, and C. Figueira de Morisson Faria. "Treating branch cuts in quantum trajectory models for photoelectron holography". In: *Phys. Rev. A* 98 (6 Dec. 2018), p. 063423. DOI: 10.1103/PhysRevA.98.063423. URL: https://link.aps.org/doi/10.1103/PhysRevA.98.063423.

[148] N. I. Shvetsov-Shilovski et al. "Semiclassical two-step model for strong-field ionization". In: *Phys. Rev. A* 94 (1 July 2016), p. 013415. DOI: 10.1103/PhysRevA.94.013415. URL: https://link.aps.org/doi/10.1103/PhysRevA.94.013415.

[149] N. I. Shvetsov-Shilovski and M. Lein. "Semiclassical two-step model with quantum input: Quantum-classical approach to strong-field ionization". In: *Phys. Rev. A* 100 (5 Nov. 2019), p. 053411. DOI: 10.1103/PhysRevA.100.053411. URL: https://link.aps.org/doi/10.1103/PhysRevA.100.053411.

[150] N. I. Shvetsov-Shilovski. "Semiclassical two-step model for ionization by a strong laser pulse: further developments and applications". In: *The European Physical Journal D* 75 (4 Apr. 2021). DOI: 10.1140/epjd/s10053-021-00134-3. URL: https://doi.org/10.1140/epjd/s10053-021-00134-3.

[151] H-J Kull. "Position–momentum correlations in electron–ion scattering in strong laser fields". In: *New Journal of Physics* 14.5 (May 2012), p. 055013. DOI: 10.1088/1367-2630/14/5/055013.

[152] C. Symonds et al. "Coupled-coherent-states approach for high-order harmonic generation". In: *Phys. Rev. A* 91 (2 Feb. 2015), p. 023427. DOI: 10.1103/PhysRevA.91.023427. URL: https://link.aps.org/doi/10.1103/PhysRevA.91.023427.

[153] Dmitrii V. Shalashilin, Mark S. Child, and Adam Kirrander. "Mechanisms of double ionization in strong laser field from simulation with Coupled Coherent States: Beyond reduced dimensionality models". In: *Chemical Physics* 347.1 (2008). Ultrafast Photoinduced Processes in Polyatomic Molecules, pp. 257–262. ISSN: 0301-0104. DOI: https://doi.org/10.1016/j.chemphys.2007.11.006. URL: https://www.sciencedirect.com/science/article/pii/S0301010407005174.

[154] Adam Kirrander and Dmitrii V. Shalashilin. "Quantum dynamics with fermion coupled coherent states: Theory and application to electron dynamics in laser fields". In: *Phys. Rev. A* 84 (3 Sept. 2011), p. 033406. DOI: 10.1103/PhysRevA.84.033406. URL: https://link.aps.org/doi/10.1103/PhysRevA.84.033406.

[155] XiaoLei Hao et al. "Quantum Effects in Double Ionization of Argon below the Threshold Intensity". In: *Phys. Rev. Lett.* 112 (7 Feb. 2014), p. 073002. DOI: 10.1103/PhysRevLett.112.073002. URL: https://link.aps.org/doi/10.1103/PhysRevLett.112.073002.

[156] A. S. Maxwell and C. Figueira de Morisson Faria. "Quantum interference in time-delayed nonsequential double ionization". In: *Phys. Rev. A* 92 (2 Aug. 2015), p. 023421. DOI: 10.1103/PhysRevA.92.023421. URL: https://link.aps.org/doi/10.1103/PhysRevA.92.023421.

[157] A. S. Maxwell and C. Figueira de Morisson Faria. "Controlling Below-Threshold Nonsequential Double Ionization via Quantum Interference". In: *Phys. Rev. Lett.* 116 (14 Apr. 2016), p. 143001. DOI: 10.1103/PhysRevLett.116.143001. URL: https://link.aps.org/doi/10.1103/PhysRevLett.116.143001.

[158] Wei Quan et al. "Quantum interference in laser-induced nonsequential double ionization". In: *Phys. Rev. A* 96 (3 Sept. 2017), p. 032511. DOI: 10.1103/PhysRevA.96.032511. URL: https://link.aps.org/doi/10.1103/PhysRevA.96.032511.

[159] Gregory H. Wannier. "The Threshold Law for Single Ionization of Atoms or Ions by Electrons". In: *Phys. Rev.* 90 (5 June 1953), pp. 817–825. DOI: 10.1103/PhysRev.90.817. URL: https://link.aps.org/doi/10.1103/PhysRev.90.817.

[160] Tiham r Geyer and Jan M Rost. "Dynamical stabilization of classical multi-electron targets against autoionization". In: *Journal of Physics B: Atomic, Molecular and Optical Physics* 36.4 (Feb. 2003), pp. L107–L112. DOI: 10.1088/0953-4075/36/4/105. URL: https://doi.org/10.1088/0953-4075/36/4/105.

[161] Shiyang Zhong et al. "Attosecond electron–spin dynamics in Xe 4d photoionization". In: *Nature Communications* 11 (Oct. 2020). URL: https://doi.org/10.1038/s41467-020-18847-1.

[162] T. Zuo and A. D. Bandrauk. "Charge-resonance-enhanced ionization of diatomic molecular ions by intense lasers". In: *Phys. Rev. A* 52 (4 Oct. 1995), R2511–R2514. DOI: 10.1103/PhysRevA.52.R2511. URL: https://link.aps.org/doi/10.1103/PhysRevA.52.R2511.

[163] K Codling, L J Frasinski, and P A Hatherly. "On the field ionisation of diatomic molecules by intense laser fields". In: *Journal of Physics B: Atomic, Molecular and Optical Physics* 22.12 (June 1989), pp. L321–L327. DOI: 10.1088/0953-4075/22/12/004.

[164] S Chelkowski and A D Bandrauk. "Two-step Coulomb explosions of diatoms in intense laser fields". In: *Journal of Physics B: Atomic, Molecular and Optical Physics* 28.23 (Dec. 1995), pp. L723–L731. DOI: 10.1088/0953-4075/28/23/004.

[165] Tamar Seideman, M. Yu. Ivanov, and P. B. Corkum. "Role of Electron Localization in Intense-Field Molecular Ionization". In: *Phys. Rev. Lett.* 75 (15 Oct. 1995), pp. 2819–2822. DOI: 10.1103/PhysRevLett.75.2819. URL: https://link.aps.org/doi/10.1103/PhysRevLett.75.2819.

[166] André D. Bandrauk and Jonathan Ruel. "Charge-resonance-enhanced ionization of molecular ions in intense laser pulses: Geometric and orientation effects". In: *Phys. Rev. A* 59 (3 Mar. 1999), pp. 2153–2162. DOI: 10.1103/PhysRevA.59.2153. URL: https://link.aps.org/doi/10.1103/PhysRevA.59.2153.

[167] D. Pavi či ć et al. "Intense-Laser-Field Ionization of the Hydrogen Molecular Ions H_2^+ and D_2^+ at Critical Internuclear Distances". In: *Phys. Rev. Lett.* 94 (16 Apr. 2005), p. 163002. DOI: 10.1103/PhysRevLett.94.163002. URL: https://link.aps.org/doi/10.1103/PhysRevLett.94.163002.

[168] Norihiro Suzuki, Isao Kawata, and Koichi Yamashita. "Comparison of the mechanisms of enhanced ionization of H2 and H3+ in intense laser fields". In: *Chemical Physics* 338.2 (2007). Molecular Wave Packet Dynamics, pp. 348–353. ISSN: 0301-0104. DOI: https://doi.org/10.1016/j.chemphys.2007.05.018. URL: http://www.sciencedirect.com/science/article/pii/S0301010407001838.

[169] D. T. Strickland et al. "Optical studies of inertially confined molecular iodine ions". In: *Phys. Rev. Lett.* 68 (18 May 1992), pp. 2755–2758. DOI: 10.1103/PhysRevLett.68.2755. URL: https://link.aps.org/doi/10.1103/PhysRevLett.68.2755.

[170] E. Constant, H. Stapelfeldt, and P. B. Corkum. "Observation of Enhanced Ionization of Molecular Ions in Intense Laser Fields". In: *Phys. Rev. Lett.* 76 (22 May 1996), pp. 4140–4143. DOI: 10.1103/PhysRevLett.76.4140. URL: https://link.aps.org/doi/10.1103/PhysRevLett.76.4140.

[171] H. Chen et al. "Angle-resolved and internuclear-separation-resolved measurements of the ionization rate of the B state of I_2 by strong laser fields". In: *Phys. Rev. A* 84 (4 Oct. 2011), p. 043427. DOI: 10.1103/PhysRevA.84.043427. URL: https://link.aps.org/doi/10.1103/PhysRevA.84.043427.

[172] H. Chen, V. Tagliamonti, and G. N. Gibson. "Enhanced ionization of an inner orbital of I_2 by strong laser fields". In: *Phys. Rev. A* 86 (5 Nov. 2012), p. 051403. DOI: 10.1103/PhysRevA.86.051403. URL: https://link.aps.org/doi/10.1103/PhysRevA.86.051403.

[173] M. Schmidt, D. Normand, and C. Cornaggia. "Laser-induced trapping of chlorine molecules with pico- and femtosecond pulses". In: *Phys. Rev. A* 50 (6 Dec. 1994), pp. 5037–5045. DOI: 10.1103/PhysRevA.50.5037. URL: https://link.aps.org/doi/10.1103/PhysRevA.50.5037.

[174] Irina Bocharova et al. "Charge Resonance Enhanced Ionization of CO_2 Probed by Laser Coulomb Explosion Imaging". In: *Phys. Rev. Lett.* 107 (6 Aug. 2011), p. 063201. DOI: 10.1103/PhysRevLett.107.063201. URL: https://link.aps.org/doi/10.1103/PhysRevLett.107.063201.

[175] Matthias Paul and Stefanie Gräfe. "Strong-field ionization dynamics of asymmetric equilateral triatomic model molecules in circularly polarized laser fields". In: *Phys. Rev. A* 99 (5 May 2019), p. 053414. DOI: 10.1103/PhysRevA.99.053414. URL: https://link.aps.org/doi/10.1103/PhysRevA.99.053414.

[176] Merrick J. DeWitt and Robert J. Levis. "The role of electron delocalization in the ionization of C6 hydrocarbons using intense 780 nm laser pulses of femtosecond duration". In: *The Journal of Chemical Physics* 108.17 (1998), pp. 7045–7048. DOI: 10.1063/1.476121. eprint: https://doi.org/10.1063/1.476121. URL: https://doi.org/10.1063/1.476121.

[177] Sonia Erattupuzha et al. "Enhanced ionisation of polyatomic molecules in intense laser pulses is due to energy upshift and field coupling of multiple orbitals". In: *Journal of Physics B: Atomic, Molecular and Optical Physics* 50.12 (May 2017), p. 125601. DOI: 10.1088/1361-6455/aa7098.

[178] Yonghao Mi et al. "Electron-Nuclear Coupling through Autoionizing States after Strong-Field Excitation of H_2 Molecules". In: *Phys. Rev. Lett.* 118 (18 May 2017), p. 183201. DOI: 10.1103/PhysRevLett.118.183201. URL: https://link.aps.org/doi/10.1103/PhysRevLett.118.183201.

[179] B. Sheehy, B. Walker, and L. F. DiMauro. "Phase Control in the Two-Color Photodissociation of HD^+". In: *Phys. Rev. Lett.* 74 (24 June 1995), pp. 4799–4802. DOI: 10.1103/PhysRevLett.74.4799. URL: https://link.aps.org/doi/10.1103/PhysRevLett.74.4799.

[180] M R Thompson et al. "One and two-colour studies of the dissociative ionization and Coulomb explosion of with intense Ti:sapphire laser pulses". In: *Journal of Physics B: Atomic, Molecular and Optical Physics* 30.24 (Dec. 1997), pp. 5755–5772. DOI: 10.1088/0953-4075/30/24/014.

[181] Kunlong Liu and Ingo Barth. "Identifying the Tunneling Site in Strong-Field Ionization of $H_2{}^+$". In: *Phys. Rev. Lett.* 119 (24 Dec. 2017), p. 243204. DOI: 10.1103/PhysRevLett.119.243204. URL: https://link.aps.org/doi/10.1103/PhysRevLett.119.243204.

[182] M. Wu J.and Meckel et al. “Probing the tunnelling site of electrons in strong field enhanced ionization of molecules”. In: *Nature Communications* 3 (Oct. 2012). Article. URL: https://doi.org/10.1038/ncomms2130.

[183] G. L. Yudin et al. “Attosecond photoionization of coherently coupled electronic states”. In: *Phys. Rev. A* 72 (5 Nov. 2005), p. 051401. DOI: 10.1103/PhysRevA.72.051401. URL: https://link.aps.org/doi/10.1103/PhysRevA.72.051401.

[184] Alexei N. Markevitch et al. “Nonadiabatic dynamics of polyatomic molecules and ions in strong laser fields”. In: *Phys. Rev. A* 68 (1 July 2003), p. 011402. DOI: 10.1103/PhysRevA.68.011402. URL: https://link.aps.org/doi/10.1103/PhysRevA.68.011402.

[185] Alexei N. Markevitch et al. “Sequential nonadiabatic excitation of large molecules and ions driven by strong laser fields”. In: *Phys. Rev. A* 69 (1 Jan. 2004), p. 013401. DOI: 10.1103/PhysRevA.69.013401. URL: https://link.aps.org/doi/10.1103/PhysRevA.69.013401.

[186] M. R. Miller et al. “Laser-driven nonadiabatic electron dynamics in molecules”. In: *Optica* 3.3 (Mar. 2016), pp. 259–269. DOI: 10.1364/OPTICA.3.000259. URL: http://www.osapublishing.org/optica/abstract.cfm?URI=optica-3-3-259.

[187] Martin P. Bircher et al. “Nonadiabatic effects in electronic and nuclear dynamics”. In: *Structural Dynamics* 4.6 (2017), p. 061510. DOI: 10.1063/1.4996816. eprint: https://doi.org/10.1063/1.4996816. URL: https://doi.org/10.1063/1.4996816.

[188] Dror Shafir et al. “Resolving the time when an electron exits a tunnelling barrier”. In: *Nature* 485 (May 2012). URL: https://doi.org/10.1038/nature11025.

[189] Masataka Ohmi, Oleg I. Tolstikhin, and Toru Morishita. “Analysis of a shift of the maximum of photoelectron momentum distributions generated by intense circularly polarized pulses”. In: *Phys. Rev. A* 92 (4 Oct. 2015), p. 043402. DOI: 10.1103/PhysRevA.92.043402. URL: https://link.aps.org/doi/10.1103/PhysRevA.92.043402.

[190] Kunlong Liu et al. “Detecting and Characterizing the Nonadiabaticity of Laser-Induced Quantum Tunneling”. In: *Phys. Rev. Lett.* 122 (5 Feb. 2019), p. 053202. DOI: 10.1103/PhysRevLett.122.053202. URL: https://link.aps.org/doi/10.1103/PhysRevLett.122.053202.

[191] Feng He, Andreas Becker, and Uwe Thumm. "Strong-Field Modulated Diffraction Effects in the Correlated Electron-Nuclear Motion in Dissociating H_2^+". In: *Phys. Rev. Lett.* 101 (21 Nov. 2008), p. 213002. DOI: 10.1103/PhysRevLett.101.213002. URL: https://link.aps.org/doi/10.1103/PhysRevLett.101.213002.

[192] D.K. Arrowsmith and C.M. Place. *Dynamical Systems: Differential Equations, Maps, and Chaotic Behaviour*. New York: Routledge, 1992.

[193] Eric J. Heller. "Quantum localization and the rate of exploration of phase space". In: *Phys. Rev. A* 35 (3 Feb. 1987), pp. 1360–1370. DOI: 10.1103/PhysRevA.35.1360. URL: https://link.aps.org/doi/10.1103/PhysRevA.35.1360.

[194] J. Javanainen, J. H. Eberly, and Qichang Su. "Numerical simulations of multiphoton ionization and above-threshold electron spectra". In: *Phys. Rev. A* 38 (7 Oct. 1988), pp. 3430–3446. DOI: 10.1103/PhysRevA.38.3430. URL: https://link.aps.org/doi/10.1103/PhysRevA.38.3430.

[195] JH Eberly. "Scale variation in a one-dimensional model of an atom interacting with a strong laser field". In: *Phys. Rev. A* 42.9 (1990), p. 5750. DOI: 10.1103/PhysRevA.42.5750.

[196] Q Su and JH Eberly. "Model atom for multiphoton physics". In: *Phys. Rev. A* 44.9 (1991), p. 5997. DOI: 10.1103/PhysRevA.44.5997.

[197] SC Rae, X Chen, and K Burnett. "Saturation of harmonic generation in one- and three-dimensional atoms". In: *Phys. Rev. A* 50.2 (1994), p. 1946. DOI: 10.1103/PhysRevA.50.1946.

[198] M. D. Feit et al. "Solution of the Schrodinger Equation by a Spectral Method". In: *Journal of Computational Physics* 47 (1982), pp. 412–433.

[199] W. B. Case. "Wigner functions and Weyl transforms for pedestrians". In: *American Journal of Physics* 76 (Oct. 2008), pp. 937–946. DOI: 10.1119/1.2957889.

[200] Jung-Hoon Kim et al. "Wigner time-frequency distribution of high-order harmonics". In: *Phys. Rev. A* 63 (6 May 2001), p. 063403. DOI: 10.1103/PhysRevA.63.063403. URL: https://link.aps.org/doi/10.1103/PhysRevA.63.063403.

[201] L. Guo, S. S. Han, and J. Chen. "Time-energy analysis of above-threshold ionization in few-cycle laser pulses". In: *Phys. Rev. A* 86 (5 Nov. 2012), p. 053409. DOI: 10.1103/PhysRevA.86.053409. URL: https://link.aps.org/doi/10.1103/PhysRevA.86.053409.

[202] Anatole Kenfack and Karol Zyczkowski. "Negativity of the Wigner function as an indicator of non-classicality". In: *Journal of Optics B: Quantum and Semiclassical Optics* 6.10 (Aug. 2004), pp. 396–404. DOI: 10.1088/1464-4266/6/10/003. URL: https://doi.org/10.1088.

[203] J. E. Moyal. "Quantum mechanics as a statistical theory". In: *Mathematical Proceedings of the Cambridge Philosophical Society* 45.1 (1949), pp. 99–124. DOI: 10.1017/S0305004100000487.

[204] H.J. Groenewold. "On the principles of elementary quantum mechanics". In: *Physica* 12.7 (1946), pp. 405–460. ISSN: 0031-8914. DOI: https://doi.org/10.1016/S0031-8914(46)80059-4. URL: http://www.sciencedirect.com/science/article/pii/S0031891446800594.

[205] C. F. D. M. Faria and A. Fring. "Isospectral Hamiltonians from Moyal products". In: *Czechoslovak Journal of Physics* 56.9 (2006), pp. 899–908. DOI: 10.1007/s10582-006-0386-x. URL: https://openaccess.city.ac.uk/id/eprint/697/.

[206] J. Wu, B.B. Augstein, and C. Figueira de Morisson Faria. "Local dynamics in high-order-harmonic generation using Bohmian trajectories". In: *Phys. Rev. A* 88 (2013), p. 023415.

[207] J. Wu, B.B. Augstein, and C. Figueira de Morisson Faria. "Bohmian-trajectory analysis of high-order-harmonic generation: Ensemble averages, nonlocality, and quantitative aspects". In: *Phys. Rev. A* 88 (2013), p. 063416.

[208] Robert E. Wyatt. *Quantum Dynamics with Trajectories*. Springer-Verlag New York, 2005. ISBN: 978-0-387-28145-2. DOI: 10.1007/0-387-28145-2.

[209] E. Madelung. "Quantentheorie in hydrodynamischer Form". In: *Zeitschrift für Physik* 40.28 (1927), pp. 322–326. ISSN: 0044-3328. DOI: 10.1007/BF01400372. URL: https://doi.org/10.1007/BF01400372.

[210] Peter R. Holland. *The Quantum Theory of Motion: An Account of the de Broglie-Bohm Causal Interpretation of Quantum Mechanics*. Cambridge University Press, 1993. DOI: 10.1017/CBO9780511622687.

[211] M.J.W. Hall; D.A. Deckerd; H.M. Wiseman. "Quantum Phenomena Modeled by Interactions between Many Classical Worlds". In: ().

[212] L. Cruz-Rodríguez et al. "Quantum dynamics modeled by interacting trajectories". In: *Chemical Physics* 503 (2018), pp. 39–49. ISSN: 0301-0104. DOI: https://doi.org/10.1016/j.chemphys.2018.01.016. URL: https://www.sciencedirect.com/science/article/pii/S0301010417308558.

[213] L. Cruz-Rodríguez et al. “Quantum trajectory study of laser-driven atomic ionization”. In: *Chemical Physics Letters* 715 (2019), pp. 211–216. ISSN: 0009-2614. DOI: https://doi.org/10.1016/j.cplett.2018.11.031. URL: https://www.sciencedirect.com/science/article/pii/S0009261418309527.

[214] Zhou P. *Finite Difference Method. In: Numerical Analysis of Electromagnetic Fields.* Springer, Berlin, Heidelberg, 1993. ISBN: 978-3-642-50319-1. DOI: https://doi.org/10.1007/978-3-642-50319-1_3.

[215] D Kufel, H Chomet, and C Figueira de Morisson Faria. “Alternative quantisation condition for wavepacket dynamics in a hyperbolic double well”. In: *Journal of Physics A: Mathematical and Theoretical* 54.3 (Dec. 2020), p. 035304. DOI: 10.1088/1751-8121/abd267. URL: https://doi.org/10.1088/1751-8121/abd267.

[216] C. A. Downing. “On a solution of the Schrödinger equation with a hyperbolic double-well potential”. In: *Journal of Mathematical Physics* 54.7 (2013), p. 072101. DOI: 10.1063/1.4811855. eprint: https://doi.org/10.1063/1.4811855. URL: https://doi.org/10.1063/1.4811855.

[217] Laurens van der Maaten and Geoffrey Hinton. “Visualizing Data using t-SNE”. In: *Journal of Machine Learning Research* 9.86 (2008), pp. 2579–2605. URL: http://jmlr.org/papers/v9/vandermaaten08a.html.

[218] S. Kullback and R. A. Leibler. “On Information and Sufficiency”. In: *The Annals of Mathematical Statistics* 22.1 (1951), pp. 79–86. DOI: 10.1214/aoms/1177729694. URL: https://doi.org/10.1214/aoms/1177729694.

[219] Léon Bottou. “Online Algorithms and Stochastic Approximations”. In: *Online Learning and Neural Networks*. Ed. by David Saad. revised, oct 2012. Cambridge, UK: Cambridge University Press, 1998. URL: http://leon.bottou.org/papers/bottou-98x.

[220] Martin Wattenberg, Fernanda Viégas, and Ian Johnson. “How to Use t-SNE Effectively”. In: *Distill* (2016). DOI: 10.23915/distill.00002. URL: http://distill.pub/2016/misread-tsne.

[221] Szilárd Majorosi et al. “Density-based one-dimensional model potentials for strong-field simulations in He, H_2^+ and H_2”. In: (2019). arXiv: 1907.13619 [physics.atom-ph].

[222] C. Figueira de Morisson Faria et al. “Resonant enhancements of high-order harmonic generation”. In: *Phys. Rev. A* 65 (2 Jan. 2002), p. 023404. DOI: 10.1103/PhysRevA.65.023404. URL: https://link.aps.org/doi/10.1103/PhysRevA.65.023404.

[223] M Razavy. “An exactly soluble Schrödinger equation with a bistable potential”. In: *American Journal of Physics* 48.4 (1980), pp. 285–288.

[224] H Konwent, P Machnikowski, and A Radosz. “A certain double-well potential related to SU (2) symmetry”. In: *Journal of Physics A: Mathematical and General* 28.13 (1995), p. 3757.

[225] Qiong-Tao Xie. “New quasi-exactly solvable double-well potentials”. In: *Journal of Physics A: Mathematical and Theoretical* 45.17 (2012), p. 175302.

[226] R. R. Hartmann. “Bound states in a hyperbolic asymmetric double-well”. In: *Journal of Mathematical Physics* 55.1 (2014), p. 012105. DOI: 10.1063/1.4861938. eprint: https://doi.org/10.1063/1.4861938. URL: https://doi.org/10.1063/1.4861938.

[227] Moshe Shapiro and Paul Brumer. “Coherent Control of Atomic, Molecular, and Electronic Processes”. In: ed. by Benjamin Bederson and Herbert Walther. Vol. 42. Advances In Atomic, Molecular, and Optical Physics. Academic Press, 2000, pp. 287–345. DOI: https://doi.org/10.1016/S1049-250X(08)60189-5. URL: https://www.sciencedirect.com/science/article/pii/S1049250X08601895.

[228] Christopher Bäuerle et al. “Coherent control of single electrons: a review of current progress”. In: *Reports on Progress in Physics* 81.5 (Apr. 2018), p. 056503. DOI: 10.1088/1361-6633/aaa98a. URL: https://doi.org/10.1088/1361-6633/aaa98a.

[229] Y. Hikosaka et al. “Coherent control in the extreme ultraviolet and attosecond regime by synchrotron radiation”. In: *Nature Communications* 10.1 (Nov. 2019), p. 4988. ISSN: 2041-1723. DOI: 10.1038/s41467-019-12978-w. URL: https://doi.org/10.1038/s41467-019-12978-w.

[230] Andreas Reiserer and Gerhard Rempe. “Cavity-based quantum networks with single atoms and optical photons”. In: *Rev. Mod. Phys.* 87 (4 Dec. 2015), pp. 1379–1418. DOI: 10.1103/RevModPhys.87.1379. URL: https://link.aps.org/doi/10.1103/RevModPhys.87.1379.

[231] Dominik Peller et al. “Sub-cycle atomic-scale forces coherently control a single-molecule switch”. In: *Nature* 585.7823 (Sept. 2020), pp. 58–62. ISSN: 1476-4687. DOI: 10.1038/s41586-020-2620-2. URL: https://doi.org/10.1038/s41586-020-2620-2.

[232] M. F. Kling et al. “Control of Electron Localization in Molecular Dissociation”. In: *Science* 312.5771 (2006), pp. 246–248. DOI: 10.1126/science.1126259. eprint: https://www.science.org/doi/pdf/10.1126/science.1126259. URL: https://www.science.org/doi/abs/10.1126/science.1126259.

[233] G. Sansone et al. “Electron localization following attosecond molecular photoionization”. In: *Nature* 465.7299 (June 2010), pp. 763–766. ISSN: 1476-4687. DOI: 10.1038/nature09084. URL: https://doi.org/10.1038/nature09084.

[234] K. P. Singh et al. “Control of Electron Localization in Deuterium Molecular Ions using an Attosecond Pulse Train and a Many-Cycle Infrared Pulse”. In: *Phys. Rev. Lett.* 104 (2 Jan. 2010), p. 023001. DOI: 10.1103/PhysRevLett.104.023001. URL: https://link.aps.org/doi/10.1103/PhysRevLett.104.023001.

[235] H. Xu et al. “Observing electron localization in a dissociating H2+ molecule in real time”. In: *Nature Communications* 8.1 (June 2017), p. 15849. ISSN: 2041-1723. DOI: 10.1038/ncomms15849. URL: https://doi.org/10.1038/ncomms15849.

[236] J. I. Cirac et al. “Quantum State Transfer and Entanglement Distribution among Distant Nodes in a Quantum Network”. In: *Phys. Rev. Lett.* 78 (16 Apr. 1997), pp. 3221–3224. DOI: 10.1103/PhysRevLett.78.3221. URL: https://link.aps.org/doi/10.1103/PhysRevLett.78.3221.

[237] H. J. Kimble. “The quantum internet”. In: *Nature* 453.7198 (June 2008), pp. 1023–1030. ISSN: 1476-4687. DOI: 10.1038/nature07127. URL: https://doi.org/10.1038/nature07127.

[238] Mark M. Wilde, James M. McCracken, and Ari Mizel. “Could light harvesting complexes exhibit non-classical effects at room temperature?” In: *Proceedings of the Royal Society A: Mathematical, Physical and Engineering Sciences* 466.2117 (2010), pp. 1347–1363. DOI: 10.1098/rspa.2009.0575. eprint: https://royalsocietypublishing.org/doi/pdf/10.1098/rspa.2009.0575. URL: https://royalsocietypublishing.org/doi/abs/10.1098/rspa.2009.0575.

[239] Edward J. O’Reilly and Alexandra Olaya-Castro. “Non-classicality of the molecular vibrations assisting exciton energy transfer at room temperature”. In: *Nature Communications* 5.1 (Jan. 2014), p. 3012. ISSN: 2041-1723. DOI: 10.1038/ncomms4012. URL: https://doi.org/10.1038/ncomms4012.

[240] Vedran Dunjko and Hans J Briegel. “Machine learning and artificial intelligence in the quantum domain: a review of recent progress”. In: *Reports on Progress in Physics* 81.7 (June 2018), p. 074001. DOI: 10.1088/1361-6633/aab406. URL: https://doi.org/10.1088/1361-6633/aab406.

[241] Giuseppe Carleo et al. “Machine learning and the physical sciences”. In: *Rev. Mod. Phys.* 91 (4 Dec. 2019), p. 045002. DOI: 10.1103/RevModPhys.91.045002. URL: https://link.aps.org/doi/10.1103/RevModPhys.91.045002.

[242] Juan Carrasquilla. "Machine learning for quantum matter". In: *Advances in Physics: X* 5.1 (2020), p. 1797528. DOI: 10.1080/23746149.2020.1797528. eprint: https://doi.org/10.1080/23746149.2020.1797528. URL: https://doi.org/10.1080/23746149.2020.1797528.

[243] Anna Dawid et al. *Modern applications of machine learning in quantum sciences*. 2022. DOI: 10.48550/ARXIV.2204.04198. URL: https://arxiv.org/abs/2204.04198.

[244] Goëry Genty et al. "Machine learning and applications in ultrafast photonics". In: *Nature Photonics* 15.2 (Feb. 2021), pp. 91–101. ISSN: 1749-4893. DOI: 10.1038/s41566-020-00716-4. URL: https://doi.org/10.1038/s41566-020-00716-4.

[245] Chon-Teng Belmiro Chu, Yae-Lin Sheu, and Shih-I Chu. "Bayesian optimal control of the ultrashort circularly polarized attosecond pulse generation by two-color polarization gating". In: *Opt. Express* 29.21 (Oct. 2021), pp. 32900–32909. DOI: 10.1364/OE.438212. URL: http://opg.optica.org/oe/abstract.cfm?URI=oe-29-21-32900.

[246] Xinyao Liu et al. "Machine learning for laser-induced electron diffraction imaging of molecular structures". In: *Communications Chemistry* 4.1 (Nov. 2021), p. 154. ISSN: 2399-3669. DOI: 10.1038/s42004-021-00594-z. URL: https://doi.org/10.1038/s42004-021-00594-z.

[247] Xiwang Liu et al. "Deep Learning for Feynman's Path Integral in Strong-Field Time-Dependent Dynamics". In: *Phys. Rev. Lett.* 124 (11 Mar. 2020), p. 113202. DOI: 10.1103/PhysRevLett.124.113202. URL: https://link.aps.org/doi/10.1103/PhysRevLett.124.113202.

[248] N. I. Shvetsov-Shilovski and M. Lein. "Deep learning for retrieval of the internuclear distance in a molecule from interference patterns in photoelectron momentum distributions". In: *Phys. Rev. A* 105 (2 Feb. 2022), p. L021102. DOI: 10.1103/PhysRevA.105.L021102. URL: https://link.aps.org/doi/10.1103/PhysRevA.105.L021102.

[249] Karl Pearson F.R.S. "LIII. On lines and planes of closest fit to systems of points in space". In: *The London, Edinburgh, and Dublin Philosophical Magazine and Journal of Science* 2.11 (1901), pp. 559–572. DOI: 10.1080/14786440109462720. eprint: https://doi.org/10.1080/14786440109462720. URL: https://doi.org/10.1080/14786440109462720.

[250] Feng He, Camilo Ruiz, and Andreas Becker. "Control of Electron Excitation and Localization in the Dissociation of H_2^+ and Its Isotopes Using Two Sequential Ultrashort Laser Pulses". In: *Phys. Rev. Lett.* 99 (8 Aug. 2007), p. 083002. DOI: 10.1103/PhysRevLett.99.083002. URL: https://link.aps.org/doi/10.1103/PhysRevLett.99.083002.

[251] Zhuo Wang et al. “Control of electron localization in highly excited states with two ultraviolet laser pulses”. In: *Journal of Physics B: Atomic, Molecular and Optical Physics* 48.1 (Dec. 2014), p. 015601. DOI: 10.1088/0953-4075/48/1/015601. URL: https://doi.org/10.1088/0953-4075/48/1/015601.

[252] Vladimir Roudnev, B. D. Esry, and I. Ben-Itzhak. “Controlling HD^+ and H_2^+ Dissociation with the Carrier-Envelope Phase Difference of an Intense Ultrashort Laser Pulse”. In: *Phys. Rev. Lett.* 93 (16 Oct. 2004), p. 163601. DOI: 10.1103/PhysRevLett.93.163601. URL: https://link.aps.org/doi/10.1103/PhysRevLett.93.163601.

[253] Kunlong Liu et al. “Wavelength dependence of electron localization in the laser-driven dissociation of H2+”. In: *Opt. Express* 19.27 (Dec. 2011), pp. 26359–26369. DOI: 10.1364/OE.19.026359. URL: http://opg.optica.org/oe/abstract.cfm?URI=oe-19-27-26359.

[254] Kunlong Liu et al. “Anomalous isotopic effect on electron-directed reactivity by a 3-μm midinfrared pulse”. In: *Opt. Express* 21.4 (Feb. 2013), pp. 5107–5116. DOI: 10.1364/OE.21.005107. URL: http://opg.optica.org/oe/abstract.cfm?URI=oe-21-4-5107.

[255] Pengfei Lan, Eiji J. Takahashi, and Katsumi Midorikawa. “Efficient control of electron localization by subcycle waveform synthesis”. In: *Phys. Rev. A* 86 (1 July 2012), p. 013418. DOI: 10.1103/PhysRevA.86.013418. URL: https://link.aps.org/doi/10.1103/PhysRevA.86.013418.

[256] J. Wu et al. “Coulomb Asymmetry in Strong Field Multielectron Ionization of Diatomic Molecules”. In: *Phys. Rev. Lett.* 108 (4 Jan. 2012), p. 043002. DOI: 10.1103/PhysRevLett.108.043002. URL: https://link.aps.org/doi/10.1103/PhysRevLett.108.043002.

[257] Freek Kelkensberg et al. “A semi-classical model of attosecond electron localization in dissociative ionization of hydrogen”. In: *Phys. Chem. Chem. Phys.* 13 (19 2011), pp. 8647–8652. DOI: 10.1039/C1CP20058E. URL: http://dx.doi.org/10.1039/C1CP20058E.

[258] Norio Takemoto and Andreas Becker. “Time-resolved view on charge-resonance-enhanced ionization”. In: *Phys. Rev. A* 84.2 (2011), p. 023401. DOI: 10.1103/PhysRevA.84.023401.

[259] Norio Takemoto and Andreas Becker. “Visualization and interpretation of attosecond electron dynamics in laser-driven hydrogen molecular ion using Bohmian trajectories”. In: *The Journal of Chemical Physics* 134.7 (2011), p. 074309. DOI: 10.1063/1.3553178. eprint: https://doi.org/10.1063/1.3553178. URL: https://doi.org/10.1063/1.3553178.

[260] A. S. Maxwell et al. “Quantum estimation in strong fields: In situ ponderomotive sensing”. In: *Phys. Rev. A* 103 (4 Apr. 2021), p. 043519. DOI: 10.1103/PhysRevA.103.043519. URL: https://link.aps.org/doi/10.1103/PhysRevA.103.043519.

[261] Marc J. J. Vrakking. “Control of Attosecond Entanglement and Coherence”. In: *Phys. Rev. Lett.* 126 (11 Mar. 2021), p. 113203. DOI: 10.1103/PhysRevLett.126.113203. URL: https://link.aps.org/doi/10.1103/PhysRevLett.126.113203.

[262] Jorge Delgado et al. “Molecular fragmentation as a way to reveal early electron dynamics induced by attosecond pulses”. In: *Faraday Discuss.* (2021). DOI: 10.1039/D0FD00121J. URL: http://dx.doi.org/10.1039/D0FD00121J.

[263] Shuai Li et al. “Control of electron recollision and molecular nonsequential double ionization”. In: *Communications Physics* 3.1 (2020), pp. 1–8.